Investigating nickel and ceria anode electrochemistry in multifuel environments

Tabish, Tabish

DOI
10.4233/uuid:15e154d9-93bb-4d2a-83c5-6e6ebb0c13d87rdp-m164

Publication date
2019

Document Version
Final published version

Citation (APA)
Tabish, T. (2019). *Investigating nickel and ceria anode electrochemistry in multifuel environments*. [Dissertation (TU Delft), Delft University of Technology]. https://doi.org/10.4233/uuid:15e154d9-93bb-4d2a-83c5-6e6ebb0c13d87rdp-m164

Investigating Nickel and Ceria Anode Electrochemistry in Multifuel Environments A.N Tabish

Investigating Nickel and Ceria Anode Electrochemistry in Multifuel Environments

A.N. TABISH

Investigating Nickel and Ceria Anode Electrochemistry in Multifuel Environments

Dissertation

for the purpose of obtaining the degree of doctor

at Delft University of Technology

by the authority of the Rector Magnificus prof.dr.ir. T.H.J.J. van der Hagen

chair of the Board for Doctorates

to be defended publicly on

Wednesday 27 February 2019 at 12:30 o'clock

by

Asif Nadeem TABISH

Master of Science in Chemical Engineering, UET Lahore, Pakistan

born in Bahawal-Nagar, Pakistan.

This dissertation has been approved by the promotors.

Composition of the doctoral committee:

Rector Magnificus,	chairperson
Dr. P.V. Aravind	Delft University of Technology, promotor
Prof.dr.ir. B.J. Boersma	Delft University of Technology, promotor

Independent members:

Prof.dr.rer.nat. K.A. Friedrich	DLR, Germany
Prof.dr.ir. J.E. ten Elshof	University of Twente
Prof.dr. D.J.E.M. Roekaerts	Delft University of Technology
Prof.dr.ir. M.K. de Kreuk	Delft University of Technology
Dr.ir. R.E.F. Lindeboom	Delft University of Technology

This research was funded by the University of Engineering and Technology Lahore-Pakistan, and also partially supported by Delft University of Technology, The Netherlands.
Keywords: Solid Oxide Fuel Cell, Electrochemistry, Pattern electrode

ISBN/EAN: 978-94-6384-015-6

Summary

Conventional energy technologies and fossil fuels are causing irreversible damage to the environment. A transition from conventional to sustainable technologies is inevitable to address the environmental concerns. Solid oxide fuel cells (SOFCs) can play a key role in this transition because of their high efficiency and fuel flexibility – SOFCs can operate with fossil fuels as well as with renewable fuels. However, several challenges concerning cost reduction, operability, and long-term durability remain in SOFC development. A good physio-chemical and electrochemical understanding of the fuel-electrode is crucial to overcome the operability and durability limiting factors, as well as to design the new, improved, and low-cost electrodes.

Electrochemical reactions in SOFC anodes take place either at the triple-phase boundary (TPB) between the gas phase, oxide-ion conductor, and electron conductor – as in case of nickel/yttrium-stabilized zirconia (Ni/YSZ) electrodes – or at the two-phase boundary (2PB) between the gas phase and mixed ionic and electronic conducting (MIEC) material – as in case of ceria-based electrodes. Fuel electrodes of commercial cells are usually composites of metal and ceramic materials with three-dimensional porous structure. Such electrode designs exhibits high electrochemical performance, however, make the electrochemical reactions difficult to localize and investigate independently. Alternatively, pattern electrodes can be made with simplified, non-porous, and two-dimensional geometry having well-defined TPB or 2PB length, well suited for studying the electrochemistry. This thesis is aimed at investigating nickel and ceria anode electrochemistry in multi-fuel environments. For this purpose, both experimental (electrochemical impedance spectroscopy (EIS) and current-voltage measurements) as well as theoretical (elementary kinetic model, the Nernst-Planck-Poisson model, and electrochemical

model) approaches have been applied. Several results have been achieved and presented in this thesis:

EIS measurements show a lower polarization resistance and activation energy with ceria than nickel, in all gas environments we tested in this work. The polarization resistance for H_2 oxidation is less than that for CO oxidation for both nickel and ceria, indicating an ease of H_2 oxidation as compared to CO oxidation. The polarization resistance for syngas oxidation is closer to that for H_2 than CO, pointing towards a preferential oxidation of H_2 in a syngas environment. Adding a small amount of steam to CO gas causes a significantly larger drop in the polarization resistance compared to the drop caused by adding steam to H_2 gas stream. This observation is attributed to the combined effect of WGS conversion and preferential oxidation of hydrogen produced via WGS reaction. The elementary kinetic modeling shows that CO may also electrochemically oxidize, in addition to H_2, depending upon its concentration in syngas. Further, the contribution of direct CO oxidation is higher in case of ceria compared to nickel.

The Nernst-Planck-Poisson model reveals that the bulk diffusion of oxide-ions vacancies and electrons in a thin-film ceria anode is faster than the kinetics of hydrogen electrochemical oxidation. The charge-transfer between hydroxyl-ions and cerium-ions is the slowest and the rate-determining step. The computed exchange-current density, based on the rate-determining elementary step, fairly matches with the experimental results over a wide range of temperature and hydrogen partial pressure.

The TPB-based kinetics using nickel pattern electrode cell is also derived in this thesis and implemented in Ni/YSZ cermet electrode cell model. The TPB specific exchange-current for hydrogen oxidation (97% H_2 and 3% H_2O) at 800 [^oC] is found to be 3.06×10^{-6} [A/cm of the effective TPB length]. Further, the simulation of Ni/YSZ cermet electrode cell shows that the effective TPB length (= 1.78×10^7 [m/m^3]) is several orders of magnitude lower than the reported physical TPB densities of cermet electrode (= 10^{12} to 10^{13} [m/m^3]). This indicates that only a minor fraction of the total TPB is actually required or available to produce the total current at given cell voltage.

The effect of HCl contaminant on the electrode performance is also investigated. It is found that adding HCl (60 and 150 [ppm(v)]) in H_2/H_2O fuel gas lowers the polarization resistance for both nickel and ceria pattern electrode cells. This is the first time that lower polarization resistance is observed on exposing nickel and ceria pattern electrode cells to HCl contaminant. Apparently, HCl leaves permanent footprint on both of the electrodes as the polarization resistance after removing HCl is lower on nickel and higher on ceria compared to the resistance observed before adding HCl. Contrary to the pattern electrode cells, it is observed that the polarization resistance remains unchanged when Ni/gadolinium-doped ceria (GDC) cermet electrode cells are exposed to 60 [ppm(v)] HCl gas and increases for higher concentration levels (150 and 300 [ppm(v)]).

This page is intentionally left blank

Samenvatting

Conventionele energietechnologieën en fossiele brandstoffen veroorzaken onomkeerbare schade aan het milieu. Een transitie van conventionele naar duurzame technologieën is onvermijdelijk om de milieuproblemen aan te pakken. Vaste-oxidebrandstofcellen (solid oxide fuel cells (SOFCs)) kunnen een sleutelrol spelen in deze transitie omdat zij een hoge efficiëntie hebben en meerdere brandstoffen kunnen gebruiken – SOFCs kunnen zowel met fossiele als duurzame brandstoffen opereren. Er zijn echter uitdagingen in de ontwikkeling van SOFCs met betrekking tot kostenreductie, betrouwbaarheid en levensduur. Een goed fysicochemisch en elektrochemisch begrip van de brandstofelektrode is onmisbaar om de operationele- en levensduurlimieten te verruimen, alsmede om nieuwe, verbeterde en goedkope elektroden te ontwerpen. De elektrochemische reacties in SOFC anoden vinden of plaats in de zogenaamde driefasen-grens (triple-phase boundary (TPB)) tussen de gasfase, zuurstofgeleider en elektronengeleider – zoals in het geval van Nickel/Yttrium-gestabiliseerd-Zirkonium (Ni/YSZ) – of in de tweefasengrens (two-phase boundary (2PB)) tussen de gasfase en een materiaal met zowel ionen als elektronen-geleidende eigenschappen (mixed ionic and electronic conductor (MIEC)) – zoals het geval is voor elektroden gebaseerd op Cerium. In de praktijk zijn electroden meestal een samenstelling van een metaal en een keramisch materiaal (cermet) met een driedimensionale poreuze structuur. Een dergelijk elektrodeontwerp resulteert in goede elektrochemische eigenschappen, maar maakt het moeilijk om vast te stellen waar de elektrochemische reactie plaatsvindt en onafhankelijk te bestuderen. Daarom worden patroon-elektroden vervaardigt met een vereenvoudigd, niet poreuze en tweedimensionale geometrie, waardoor de lengte van de TPB of 2PB goed gedefinieerd is en de elektrochemie in detail bestudeerd kan worden. In deze dissertatie wordt de elektrochemie in Nickel- en Cerium-anoden onderzocht wan-

neer deze worden blootgesteld aan verschillende brandstoffen. Daarvoor zijn zowel experimentele (electrochemical impedance spectroscopy (EIS) en stroom-voltage metingen) als theoretische (een elementair kinetisch model, het Nernst-Planck-Poisson model en een electrochemisch model) benaderingen gebruikt. Daarmee zijn verscheidene resultaten bereikt, die beschreven zijn in deze dissertatie: EIS metingen laten een lagere polarisatieweerstand en activatie-energie zien voor Cerium dan voor Nickel, voor alle in dit werk geteste gascomposities. De polarisatieweerstand is lager voor H_2 dan die voor CO oxidatie met zowel Nickel als Cerium, wat erop duidt dat H_2 eenvoudiger te oxideren is dan CO. De polarisatieweerstand voor synthetisch gas ligt dichter bij die van H_2 dan van CO, wat op een voorkeur voor de oxidatie van H_2 wijst wanneer de elektrode aan een synthetisch gas wordt blootgesteld. Wanneer een kleine hoeveelheid stoom wordt toegevoegd aan CO wordt de polarisatieweerstand aanzienlijk meer verlaagd dan wanneer stoom aan H_2 wordt toegevoegd. Deze observatie kan verklaard worden door een combinatie van het effect van de water-gas-shift (WGS) conversie en de voorkeur voor de oxidatie van de waterstof die middels de WGS reactie gevormd wordt. Elementaire kinetische modellering toont aan dat CO ook elektrochemisch geoxideerd kan worden, naast H_2, afhankelijk van de CO-concentratie in het synthetisch gas. De bijdrage van CO-oxidatie is groter voor Cerium dan voor Nickel. Het Nernst-Planck-Poisson model toont aan dat de bulk-diffusie van zuurstofionen en elektronen in een dunne-film-Cerium-anode veel sneller is dan de kinetica van de elektrochemische waterstofoxidatie. De ladingsoverdracht tussen hydroxylionen en Cerium-ionen is de langzaamste en snelheidsbepalende stap. De berekende uitwisselingsstroom-dichtheid, gebaseerd op de snelheidsbepalende stap, is overeenkomstig met de experimentele resultaten in een ruim bereik van temperaturen en partiele drukken. Met een Nickel patroon-elektrode is de TPB-gebaseerde kinetica afgeleid in deze dissertatie, en geïmplementeerd in een Ni-YSZ cermet-cel model. De TPB-specifieke uitwisselingstroom-dichtheid voor waterstofoxidatie (97% H_2 en 3% H_2O) bij 800 [^oC] was $3.06x10^{-6}$ [A/cm effectieve TPB-lengte]. Simulatie van een anode-ondersteunde cermet-cel toont aan dat de effectieve TPB-lengte (= $1.78x10^7$ [m/m^3]) enkele ordergrootten kleiner is dan gerapporteerde fysieke TPB-dichtheiden van cermet anoden (= 10^{12} to 10^{13} [m/m^3]). Dit duidt erop dat slechts een klein deel van de totale TPB

daadwerkelijk nodig of beschikbaar is om de totale stroom te produceren bijeen gegeven cel-voltage. Het effect van HCl vergiftiging op de prestatie van de elektrode is ook onderzocht. Het toevoegen van HCl (60 en 150 [ppm(v)]) in een H_2/H_2O gasmengsel verlaagt de polarisatieweerstand voor zowel Nickel als Cerium patroon-elektroden. Dit is de eerste keer dan een lagere polarisatieweerstand is waargenomen wanneer Nickel en Cerium blootgesteld worden aan HCl vergiftiging. Het lijkt erop dat HCl beide patroon-elektroden blijvend verandert, aangezien de polarisatieweertand nadat HCl verwijdert is uit het gasmengsel lager is voor Nickel en hoger is voor Cerium ten opzichte van de weerstand die gemeten is voordat HCl toegevoegd werd. In tegenstelling tot de patroon-elektroden verandert de polarisatieweerstand niet wanneer een Nickel/Gadolinium-gedoopt-Cerium (GDC) cermet anode blootgesteld wordt aan 60 [ppm(v)] HCl, en neemt de polarisatieweerstand toe voor hogere concentraties (150 en 300 [ppm(v)].

This page is intentionally left blank

Contents

List of Figures

List of Tables

1

Introduction

1.1 Background

As the world population grows, so does the energy demand. This ever-increasing demand combined with the concerns of global temperature rise, caused by the greenhouse gas emissions, impose immense pressure on the energy sources and technologies. Beginning in the early 2000s, growing concerns of the climate changes heightened the interest in the development of renewable energy sources. While renewable fuels are the world's fastest-growing sources of energy, fossil fuels are expected to supply more than three fourth of the world total energy consumption till mid of the 21st century [1]. Therefore, the fossil fuels, in particular natural gas and oil, will be seen as playing a dominant role in the global energy systems for many decades.

While the role of fossil fuels in the 21st-century energy sector cannot be overlooked, improvements in the energy efficiency are inevitable. Electrical energy is a form of energy, currently generated mainly by thermomechanical conversion of fuel: heat is produced via fuel combustion, which is subsequently converted to mechanical energy and ultimately to electrical energy. The efficiency of this process is limited by the Carnot's theorem, and cannot exceed a certain limit. Alternatively, chemical energy contained in a fuel can directly and efficiently be converted to electrical energy via electrochemical conversion. A fuel cell is a device that works on the principle of electrochemical conversion, and so provides a good way to increase the energy efficiency.

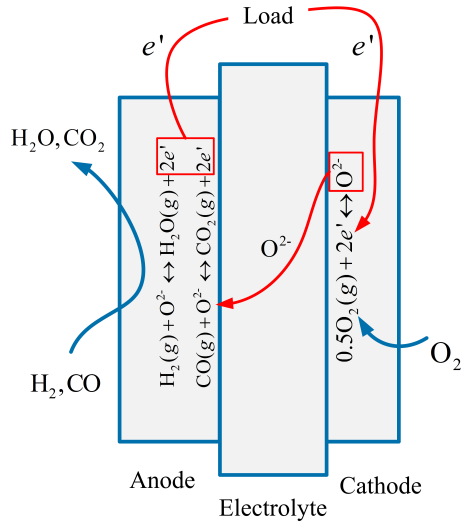

Figure 1.1 Schematic of a solid oxide fuel cell

There are five major types of fuel cells: the phosphoric acid fuel cell (PAFC), the polymer electrolyte membrane fuel cell (PEMFC), the alkaline fuel cell (AFC), the molten carbonate fuel cell (MCFC), and the solid-oxide fuel cell (SOFC). All are currently subjects of academic and industrial research. The SOFCs are of particular interest because they operate at high temperature and offer an alternative for efficiently utilizing a wide range of fuels including conventional fossil fuels such as natural gas and liquefied petroleum gas (LPG) as well as sustainable biomass-derived fuels such as biogas and synthesis gas (or syngas). High fuel-flexibility is attributed to the fact that O^{2-} ions are the species transported through the electrolyte (as shown in fig 1.1); allowing SOFCs to operate, in principle, on any combustible fuel [2]. For use with such fuels, requires anode materials with low cost as well as high electrochemical activity, electronic conductivity, thermal compatibility with electrolyte material, chemical stability in a redox environment, tolerance to carbon deposition, and resistance to sulphur and chlorine poisoning.

Currently, Ni/YSZ – a cermet (metal and ceramic) of nickel and yttrium-stabilized zirconia – is the state-of-the-art anode material because it fulfils most of the electrode requirements mentioned above. In

addition, Ni/YSZ also facilitates internal reforming[1]; thus, converting some, if not all, of the hydrocarbons to a mixture of H_2 and CO prior to electrochemical oxidation. However, Ni/YSZ have some inherent disadvantages such as performance degradation over a prolonged operation, low tolerance to sulphur and chlorine impurities present in hydrocarbon fuels, and propensity to form carbon deposits. Long-chain "sooty" carbon deposits are formed on the nickel surface unless a large amount of steam is provided along with hydrocarbon fuel. Alternatively, ceria cermets such as Ni/GDC and Cu/GDC (GDC: gadolinium-doped ceria) exhibit promising performance in the same environment without any appreciable carbon deposition; usually related to the mixed ionic electronic conductivity that ceria exhibits under reducing conditions [2]. Ceria cermets are, therefore, considered as potential alternatives to conventional Ni/YSZ cermets for hydrocarbon-based SOFC systems.

The selection of appropriate anode material for specific fuel type requires a deep understanding of the interaction chemistry between anode material and fuel components. For instance, syngas and reforming products (reformat) mainly contain H_2 and CO as principle oxidizable components. The effectiveness of anode, in such an environment, will depend primarily on the ability of anode material to oxidize H_2/CO mixture, particularly oxidize CO – either via direct electrochemical oxidation ($CO(g) + O^{2-}(el) \rightarrow CO_2(g) + 2e'$) or via water-gas-shift (WGS) conversion ($CO(g) + H_2O(g) \rightleftharpoons CO_2(g) + H_2(g)$). While, the kinetics of H_2 electrochemical oxidation is generally faster than that of CO [3], the relative importance of H_2 and CO oxidation kinetics during the oxidation of H_2/CO mixtures is not clear. More importantly, the role of WGS reaction in the overall oxidation process is not clearly understood. Therefore, a comprehensive work, both experimental and theoretical, is required to characterize the SOFC anode performance for a wide range of syngas mixtures.

While, the kinetics of H_2 and CO electrochemical oxidation on Ni/YSZ cermet anode is better known **[4]**, same is not true in case of ceria cermet anode. Even the kinetics of H_2 electrochemical oxidation on ceria is not

[1] Reforming is a method of producing H_2 and CO from hydrocarbons such as methane (steam reforming: $CH_4 + H_2O \rightarrow CO + 3H_2$ or dry reforming: $CH_4 + CO_2 \rightarrow 2CO + 2H_2$).

fully understood. Understanding and formulating the oxidation kinetics on supported/unsupported ceria is a key in the development of ceria-based cermets as the fuel oxidation primarily takes place at the ceria surface exposed to the fuel gas. The knowledge available on this subject is insufficient and requires further explanations.

Besides H_2 and CO, syngas also contains varying levels of sulphur and chlorine contaminants such as H_2S and HCl, that are likely to degrade the cell performance. Therefore, understanding the interaction chemistry between these contaminants and the anode materials, is also of critical importance for future advances of SOFC technology running on practical fuels.

1.2 Anode structure and Pattern-anode

A practical cermet anode consists of a complex network of pores, and ion conducting and electron conducting phases. The point at which three phases are in simultaneous contact, is commonly known as the triple-phase-boundary (TPB). The triple-phase boundaries are believed to be the electrochemically active sites of fuel cell electrodes because only at these locations electrochemical reactions can occur. Therefore, knowing the TPB length is essential in studying the kinetics of electrochemical fuel oxidation; also, because the polarization resistance, related to these kinetics, generally decreases with increasing the TPB length [5]. However, quantifying the TPB length of a cermet electrode is difficult because of the complex 3D microporous structure of the cermet. This, combined with the interference of gas-phase transport, makes cermet electrode cells non-ideal for kinetics study.

SOFC pattern electrodes, first introduced by Mizusaki et al. [6], are increasingly used in the literature for experimental and theoretical investigations of the electrode electrochemistry. A schematic of pattern anode is shown in fig.1.2. Dense patterns are usually fabricated by photolithography or directly sputtering the target material onto the electrolyte substrate through a stainless-steel mask. The simplified 2D geometry of the patterns allows accurate measurement of the TPB length; that is equal to the perimeter of pattern (length of interface between the electrode and the electrolyte). For instance, area specific TPB length of the

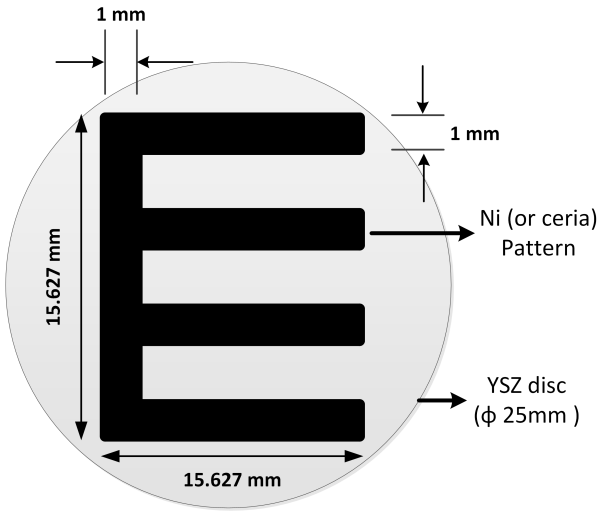

Figure 1.2 Schematic of a pattern electrode

pattern shown in fig.1.2 is 0.2027 m/cm^2. Since TPB length is accurately quantified and the influence of gas-phase transport is eliminated, it is possible to develop the TPB-based kinetics of the oxidation process and implement in a macroscale model for design optimizations.

1.3 Objectives and thesis outline

While several studies have addressed the electrochemical oxidation of H_2, CO, and H_2/CO mixtures, there is little consensus on the mechanistic details, especially for ceria electrode. Formulating the elementary reactions and evaluating the kinetics of each step involved will help in identifying the rate-limiting steps and establishing the kinetic parameters. This knowledge will help in understanding the relative importance of underlying electrochemical and physiochemical processes.

The overall objective of this research is to improve our understanding regarding the electrochemistry of nickel and ceria anodes in multifuel environments. In order to design the scope of this research, we selected syngas as a target fuel as it contains both oxidizable components (H_2 and CO) as well as contaminants of sulphur and chlorine such as H_2S and HCl. We explored the electrochemistry of both nickel, a conventional anode material, and ceria, a potential alternative, in the similar

environments. Furthermore, we considered chlorine contaminant only as it is less explored and very little is known about its poisoning mechanisms. The effect of H_2S contaminant on the nickel and ceria anode electrochemistry has been explored previously in the group [7]. Finally, we formulated following questions which, we think, require immediate attention in the SOFC development.

1. How does syngas composition affect the reaction kinetics of H_2 and CO electrochemical oxidation on nickel and ceria anodes?

2. How does reaction kinetics and defect transport contribute to electrochemical oxidation on ceria?

3. How does the TPB-based kinetics help in understanding the performance of cermet electrode cells?

4. How can pattern electrode help in understanding the effect of HCl on anode electrochemistry?

This thesis is an attempt to address the above-mentioned questions separately. Introduction of the topic and scope of this thesis are presented in the current chapter whereas outline of following chapters is as follows:

In **Chapter 2**, the kinetics of H_2 and CO electrochemical oxidation is discussed with a specific focus on the kinetics of co-oxidation using both experimental and theoretical approaches. Pattern electrode cells are employed for experimental and elementary kinetic model is developed for theoretical investigations. Electrochemical oxidation of H_2/CO mixtures is studied, in both dry and wet conditions, and relative kinetics of H_2 and CO oxidation in H_2/CO mixtures is evaluated, for both nickel and ceria. Furthermore, a direct comparison of the performance is made between these two electrode materials.

In **Chapter 3**, a detailed understanding of the electrochemical oxidation of H_2 on ceria is presented. Using the Nernst-Planck-Poisson (NPP) model and detailed oxidation mechanism, relative importance of the reaction kinetics, and ionic transport and electronic transport in the bulk of ceria is evaluated. A rate-limiting step is identified and exchange current density based on that step is calculated and validated with the experimental results.

In **Chapter 4**, the TPB specific kinetics is derived first using experimental results obtained with nickel pattern electrode cells and then implemented in the Ni/YSZ cermet electrode cell model. The effective TPB density of Ni/YSZ cermet electrode is calculated using the TPB-based kinetics and compared with the physical TPB density of the cermet electrode. Also, the effect of various operating conditions on the activation overpotential is discussed.

While several researchers have investigated the effect of HCl on the performance of cermet electrode cells, we employed nickel and ceria pattern electrode cells to better understand the influence of HCl on the electrochemistry of fuel oxidation on the anode. The results of this investigation are presented in **Chapter 5**.

In **Chapter 6** key findings of this thesis are summarized and a future outlook is provided as well.

This page is intentionally left blank

2

Electrochemical oxidation of syngas on nickel and ceria electrodes

In the previous chapter, a global overview of SOFC technology is presented and challenges regarding SOFC anode development are highlighted. Poor understanding of anode electrochemistry, particularly in syngas (H_2/CO mixture) environment, is one of these challenges. While cell performance with syngas has been investigated in several studies, relative kinetics of H_2 and CO electrochemical oxidation and role of water-gas shift conversion are still unclear. The most common assumption that H_2 is the only electroactive species in syngas is also questioned in recent studies, but with a little knowledge of kinetics. Kinetic modeling of elementary reactions occurring at pattern electrodes is helpful in studying the electrode electrochemistry and develop the reaction kinetics. In this chapter, electrochemical oxidation of syngas in both dry and wet gas environments is explored and presented. A specific focus has been on developing the relative kinetics of H_2 and CO electrochemical oxidation and comparing the electrochemical performance of nickel and ceria pattern electrode cells.

This chapter has been published as: A.N. Tabish, H.C. Patel, and P.V. Aravind. Electrochemical Oxidation of Syngas on Nickel and Ceria Anodes. Electrochimica Acta. 228 (2017) 575-585

2.1 Introduction

SOFCs are considered as promising candidates for next generation stationary power production because they are efficient and fuel flexible. Besides hydrogen, various hydrocarbon-based fuels such as biomass and coal derived synthetic gas (syngas), natural gas, and biogas are suggested as potential fuels for SOFCs as they can be fed directly to the anode after necessary cleaning [8–11]. Syngas is mainly a mixture of hydrogen, CO, and varying concentrations of CH_4, H_2O, CO_2, N_2, and other impurities. Natural gas and biogas can also be reformed to produce a mixture of hydrogen and CO. Thus, in all these fuels, a mixture of hydrogen and CO is ultimately expected to undergo an electrochemical oxidation. When a CO/H_2 mixture is fed to an SOFC anode, the overall (electro-)chemical reactions can be described as (the Kröger-Vink notation):

$$H_2 + O_O^x \rightarrow H_2O + V_O^{\bullet\bullet} + 2e' \tag{2.1}$$

$$CO + O_O^x \rightarrow CO_2 + V_O^{\bullet\bullet} + 2e' \tag{2.2}$$

$$CO + H_2O \rightleftharpoons CO_2 + H_2 \tag{2.3}$$

here O_O^x is a regular oxide-ion in the electrolyte and $V_O^{\bullet\bullet}$ is an oxide-ion vacancy created during an electrochemical reaction.

The total faradaic current is a result of two charge-transfer reactions (reaction 2.1 and 2.2). Relative contribution of these individual reactions is not very clear so far. Several experimental [12–16] and modeling [17–22] studies investigated the effect of syngas composition on the cell performance. For example, at low CO concentrations, even up to equimolar CO/H_2 mixture, the cell performance is almost same as obtained by a slightly moist hydrogen [13]. Sasaki [15] reported only 4 % drop in cell voltage for CO/H_2 = 7:3 (at 1000 [°C] and 0.32 [A/cm^2] indicating only an insignificant effect on cell performance. Sukeshini [16] observed a monotonous decrease in the maximum power density with an increase in CO/H_2 ratio, and degradation was not more than 25 % for CO/H_2 = 3:1. For very high CO fractions, CO/H_2 = 9:1, a significant drop in cell performance at 950 [°C] is reported [14]. The experimental studies were conducted for a short-term operation and proved a good performance for a wide range of CO/H_2 ratios.

Several studies have shown that the rate of CO electrochemical oxidation is 2-3 times slower than that of hydrogen [12]. Therefore, hydrogen is expected to oxidize preferentially in a syngas mixture [3]. It is worthwhile remembering that steam is a product of hydrogen oxidation which may in turn promote CO conversion via water-gas shift (WGS) reaction (reaction 2.3), therefore, producing more hydrogen. Whether CO electrochemically oxidizes at all, is very uncertain. In the modeling studies, two approaches are generally considered to address this concern. Firstly, it is assumed that only hydrogen participates in the electrochemical reaction, while CO is converted to hydrogen via WGS reaction. So, the total current density is solely attributed to electrochemical oxidation of hydrogen. Secondly, some authors [17, 19] have taken care of the current fraction from hydrogen and CO on the basis of their electrochemical oxidation rates in CO/CO_2 and H_2/H_2O environments, respectively. Both of these approaches have limitations because of non-electrochemical oxidation of CO in the first and a linear coupling between hydrogen and CO electrochemistry in the latter. Recently, Bao et al.[18, 23] proposed a non-linear coupling of hydrogen and CO electrochemistry in order to correlate the total current output with syngas composition. They developed a model based on macroscopic electrochemistry and species transport in a complex microporous structure. They conclude that, as CO/H_2 ratio increases, the hydrogen current fraction decreases which they associated to the contribution of electrochemical oxidation of CO. However, as their model was based on the global oxidation kinetics, an elementary kinetic approach can provide a further insight into possible contribution of direct CO electrochemical oxidation.

Using syngas as an SOFC fuel requires electrochemically stable anode materials besides their high electrocatalytic activity. An effective and viable anode material is expected to maximize the (electro-)chemical oxidation (reactions 2.1-2.3) and suppress the coke formation and the influence of syngas contaminants like H_2S and HCl. The state-of-the-art Ni/YSZ cermet fulfills most of the requirements related to catalysis. However, inherited poor redox stability and carbon cracking activity of nickel [24, 25] make these cermets less suitable for use in a syngas. Recently, ceria-based materials have gained a considerable attention as possible alternative for hydrocarbon feeds [26, 27]. For non-electrochemical applications, ceria has been extensively investigated as a support material

for various reactions like hydrocarbon oxidation, WGS conversion, and CO preferential oxidation (CO-PROX) [28]. As an anode material, it has shown even a better catalytic activity for hydrogen and CO oxidation compared to nickel [3, 29]. The superior activity of ceria is a result of extended reaction sites on ceria surface that are limited to TPB in case of nickel electrode. Conversely, electronic conductivity and WGS catalytic activity of pure ceria is too low to be used as an anode material for commercial applications [30, 31]. The electronic conductivity of ceria in a reduced environment is of the order of 0.2–2.0 [S/cm] that is 3-4 orders of magnitude lower than that of nickel (2.14×10^4 [S/cm]) at 1000 [^{o}C] [32]. Thus, added advantages of both of these materials have been combined in the form of nickel and ceria composite and cells are tested for syngas applications with promising results compared to Ni/YSZ cermet [33, 34]. Besides nickel/ceria cermet, copper/ceria cermet has also been tested in a syngas with superior performance than Ni/YSZ cermet [35]. In copper/ceria cermet, copper primarily provides an electronic conductivity to the anode and is otherwise catalytically inert [36]. While major focus of these studies was development of a better performing anode, very little attention has been paid on understanding the electrochemistry of fuel oxidation on ceria. Available knowledge of possible reaction mechanism(s), rate-limiting processes, and WGS catalytic activity of ceria at SOFC operating conditions is very limited [3, 32, 37–39]. Therefore, it is essential to investigate the reaction kinetics on nickel and ceria separately in order to realize commercialization of nickel/ceria cermet electrode cells.

Studying reaction kinetics with porous and cermet electrodes has some inherent disadvantages. For example, gas diffusion impedance of cermet electrode cells can dominate over reaction kinetics [40]. Since the objective of this work is to study the kinetics, all such effects arising out of geometrical parameters need to be avoided. Hence, we use pattern electrode cells where the electrode geometry is well defined and the reactions can be localized. Since current drawn is very small, gas diffusion impedance is not expected to play any significant part in determining the response [29]. Impedance spectra obtained are also expected to be easier to analyze. In this work, we comprehensively explore the electrochemical oxidation of syngas on nickel (section 2.3) and ceria anodes (section 2.4) separately in both dry and wet gas environments. Experimental and

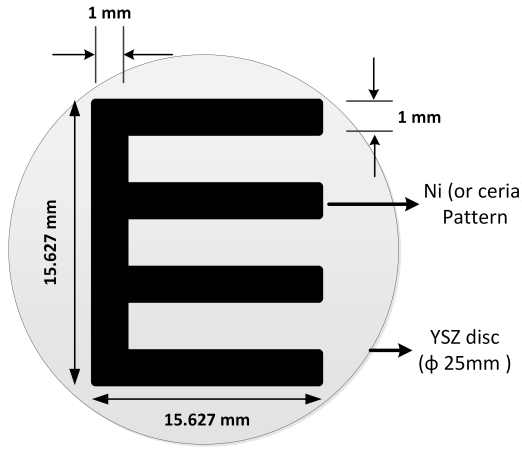

Figure 2.1 A schematic of the pattern electrode

theoretical approaches are explained in the following section.

2.2 Experimental and modeling methodology

2.2.1 Cell preparation

Electrolyte supported nickel and ceria pattern electrode cells are used in this study. Symmetrical cell configuration was chosen to study the anode processes. 8 % YSZ substrates (25 [mm] diameter and 250 [μm] thick) were obtained from Fuel cell materials (www.fuelcellmaterials.com). Nickel and ceria were deposited on YSZ substrate through a stainless-steel mask using DC magnetron sputtering (AJA International, ATC 2600 UHV). Thickness of nickel and ceria patterns was 1.780 [μm] and 500 [nm], respectively. Details of sputtering process are reported elsewhere [3, 41]. Figure 2.1 shows schematic of the pattern electrode. Area specific triple-phase boundary (TPB) length of nickel patterns is 0.2027 [m/cm^2].

2.2.2 Cell test station

A schematic representation of quartz reactor tube containing ceramic cell holder is shown in figure 2.2. Cell was placed between two macro-porous ceramic supports; acting as gas distributors as well. Gold

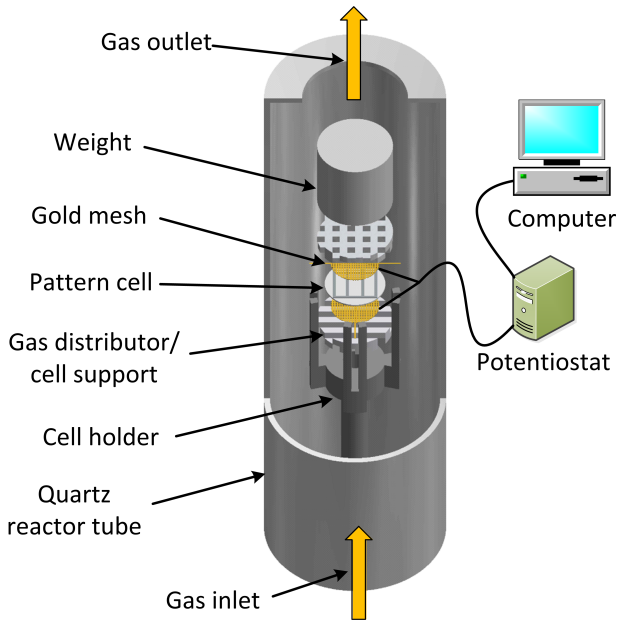

Figure 2.2 Symmetrical cell test station

mesh was applied on both sides of the cell for current collection. A small weight was placed on the top distributor to ensure a good contact between gold mesh and the cell. Quartz tube was placed inside a temperature controlled furnace for testing at a desired temperature. For humidified experiments, the gas mixtures were saturated in a temperature controlled humidifier.

Before electrochemical characterization, cells were heated to 850 [^{o}C] at a ramping rate of 30 [^{o}C/hr]. After achieving the target temperature, gas stream was slowly switched from nitrogen to hydrogen fuel. After a delay of 25 [hrs] – for stabilization, structural reconfiguration, and reduction in case of ceria – electrochemical impedance spectroscopy (EIS) was carried out using Gamry Potentiostat (R600). EIS measurements were conducted with AC perturbation of 10mV, between 700 to 850 [^{o}C], and in a frequency range of 100 to 0.01 [Hz]. The consecutive spectra were recorded with a time delay of at least 1 [hr]. Gas compositions tested in this study are given in table 2.1.

Gas environment	Fuel no.	Syngas composition (vol %)			
		H_2	CO	H_2O	CO_2
Dry	F1	50	0	0	50
	F2	40	10	0	50
	F3	30	20	0	50
	F4	20	30	0	50
	F5	0	50	0	50
Wet	F6	96	0	4	0
	F7	72	24	4	0
	F8	48	48	4	0
	F9	28	68	4	0
	F10	0	96	4	0

Table 2.1 Dry and wet syngas compositions tested in this study

2.2.3 Equivalent circuit model (ECM)

Impedance modeling was done by defining an appropriate equivalent circuit model [3] as shown in figure 2.3. Two R-CPE elements connected in series with electrolyte resistance (Re) are associated to two dominant polarization processes i.e., a high-frequency process (R1-CPE1) and a low-frequency process (R2-CPE2). CPE is a constant-phase element indicating a distributed capacitance. Impedance of this equivalent circuit (Z_{EC}) is given as;

$$Z_{EC} = Re + \frac{R_1}{1 + R_1 Q_1 (i\omega)^{n_1}} + \frac{R_2}{1 + R_2 Q_2 (i\omega)^{n_2}} \tag{2.4}$$

here, R_i [Ω] represents resistance, and Q_i [Fs^{n-1}] and n_i are frequency-independent CPE parameters. The relaxation frequency (f_s) and equivalent capacitance (C_{eq}) of a process described by an R-CPE circuit can be written as;

$$f_s = \frac{1}{2\pi \sqrt[n_i]{R_i Q_i}} \tag{2.5}$$

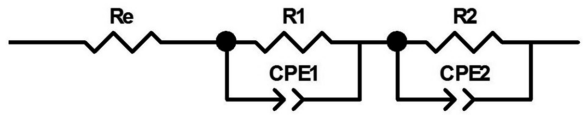

Figure 2.3 Equivalent circuit model (ECM)

$$C_{eq} = \frac{\sqrt[n_i]{R_i Q_i}}{R_i} \tag{2.6}$$

2.2.4 Elementary kinetic model

Relevant equations for elementary kinetic modeling are given in table 2.2. Elementary reactions for hydrogen and CO electrochemical oxidation on nickel and ceria anodes along with their kinetic parameters are given in tables 2.3 and 2.4. Reaction mechanisms for hydrogen and CO oxidation on nickel are taken from [42] and [43, 44], respectively. Thermodynamic and kinetic parameters are also adopted from the same. The reaction mechanisms of hydrogen and CO oxidation on ceria are adopted from [37].

Since the whole ceria surface is catalytically active, lateral diffusion of ceria surface species is considered unimportant. So, the relevant mass transfer (reaction-diffusion) equations for ceria reduce to ordinary differential equations. Further, for the sake of convenience, transport of electrons and ions in ceria bulk is considered very fast. A detailed treatment of bulk transport is presented in chapter 3. For nickel and YSZ surface species, coverage of each surface species was calculated by solving coupled partial differential equations using Chebfun [45] function in Matlab software.

During simulation, rate coefficients for charge-transfer reactions of individual hydrogen and CO oxidation were manually varied to obtain the best fit of experimental impedance spectra. Other parameters like capacitance values and CPE exponents were kept the same as obtained by ECM fitting. Thus, fixing the parameters obtained by ECM fitting reduced the number of free fit parameters in kinetic modeling and focus could be asserted on the charge-transfer process. For simulation of

Physico-chemical process	Relevant equation
Conservation of surface species	$\frac{\partial}{\partial t}\theta_i = \frac{\sigma_i}{\Gamma_k}\dot{s}_i + \frac{\partial}{\partial x}J_i^{surf}$
Diffusion flux	$J_i^{surf} = -D_i^{surf}\frac{\partial}{\partial x}\theta_i$
Specie production rate	$\dot{s}_i = \sum_m v_{i,m}\left(k_{f,m}\prod c_{i,r}^{vr} - k_{b,m}\prod c_{i,p}^{vp}\right)$
Forward reaction rate constant	$k_{f,m} = k_{f,m}^0 T^{\beta_m} exp\left(-\frac{E_m^{act}}{RT}\right)$
Backward reaction rate constant	$k_{b,m} = k_{f,m} exp\left(\frac{\Delta G_m}{RT}\right)$
Diffusion coefficient	$D_i^{surf} = D_i^0 exp\left(-\frac{E_i^{act}}{RT}\right)$
Faradaic current	$i_F = zFl_{tpb}\sum_{CTRx}\left(k_{f,ct}\prod c_{i,r}^{vr} - k_{b,ct}\prod c_{i,p}^{vp}\right)$
Forward charge-transfer rate constant	$k_{f,ct} = k_{f,ct}^0 exp\left(-\frac{E_{ct}^{act}}{RT}\right) exp\left(\frac{z\alpha_a F}{RT}\eta\right)$
Backward charge-transfer rate constant	$k_{r,ct} = k_{f,ct} exp\left(\frac{\Delta G_{ct}}{RT}\right) exp\left(-\frac{z\alpha_c F}{RT}\eta\right)$
Voltage perturbation for EIS study	$\eta = V_0 sin(2\pi f t)$
Charge-transfer resistance	$R_{ct} \approx \frac{d\eta}{di_F}$

Table 2.2 A summary of relevant equations of anode half-cell model [42]. i refers to bulk/surface species, m runs over all reactions involving surface/gas, surface/bulk and charge-transfer reactions (r for reactant species, p for product species and ct for charge-transfer).

Elementary Reaction	k_m^0 (or s_m^0)	E_m^{act}
Ni surface reactions		
$H_2O_{gas} + \square_{Ni} \leftrightharpoons H_2O_{Ni}$	$1.4x10^{10}$ $cm^3/mol.s$	0
$H_{2gas} + 2\square_{Ni} \leftrightharpoons 2H_{Ni}$	$9.8x10^{17}$ $cm^5/mol^2.s$	0
$H_{Ni} + O_{Ni} \leftrightharpoons OH_{Ni} + \square_{Ni}$	$5.0x10^{22}$ $cm^2/mol.s$	97
$H_2O_{Ni} + O_{Ni} \leftrightharpoons 2OH_{Ni}$	$5.4x10^{23}$ $cm^2/mol.s$	20.9
$OH_{Ni} + H_{Ni} \leftrightharpoons H_2O_{Ni} + \square_{Ni}$	$3.0x10^{20}$ $cm^2/mol.s$	43
$CO_{gas} + \square_{Ni} \leftrightharpoons CO_{Ni}$	$s_m^0 = 0.5$	0
$CO_{gas} + O_{Ni} \leftrightharpoons CO_{2,gas} + \square_{Ni}$	$1.0x10^{23}$ $cm^3/mol.s$	181.8
$CO_{Ni} + O_{Ni} \leftrightharpoons CO_{2,Ni} + \square_{Ni}$	$2.0x10^{19}$ $cm^2/mol.s$	123.6
$CO_{2,Ni} \leftrightharpoons CO_{2,gas} + \square_{Ni}$	$7x10^{11}$ $1/s$	41.0
YSZ surface reactions		
$H_2O_{gas} + \square_{YSZ} \leftrightharpoons H_2O_{YSZ}$	$6.6x10^{11}$ $cm^3/mol.s$	0
$O^{2-}_{YSZ} + H_2O_{YSZ} \leftrightharpoons 2OH^-_{YSZ}$	$1.6x10^{22}$ $cm^2/mol.s$	9.6
$O^{2-}_{YSZ} + V^{\bullet\bullet}_O \leftrightharpoons O^x_O + \square_{YSZ}$	$1.6x10^{22}$ $cm^3/mol.s$	90.9
$CO_{gas} + \square_{YSZ} \leftrightharpoons CO_{YSZ}$	$s_m^0 = 0.04$	
Charge-transfer reactions		
$H_{Ni} + O^{2-}_{YSZ} \leftrightharpoons OH^-_{YSZ} + \square_{YSZ} + e^-_{Ni}$	fit	134
$H_{Ni} + OH^-_{YSZ} \leftrightharpoons H_2O_{YSZ} + \square_{Ni} + e^-_{Ni}$	fit	134
$O^x_O + \square_{YSZ} \leftrightharpoons O^-_{YSZ} + V^{\bullet\bullet}_O + e^-_{Ni}$	fit	173
$CO_{Ni} + O^-_{YSZ} + \leftrightharpoons CO_{2,gas} + \square_{Ni} + \square_{YSZ} + e^-_{Ni}$	fit	173

Table 2.3 Elementary reactions for hydrogen and CO electrochemical oxidation on nickel [42, 43]. $\square_{Ni}$ is a free adsorption site at nickel surface, $\square_{YSZ}$ a free adsorption site at YSZ surface, O^x_O lattice oxygen in YSZ, $V^{\bullet\bullet}_O$ oxide ion vacancy with an effective charge +2, O^{2-}_{YSZ} oxide ion at YSZ surface, e^-_{Ni} electron in the nickel, and all other species indicate adsorbed species at nickel surface with Ni subscript and YSZ surface species with YSZ subscript. E_m^{act} is in kJ/mol.

Elementary Reaction	k_m^0	E_m^{act}
$H_{2,gas} + 2\square_{ce} \leftrightharpoons 2H_{ads}$	$8x10^{10}$ cm^5/mol^2.s	131.0
$H_{ads} + O_{ce}^{2-} \leftrightharpoons OH_{ads}^{-} + \square_{ce} + e^{-}$	fit	133.0
$H_{ads} + OH_{ads}^{-} \leftrightharpoons H_2O_{gas} + 2\square_{ce} + e^{-}$	fit	133.0
$CO_{gas} + 2O_O^x \leftrightharpoons CO_3^x$	$3x10^{13}$ cm^5/mol^2.s	212.0
$CO_3^x \leftrightharpoons CO_{2,gas} + O_O^x + V_O^{\bullet\bullet} + 2e'$	fit	117.0

Table 2.4 Elementary reactions for hydrogen and CO oxidation on ceria pattern anode [37]. $\square_{ce}$ is a free adsorption site at ceria surface, O_{ce}^{2-} oxide ion at ceria surface, O_O^x lattice oxygen, and $V_O^{\bullet\bullet}$ is oxide ion vacancy. E_m^{act} is in kJ/mol.

syngas mixtures, all other parameters were kept unchanged except the gas-phase activities.

2.3 Oxidation on nickel pattern electrode

Figure 2.4 shows the impedance spectra obtained with nickel pattern electrode cells at 800 [^{o}C] and the activation energies for both high-frequency and low-frequency processes for different syngas compositions in dry and wet gas environments.

2.3.1 Oxidation in dry environment

Figure 2.4a shows that the polarization resistance for CO oxidation (F5) is almost 2.5 times higher than that of hydrogen (F1). Higher polarization resistance and lower cell performance with CO compared to hydrogen are reported for nickel pattern electrode cells [3, 12, 16, 35, 46, 47]. With the addition of small amounts of hydrogen to CO gas stream, the polarization resistance drops drastically. Sudden drop in the polarization resistance is attributed to the hydrogen preferential oxidation, here termed as "H_2-PROX". Further increase in the hydrogen fraction causes only a gradual decrease in the polarization resistance. Effect of hydrogen oxidation kinetics is so significant that the impedance spectra for all CO/H_2 mixtures (F2-F4) is much closer to that of hydrogen (F1) than CO (F5).

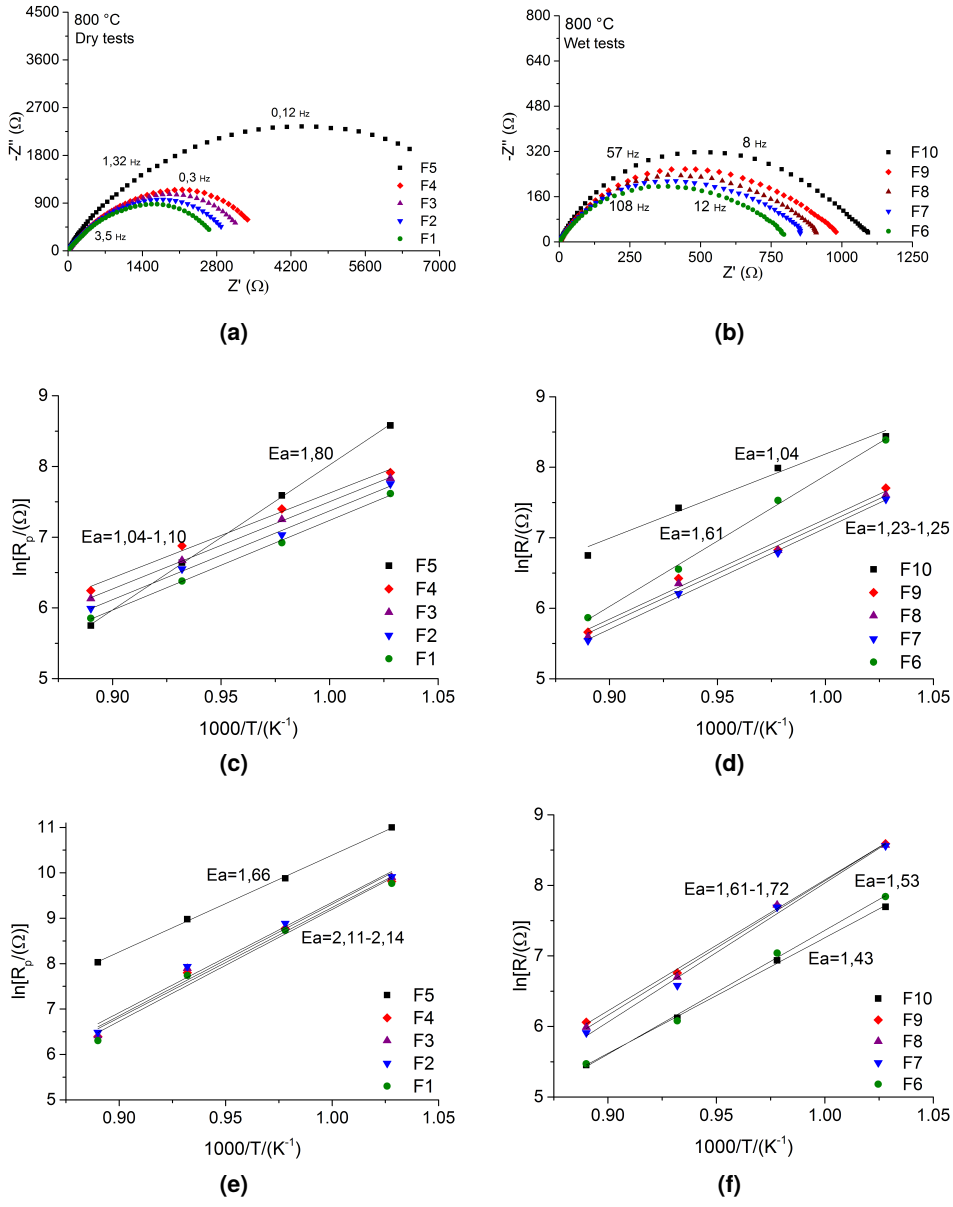

Figure 2.4 EIS and ECM fitting results for syngas oxidation on nickel: impedance spectra at 800 °C (a and b), Arrhenius plot for high-frequency process (c and d), and Arrhenius plot for low-frequency process (e and f). Figures on the left are for dry environment and figures on the right are for wet environment.

Parameter	Gas atmosphere		
	H_2/H_2O	CO/CO_2	CO/H_2O
Q_1	$6.2x10^{-3}$	$2.0x10^{-4}$	$5.6x10^{-4}$
Q_2	$6.4x10^{-4}$	$2.1x10^{-4}$	$3.7x10^{-4}$
n_1	0.67	0.7	0.77
n_2	0.60	0.66	0.70

Table 2.5 ECM fitting parameters for fuel oxidation on nickel

Impedance spectra are also fitted to the equivalent circuit, shown in figure 2.3. The fitting parameters for three gas environments are provided in table 2.5. Figure 2.4c and 2.4e shows temperature dependence of high-frequency and low-frequency processes, respectively. The activation energies of both processes are almost the same for hydrogen and CO/H_2 mixtures, that supports the argument of H_2-PROX. In CO/CO_2 environment, the high-frequency process is found to be highly thermally activated (Ea = 1.80 eV) and attributed to the electrochemical/ charge-transfer process. Low-frequency activation energy is also relatively high (Ea = 1.66 eV), that makes difficult to identify a rate-limiting process. Possible rate-limiting processes are discussed elsewhere [3, 4].

2.3.2 Oxidation in wet environment

Figure 2.4 show the impedance spectra (2.4b) and Arrhenius plot (2.4d and 2.4f) for hydrogen, CO, and CO/H_2 mixtures oxidation in a wet environment (4 % moisture). It is noticed that the polarization resistance for wet hydrogen oxidation (F6) is only one fourth of the resistance observed in case of dry hydrogen oxidation (F1). Similarly, the polarization resistance for wet CO oxidation (F10) is less than one sixth of the resistance observed in case of dry CO oxidation (F5). Relaxation frequencies for both low and high-frequency processes also increased by more than an order of magnitude. This indicates that adding water to hydrogen or CO gas stream strongly stimulates the oxidation process. The accelerating effect of water addition on hydrogen oxidation process is documented [5, 48, 49]. While the effect on CO oxidation is possibly

related to the heterogeneous WGS conversion and a subsequent hydrogen preferential oxidation. Unlike dry gas environment, adding hydrogen to wet CO does not lead to a drastic decrease in the polarization resistance. Rather, the polarization resistance gradually decreases from wet CO (F10) to wet hydrogen (F6).

Activation energies of high-frequency and low-frequency processes for hydrogen oxidation are 1.61 and 1.43 eV, respectively. It is clear that the high-frequency process is highly thermally activated which usually points towards an electrochemical charge-transfer like process. High-frequency activation energies for CO/H_2 mixtures lie between the values obtained for wet hydrogen and wet CO gas environments. The effect of increasing steam partial pressure in CO gas stream on the polarization resistance and relaxation frequency is shown in figure 2.5. Increasing steam partial pressure decreases the polarization resistance decreases and increases the relaxation frequency for both high-frequency and low-frequency process.

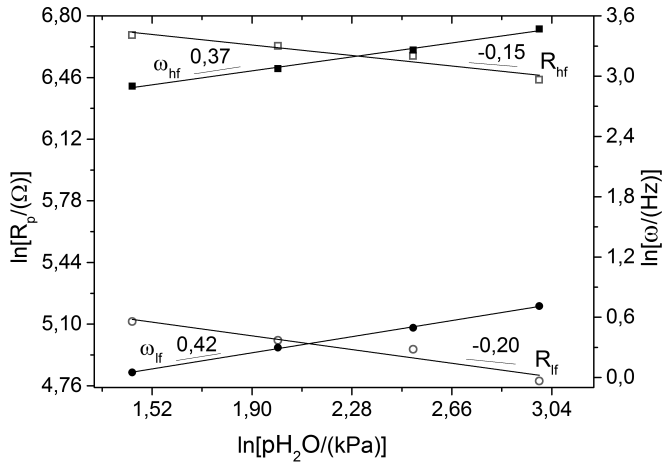

Figure 2.5 Dependence of polarization resistance and relaxation frequency on p_{H_2O} for nickel pattern electrode cells at 800 [°C]. hf and lf refer to the high-frequency and low-frequency processes, respectively.

2.3.3 Simulation results

Figure 2.6 shows experimental and simulated impedance spectra for H_2/H_2O, CO/CO_2, and wet CO environments. Charge-transfer rate-

coefficients for H_2/H_2O and CO/CO_2 systems were the only free fit parameters in this simulation. The resolved coefficients were then used for simulating wet CO and CO/H_2 mixtures. This approach resembles to the one adopted in [21], where hydrogen and CO co-oxidation was simulated by merging the kinetics of both hydrogen and oxygen spillover mechanisms. The simulated impedance spectra in figure 2.6 correspond to the Eq. 2.4 and equivalent circuit shown in figure 2.3. The capacitance and exponent values for high-frequency and low-frequency processes are shown in table 2.5.

The results indicate a reasonably good qualitative agreement between experimental and simulated spectra for H_2/H_2O and CO/CO_2 environments, however, slightly over-predicts the polarization resistance for wet CO. The misalignment between experimental and simulated peaks for wet CO is apparent on Bode plots (figure 2.6b) as well: the simulations predict that the peak occurs at lower frequencies than the observed ones. Further optimization of the model for co-oxidation may address this discrepancy. The simulated rate of charge-transfer reactions for hydrogen and CO oxidation in wet CO environment (F10) are found to be $6.9\text{x}10^{-11}$ and $1.2\text{x}10^{-11}$ [mol/cm^2.s], respectively. Clearly the rate of charge-transfer reaction for hydrogen oxidation is higher than CO despite of very low hydrogen equivalent concentration.

Figure 2.7 compares the impedance spectra resulting from all three current calculation scenarios: a) from hydrogen oxidation only ($i_F = i_{H_2}$), b) from CO oxidation only ($i_F = i_{CO}$), and c) if both hydrogen and CO contribute to the total faradaic current ($i_F = i_{H_2} + i_{CO}$). It can be seen that the impedance spectrum simulated by considering only hydrogen oxidation is closer to the experimental spectrum than considering CO oxidation alone. This indicates that during oxidation of wet CO, a larger fraction of current is produced from hydrogen oxidation. This is also in line with the argument of hydrogen preferential oxidation. Considering co-oxidation, a slightly better match with the experimental spectrum is found which created an interest to quantify the current fractions produced from both hydrogen and CO oxidation.

Hydrogen current fraction is defined as the ratio of current produced by hydrogen oxidation to the total current produced by hydrogen and

CO co-oxidation. Hydrogen current fraction as a function of hydrogen fraction in syngas is shown in figure 2.8. It is found that at a very low hydrogen concentration (5 %), almost 85 % current is solely produced by hydrogen oxidation. While remaining 15 % current is obtained from CO oxidation. That is why, best match to the experimental data in figure 2.7 is obtained from co-oxidation. With increase in hydrogen fraction, hydrogen current fraction also increases. For example, at equimolar hydrogen and CO concentration, hydrogen current fraction is almost 0.97 which indicates that direct CO oxidation is negligible.

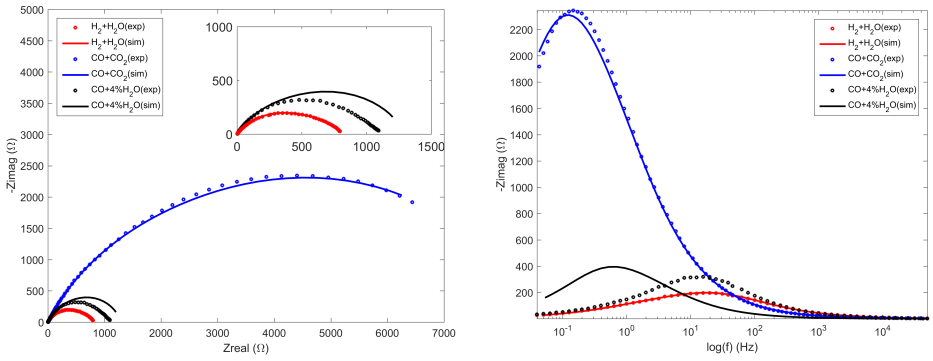

Figure 2.6 Elementary kinetic model fitting and experimental data for nickel pattern electrode cells for H_2/H_2O, CO/CO_2, and wet CO systems. a) Nyquist plots b) Bode plots. exp indicates the experimental and sim indicates the simulated data.

2.4 Oxidation on ceria pattern electrodes

The impedance spectra and activation energies for syngas oxidation on ceria pattern anodes are shown in figure 2.9.

The impedance spectra show two clearly distinct arcs; a relatively small and depressed arc at high-frequency end (figure 2.9a and 2.9b insets) and the main impedance arc at low-frequency end. The polarization resistance of high-frequency process is significantly lower than that of low-frequency, therefore, not considered to be the rate-limiting. Main characteristics of high-frequency process at 800 [°C] are shown in table

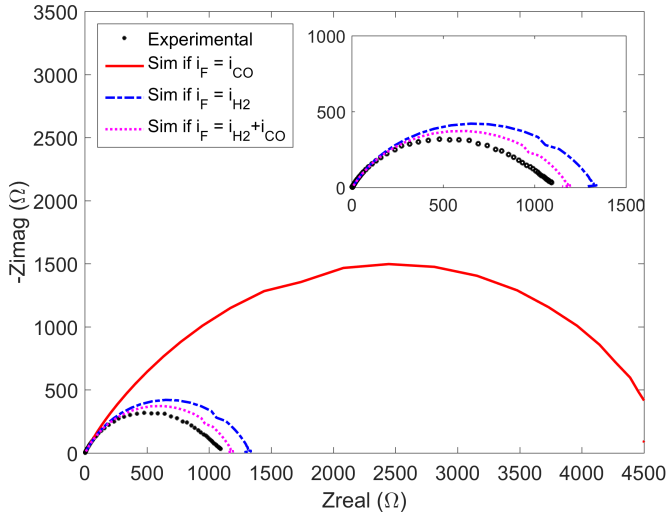

Figure 2.7 The simulated impedance spectra with nickel if faradaic current is a result of hydrogen (i_{H_2}), CO (i_{CO}), or H_2+CO ($i_{H_2} + i_{CO}$) oxidation. Experimental data is also shown for comparison.

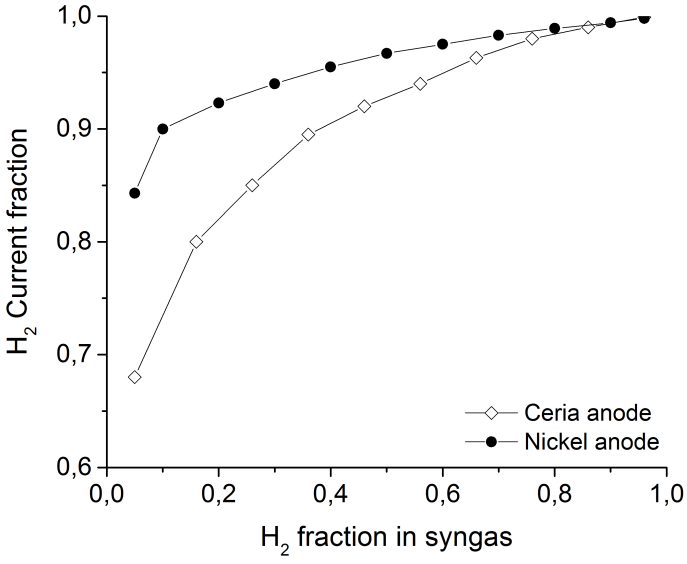

Figure 2.8 Effect of hydrogen fraction in a syngas on hydrogen current fraction at 800 [^{o}C]

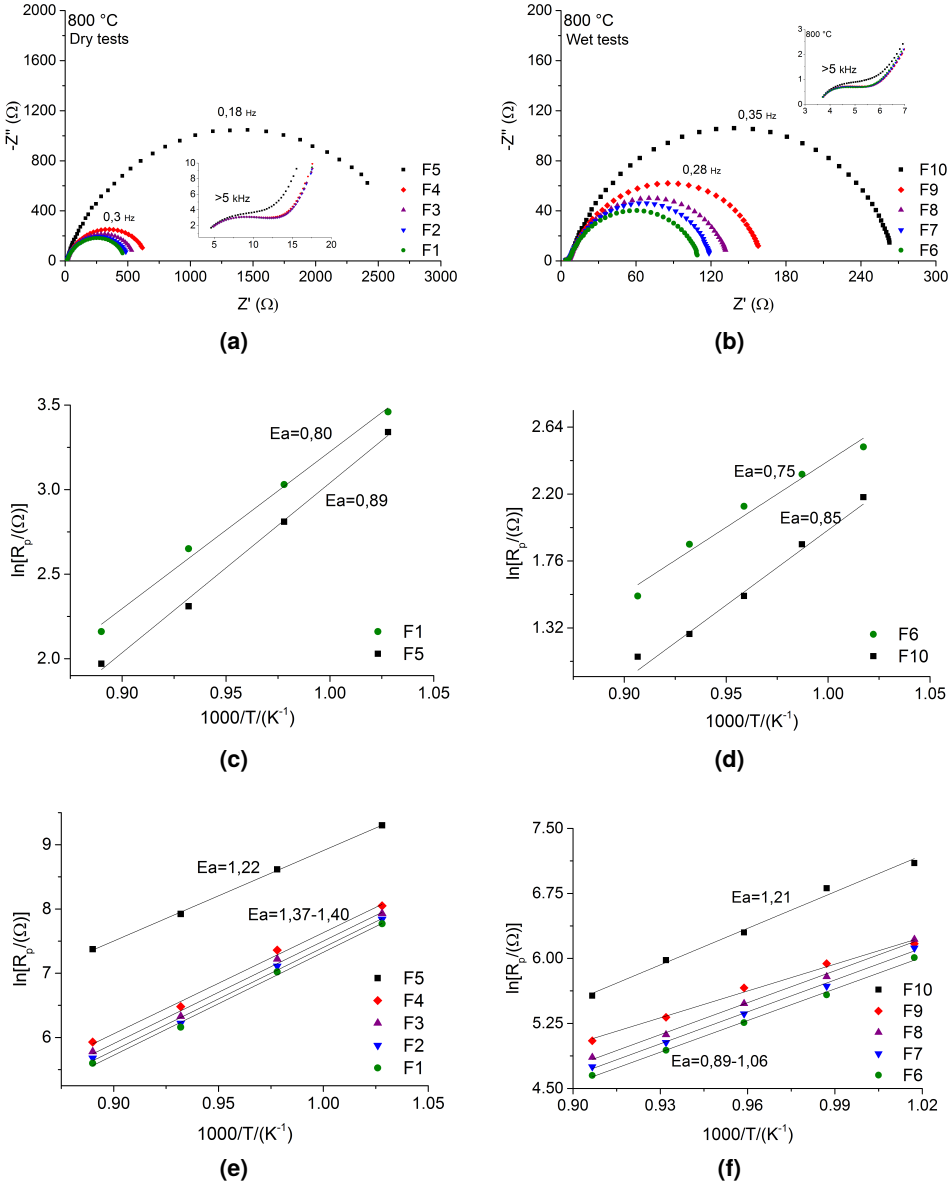

Figure 2.9 EIS and ECM fitting results for syngas oxidation on ceria: impedance spectra at 800 [°C] (a and b), Arrhenius plot for high-frequency process (c and d), and Arrhenius plot for low-frequency process (e and f). Figures on the left are for dry environment and figures on the right are for wet environment.

Parameter	dry H_2	dry CO	wet H_2	wet CO
E_a [eV]	0.80	0.89	0.75	0.85
f_s [kHz]	6.92	5.48	20.52	7.86
C_{eq} [μF.cm^{-2}]	5.30	1.31	1.14	9.11

Table 2.6 Typical characteristics of high-frequency arc observed with ceria pattern electrode cells. f_s and C_{eq} are given at 800 [°C]

2.6. It is found that the gas environment does not considerably influence the polarization resistance and activation energy of high-frequency process. Further, the equivalent capacitance values are mainly independent of temperature. Both of these observations suggest that the high-frequency process cannot be related to a charge-transfer process. Similar arcs at high-frequency end were also observed in other studies and attributed to a grain boundary effect [50, 51] and poor contact between electrode and current collector [52]. The equivalent capacitance implied for the low-frequency arc is of the order of 0.1–1.0 mF/cm^2, that is a characteristic of gas/solid interface [53]. Therefore, the resistance associated with the low-frequency arc is attributed to electrochemical reaction at gas/ceria interface and discussed here in detail.

2.4.1 Oxidation in dry environment

Impedance spectroscopy reveals that the polarization resistance of fuel oxidation on ceria is much lower than on nickel for all gas environments tested here. Previously, this observation was related to a larger electrochemically active region on ceria compared to nickel [29]. Figure 2.9a shows that the polarization resistance for CO oxidation (F5) is almost five times higher than for hydrogen oxidation (F1). Whereas, this difference was only 2.5 times in case of nickel (figure 2.4a, F5 vs F1). Surface characterization techniques like XPS and IR have shown the formation of intermediate carbonate species on ceria surface when exposed to CO [39, 54]. Decomposition of these intermediates to produce gas phase CO_2 is highly energy demanding. Therefore, very high polarization resistance for CO relative to hydrogen may be attributed to a high

surface coverage of carbonate species with decomposition/desorption step as the rate-determining [37, 55].

Adding a small amount of hydrogen to CO (F4), drops the polarization resistance drastically indicating H_2-PROX. Further increase in hydrogen fraction does not lead to a substantial drop in the polarization resistance. Effect of hydrogen oxidation kinetics is so significant that the size of impedance spectra for all syngas mixtures (F2-F4) is much closer to hydrogen (F1) than to CO (F5). Low-frequency activation energies for syngas oxidation (figure 2.9e) are also similar to that of hydrogen oxidation. It is, therefore, speculated that hydrogen preferentially oxidizes in syngas, while CO mainly forms surface carbonates and inhibits hydrogen adsorption and subsequent oxidation. Possible reaction mechanisms and the rate-limiting processes for electrochemical oxidation of hydrogen and CO are detailed elsewhere [3, 37].

2.4.2 Oxidation in wet environment

Impedance spectra of hydrogen, CO, and syngas oxidation in wet environment are shown in figure 2.9b. When compared with dry environment (figure 2.9a), it is noticed that the polarization resistance for wet hydrogen oxidation (F6) is only one fifth of the resistance observed in case of dry hydrogen oxidation (F1). Similarly, the polarization resistance for wet CO oxidation (F10) is less than one tenth of the resistance observed for dry CO oxidation (F5). Interestingly, the polarization resistance for CO (F10) is still almost twice of hydrogen (F6). Whereas, polarization resistance for hydrogen oxidation on nickel was only 40 percent higher than that of CO oxidation. Relatively higher resistance for CO oxidation on ceria may be related to the formation of surface carbonates. The low-frequency energies for wet environment are shown in figure 2.9f. It is found that the low-frequency activation energy for CO oxidation is the same in both dry and wet gas environment. This suggests that adding water to CO does not affect the rate limitations. Conversely, adding water to hydrogen (F6) and syngas mixtures (F7-F9) drops the activation barrier significantly. While surface chemistry and charge-transfer processes are lumped together in the main arc, it is difficult to separate them and quantify the effect of steam addition on individual process. The effect of varying steam partial pressure on wet CO electrochemistry

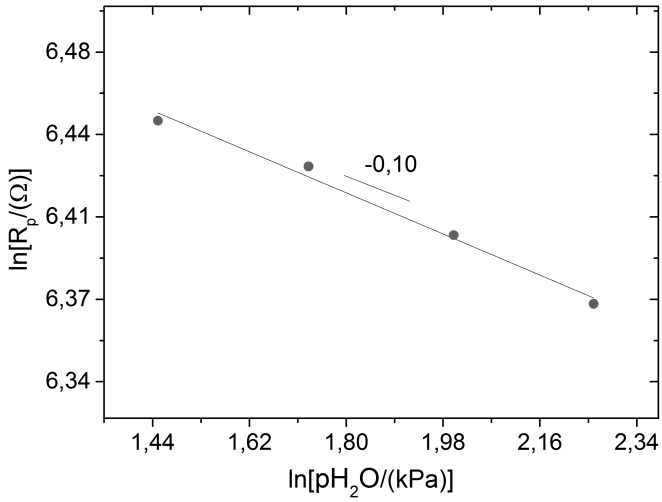

Figure 2.10 Dependence of polarization resistance on p_{H_2O} observed using ceria pattern electrode cells at 780 [°C]

is shown in figure 2.10. It can be seen that the polarization resistance decreases when amount of water in the fuel gas is increased. This is in line with the observation made in case of nickel (figure 2.5). However, the slope of ln[pH_2O] vs ln[Rp] curve for ceria is found to be -0.10, that is slightly higher (= -0.15) in case of nickel . This observation suggests that the addition of water has more accelerating effect on the overall CO oxidation process on nickel compared to ceria.

2.4.3 Simulation results

Elementary reactions for hydrogen and CO oxidation on ceria are given in table 2.4. Model fitting and experimental data for all three gas environments (H_2/H_2O, CO/CO_2, and wet CO) are shown in fig 2.11. The rate of charge-transfer reactions for hydrogen and CO oxidation in wet CO environment are found to be 10.0x10^{-11} and 5.5x10^{-11} [mol/cm^2.s], respectively. Interestingly, the rate of hydrogen oxidation in wet CO environment is only twice of the rate of CO oxidation. The impedance spectra resulting from all three current calculation scenarios as explained in section 2.3.3 are compared in fig 2.12. It can be seen that neither current obtained from CO oxidation ($i_F = i_{CO}$) nor from hydrogen oxidation ($i_F = i_{H_2}$) matches the experimental spectrum. Rather a co-oxidation

of hydrogen and CO ($i_F = i_{H_2} + i_{CO}$) gives best qualitative representation of the experimental spectrum. Similar to nickel pattern electrode cells, a misalignment between experimental and simulated peaks is also apparent for wet CO (figure 2.11b). The relative contribution of hydrogen and CO oxidation in a syngas is simulated and shown in figure 2.8. It is found that, though hydrogen current fraction is higher than that of CO, yet it is much lower than the fraction found in case of nickel pattern electrode cells. For 5 % hydrogen in syngas, only 68 % current is produced from hydrogen oxidation. At equimolar concentrations, almost 93 % current is obtained from hydrogen oxidation and remaining 7 % from CO. This indicates that while studying syngas oxidation on ceria, electrochemical oxidation of CO cannot be ignored.

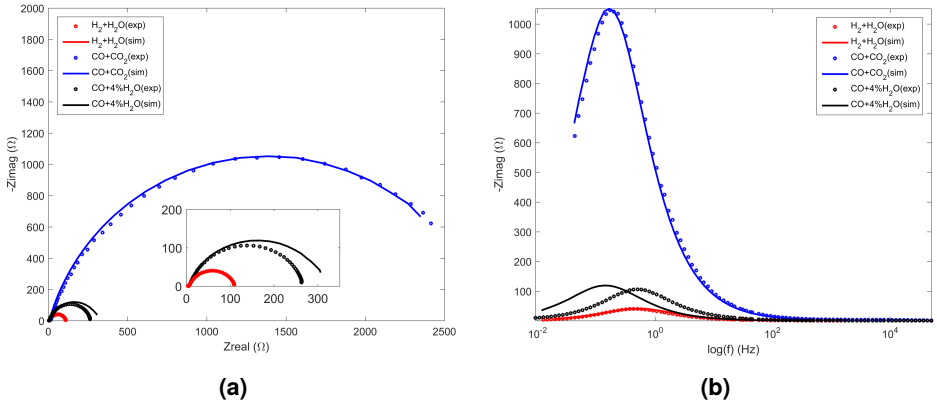

Figure 2.11 Elementary kinetic model fitting and experimental data on ceria pattern electrodes for H_2/H_2O, CO/CO_2, and wet CO (4 % H_2O systems: a) Nyquist plots b) Bode plots.

2.5 Comparison between nickel and ceria pattern electrodes

Based on results discussed in the previous sections, nickel and ceria are compared with respect to: 1) the cell performance in hydrogen and CO, 2) the hydrogen preferential oxidation in syngas, and 3) the effect of hydrogen concentration on hydrogen current fraction.

Polarization resistance for the oxidation of hydrogen (F1), CO (F5),

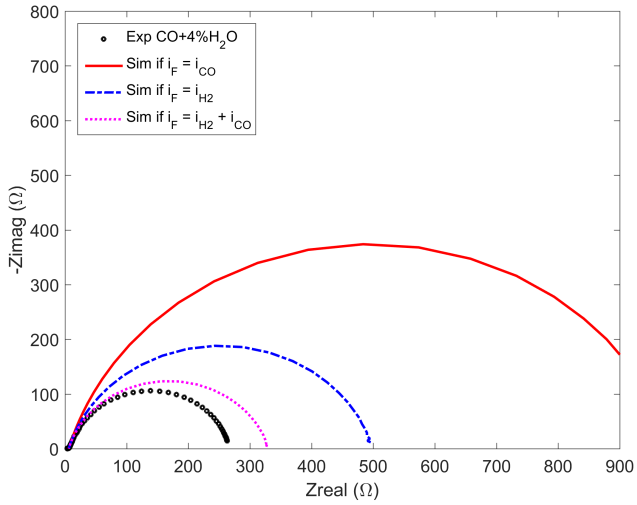

Figure 2.12 The simulated impedance spectra with ceria pattern electrode cells if faradaic current is a result of hydrogen (i_{H_2}), CO (i_{CO}) and H_2+CO (i_{H_2} + i_{CO}) oxidation. Experimental data is also shown for comparison.

and CO/H_2 mixture (F4) in dry environment are compared in table 2.7. Better cell performance with hydrogen than with CO on nickel is in line with the literature [3, 12, 16, 35, 46, 47]. However, the cell performance with hydrogen and CO on ceria is contradictory to the reported trend [35, 56]. In [35], it is observed that the cell performance with Cu/CeO_2/YSZ anode is identical when using either hydrogen or CO, whereas we found very high polarization resistance for CO in comparison to hydrogen. It is worthwhile remembering that, oxidation on both pure ceria and Cu/CeO_2 is expected to take place only on ceria phase [36]. Similarly, Graves et al. [56] reported higher electrocatalytic activity of gadolinium-doped ceria (GDC) in CO/CO_2 environment than in H_2/H_2O. Due to apparently inconsistent trends between these studies, further investigations are suggested.

In case of CO/H_2 mixture, the polarization resistance is closer to that of hydrogen compared to CO. This clearly indicates that the oxidation process of mixtures resembles to the hydrogen oxidation instead of CO, which we regard as the hydrogen preferential oxidation. This effect is observed with both nickel and ceria pattern electrode cells. Using nickel pattern electrode cells, better cell performance with CO/H_2 mixtures

Fuel gas ID	Polarization resistance (ohm)	
	nickel pattern electrode cells	ceria pattern electrode cells
F1 (H_2)	2890	480
F4 (CO/H_2)	3860	670
F5 (CO)	8600	2750

Table 2.7 Polarization resistance for hydrogen (F1), CO (F5) and CO/H_2 mixture (F4) oxidation on nickel and ceria pattern electrode cells

than CO is reported as discussed in section 2.1. However, using ceria pattern electrode cells, such studies are not known to our knowledge besides preliminary results presented by our group previously [3].

Electrochemical co-oxidation of hydrogen and CO is studied by elementary kinetic modeling. In a wet CO (F6) environment, the rate of charge-transfer reactions for CO is almost one sixth of hydrogen on nickel and only half of hydrogen on ceria. These reaction rates correspond to the hydrogen current fraction of 0.85 and 0.65 for nickel and ceria, respectively. Then hydrogen current fraction is further evaluated for a wide range of hydrogen fractions in syngas (figure 2.8). It is found that, increasing hydrogen fraction in a syngas, increases the hydrogen current fraction for both nickel and ceria. For an equimolar syngas mixture, the hydrogen current fraction is found to be 0.97 for nickel and 0.93 for ceria.

2.6 Conclusions:

In this study, electrochemical oxidation of hydrogen, CO, and syngas was investigated in both dry and wet gas environments using EIS. Further, elementary kinetic model was developed to understand hydrogen and CO co-oxidation. The main results are summarized as:

- The polarization resistance for hydrogen oxidation was less than CO oxidation for both nickel and ceria pattern electrode cells. The polarization resistance for syngas oxidation was closer to that of

hydrogen oxidation than CO. The activation energies for syngas were similar to that of hydrogen oxidation. These observations led to a conclusion that the oxidation of syngas dominantly resembles hydrogen oxidation and hydrogen is preferentially oxidized.

- Addition of water to CO lead to a significantly larger drop in the polarization resistance compared to the drop caused by addition of water to hydrogen. However, the polarization resistance for CO/H_2 mixture was still higher than H_2/H_2O mixture. Larger drop in the polarization resistance in former case was attributed to the combined effect of water-gas shift conversion and preferential oxidation of hydrogen produced via CO conversion. Preferential oxidation of hydrogen produced via water-gas-shift conversion was also captured by the kinetic model.

- Majority of the membrane-electrode assembly (MEA) models neglect CO electrochemistry in CO/H_2 mixtures assuming that hydrogen is the only electrochemically active species while CO undergoes WGS transformation. In this study, simulation has shown that CO may also electrochemically oxidize depending upon its concentration in syngas. The hydrogen current fraction was found higher on ceria compared to nickel for all simulated gas mixtures. For confirming and better understanding of the relatively larger contribution of CO electrochemistry in case of ceria, further investigations are required.

This page is intentionally left blank

3

A detailed look into hydrogen electrochemical oxidation on ceria

In Chapter 2, we discovered that the mechanistic details of fuel oxidation on ceria anodes are far less investigated, than those on nickel anodes. Even the mechanism of hydrogen oxidation, charge transfer process, and rate-determining step are not clear. One of the reasons is the complex mixed ionic and electronic conducting (MIEC) nature of ceria. In the present work, we study hydrogen electrochemical oxidation on a ceria using the Nernst-Planck-Poisson model and a detailed reaction mechanism. The resistance caused by surface kinetics, and bulk transport of oxide-ions vacancies and electrons are computed individually to identify the dominant resistive process. The effect of operating conditions like temperature and gas-phase composition on the polarization resistance is evaluated and compared with the experimental data obtained by the electrochemical impedance spectroscopy (EIS).

This chapter has been published as: A.N. Tabish, H.C. Patel, J. Schoonman, and P.V. Aravind. A detailed look into hydrogen electrochemical oxidation on ceria anodes. Electrochimica Acta 283 (2018) 789-797

3.1 Introduction

Ceria is one of the extensively studied mixed ionic and electronic conducting (MIEC) material and inherits outstanding redox properties [57]. It is widely used as a three-way catalyst in automotive industry as well as a promoter for water-gas shift conversion, thermochemical water splitting, and various other catalytic reactions [58]. In the recent years, ceria has gained a considerable attention as an SOFC anode material due to its ability of oxidizing carbon containing fuels [2, 59] and extended electrochemically active area. Doping ceria with trivalent elements like gadolinium and samarium enhances the oxygen vacancy concentration and hence its ionic conductivity [60]. The electronic conductivity of pure ceria in reducing environment is low, almost 3-4 orders of magnitude lower than nickel at 1000 ^{o}C [32]. Therefore, metal/ceria composites are preferred over pure ceria for anode applications.

While nickel/ceria cermets exhibit an excellent electrochemical performance [61, 62], their fundamental electrochemistry is poorly understood. The lack of understanding is mainly due to complexity of MIEC nature of ceria and uncertainty in relative significance of the two-phase boundary (2PB) between ceria surface and gas-phase, and the triple-phase boundary (TPB) between nickel, ceria, and gas-phase. This is unlike conventional nickel/YSZ cermets where electrochemical reactions are only restricted to the TPB between nickel, YSZ, and gas-phase. Recently, Shishkin et al. [63, 64] studied the electrochemical properties of nickel/ceria cermets using density functional theory (DFT) and found that the electrochemical fuel oxidation occurs predominantly at ceria surface than at the TPB. This conclusion was based on the observation that the formation of oxide-ion vacancies is more favorable at the ceria surface than at the TPB. While comparing the performance of nickel/GDC and Au/GDC in a H_2/H_2O environment, Lei et al. [65] also argued that the electrochemical reactions mainly occur at the GDC surface and contribution of the TPB is of secondary importance. Therefore, studying the electrochemistry of ceria cermets primarily requires understanding of ceria electrochemistry itself.

Ceria electrochemistry essentially assimilates the kinetics of electrochemical reactions at the 2PB and the bulk transport of oxide-ions

vacancies and electrons. The overall cell impedance is mainly the cumulative response of these processes. Generally, ceria-film thickness is kept of the orders of nano-meters so that the resistance of ionic transport is small enough to be neglected. The impedance of thin-film ceria pattern anode, corresponding to what we measure experimentally, can then be categorized into: 1) drift-diffusion resistance associated with the transport of electrons between current collector and reaction sites at the 2PB (commonly termed as current collector spacing), and 2) surface reaction resistance associated with the charge transfer process at the 2PB. Chen et al. [66] and Ciucci et al. [67] studied these two processes in reducing environment ($H_2 - H_2O - Ar$) at 550–650 ^oC using the Nernst-Planck-Poisson (NPP) model. The authors reported that the drift-diffusion resistance is negligibly small if the spacing is less than 10 μm, indicating sole-role of the reaction resistance. However, with increase in spacing from 10 to 1000 μm, the drift-diffusion resistance increases exponentially such that at spacing > 1000 μm the diffusion resistance becomes the dominant. These results emphasize the need of an efficient current collection mechanism for reaction kinetics studies with MIEC electrodes. Since these studies implied global reaction kinetics, no conclusion can be made on reaction mechanism and charge-transfer process.

Other researchers [3, 32, 38, 68, 69] also studied ceria electrochemistry in $H_2 - H_2O$ environment and proposed reaction mechanisms, charge-transfer processes, and rate-determining step(s). However, these studies do not lead to consensus on charge-transfer mechanism and on rate-determining elementary step. For example, Zhang et al. [38] and Patel et al. [37] considered a two-step charge-transfer process similar to that of hydrogen oxidation on nickel/YSZ, while Feng et al. [69] proposed a single-step electron transfer from the surface hydroxyl ions to the cerium ions, and DeCaluwe et al. [32] considered charge-transfer at ceria/YSZ interface. Similarly, El Fallah et al. [68] proposed hydrogen adsorption, while others [32, 37, 38, 69] suggested charge-transfer as rate-determining elementary step. Knowledge of rate-determining step is a key to further improve the electrode performance. It also helps deriving right expression for exchange-current density – a key parameter to represent the electrochemistry in fuel cell model. Such lack of clarity in charge-transfer process and rate-determining step was the motivation

for this work.

The elementary kinetic modeling approach has been applied for studying reaction mechanisms and identifying rate-determining step(s) [42, 43, 70] on nickel pattern anodes. Previously [37], we conducted a preliminary study, using this approach, to identify rate-determining step for hydrogen electrochemical oxidation on thin-film ceria pattern anodes. For convenience, both anionic and cationic sites were considered equivalent for adsorption/desorption and charge-transfer reactions, whereas, DFT studies have shown that anionic sites are thermodynamically favorable for hydrogen dissociative adsorption than cationic sites [71]. In this work, we revisited the model developed in [37] with a better prediction of thermo-kinetic parameters and differentiating between surface sites. Additionally, bulk transport of oxide-ions vacancies and electrons is also computed using the NPP model to quantify relative significance of the resistance caused by electrochemical reactions and defect transport. The proposed reaction scheme is evaluated over a wide range of temperatures and gas-phase partial pressures. For model validation, results from the electrochemical impedance spectroscopy of hydrogen oxidation over ceria pattern electrode cells are used. A sensitivity analysis is carried out to identify the rate-determining step, based on which a model for the exchange-current density is also developed.

3.2 Theoretical modeling

Figure 3.1 depicts physical domain of the NPP model. Γ_5 refers to the 2PB between ceria and gas-phase where electrochemical reactions occur. Electrons and oxide-ion vacancies produced at Γ_5 during the electrochemical oxidation diffuse into bulk of ceria. The dominant pathways for electron and vacancy transport are from Γ_5 to Γ_4 and from Γ_5 to Γ_1, respectively. Γ_2 and Γ_3 are the symmetric boundaries. Development of detailed reaction mechanism and the NPP model are discussed in the following sections.

3.2.1 Reaction mechanism

Overall reaction for hydrogen electrochemical oxidation on ceria can be written as (Kröger-Vink notation) [72]:

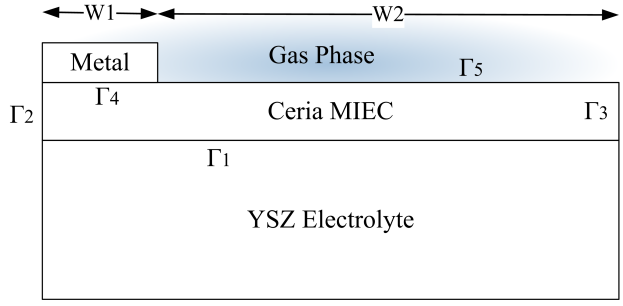

Figure 3.1 Physical domain of the model

$$H_2(g) + O_O^x + 2Ce_{ce}^x \rightleftharpoons H_2O(g) + V_O^{\bullet\bullet} + 2Ce_{ce}^{'} \tag{3.1}$$

where O_O^x is an oxide anion residing on an oxide site, Ce_{ce}^x is a cerium cation (Ce^{4+}) residing on a cation site, $Ce_{ce}^{'}$ is a localized electron at cerium (Ce^{3+}), and $V_O^{\bullet\bullet}$ is an oxide-ion vacancy with an effective charge of 2+. Reaction (3.1) is as overall oxidation reaction that involves several heterogeneous and surface elementary steps, such as: 1) the adsorption and dissociation of hydrogen on a favorable O_O^x or Ce_{ce}^x site, 2) the formation of intermediates such as hydroxyl species, 3) the charge-transfer and transport reactions, and 4) the formation and subsequent desorption of water.

At SOFC operating conditions, the dissociative adsorption of hydrogen on the O_O^x sites is thermodynamically favorable (ΔH = -165.1 kJ/mol) compared to that on Ce_{ce}^x sites [73]. Therefore, it is expected that hydrogen oxidation follows the formation of hydroxyl-ions, whereas hydrogen associative adsorption (ΔH = -3.34 kJ/mol) or the formation of cerium hydroxide (ΔH = 38.8 kJ/mol) are either unlikely or unstable. This leads to the following reaction scheme:

$$H_2(g) + 2O_O^x + 2Ce_{ce}^x \rightleftharpoons 2OH_O^{\bullet} + 2Ce_{ce}^{'} \tag{3.2}$$

$$2OH_O^{\bullet} \rightleftharpoons H_2O_O^{\bullet\bullet} + O_O^x \tag{3.3}$$

$$H_2O_O^{\bullet\bullet} \rightleftharpoons H_2O(g) + V_O^{\bullet\bullet} \tag{3.4}$$

Briefly: gaseous hydrogen dissociatively adsorbs on O_O^x sites and forms two hydroxyl ions ($OH_O^{\bullet}$) as shown in reaction 3.2. This reaction also describes the charge-transfer process where two electrons are transferred from $OH_O^{\bullet}$ to two $Ce_{ce}^{'}$. It is also possible that hydrogen molecule first dissociates near oxide-ions forming two neutral hydroxyl groups followed by the transfer of two electrons to cerium as suggested in the literature [69]. However, due to unavailability of the kinetics of each elementary step, the dissociative adsorption and the charge-transfer are considered as a single elementary step. Such an approach has been reported [74]. In the second step, one of O-H bonds weakens and releases a proton which then combines with the neighboring $OH_O^{\bullet}$ group to form a water molecule (reaction 3.3). Water molecules then desorb from oxide sites creating oxide-ion vacancies (reaction 3.4). Upon formation, these vacancies and electrons diffuse towards their respective boundaries: Γ_1 and Γ_4, respectively. The transport processes between two nearest neighbor lattice sites, x_1 and x_2, can be written as:

$$V_O^{\bullet\bullet}(x_1) + O_O^x(x_2) \rightleftharpoons O_O^x(x_1) + V_O^{\bullet\bullet}(x_2) \tag{3.5}$$

$$Ce_{ce}^{'}(x_1) + Ce_{ce}^x(x_2) \rightleftharpoons Ce_{ce}^x(x_1) + Ce_{ce}^{'}(x_2) \tag{3.6}$$

3.2.2 Surface chemistry

Governing equations for the concentration of surface species are written as:

$$\frac{\partial}{\partial t} c_k = \dot{s}_k \tag{3.7}$$

$$\dot{s}_k = \sum v_{ki} \left(\overrightarrow{k_i} \prod_{reactant} c_k^{v_{ki}} - \overleftarrow{k_i} \prod_{product} c_k^{v_{ki}} \right) \tag{3.8}$$

where $k \in O_O^x, OH_O^{\bullet}, H_2O_O^{\bullet\bullet}, V_O^{\bullet\bullet}, Ce_{ce}^x$, and $Ce_{ce}^{'}$, c_k is the molar concentration of surface specie k (mol/m^2), and $\dot{s}_k$ is the net rate of generation (mol/m^2.s). The concentration of specie k can be expressed as:

$c_k = \Gamma[X_k]$, where Γ represents the available site density at ceria surface [32] (=1.6x10^{-5} mol/m^2) and $[X_k]$ is the fractional coverage. v_{ki} is the stoichiometric coefficient of reactant k in the ith reaction, $\overrightarrow{k_i}$ and $\overleftarrow{k_i}$ are the forward and backward rate coefficients, respectively. To ensure thermodynamic consistency, $\overrightarrow{k_i}$ and $\overleftarrow{k_i}$ are related as:

$$K_i = \frac{\overrightarrow{k_i}}{\overleftarrow{k_i}} = exp\left(-\frac{\Delta H_i^o - T\Delta S_i^o}{RT}\right) \tag{3.9}$$

Eq. 3.7 and Eq. 3.8 are solved simultaneously by applying the conservation of both oxide-ion sites ($\left[O_O^x\right] + \left[OH_O^{\bullet}\right] + \left[H_2O_O^{\bullet\bullet}\right] + \left[V_O^{\bullet\bullet}\right] = 2$) as well as cerium-ion sites ($\left[Ce_{ce}^x\right] + \left[Ce_{ce}^{'}\right] = 1$).

3.2.3 Bulk transport

Transport in the bulk of ceria is modeled by explicit consideration of oxide-ion vacancies ($V_O^{\bullet\bullet}$) and electrons ($Ce_{ce}^{'}$) . Under the assumption that there is no internal source or sink, species conservation in the bulk implies that:

$$\frac{\partial}{\partial t}C_k + \nabla.J_k = 0 \tag{3.10}$$

where k refers to the bulk defects: electrons and oxide-ions vacancies, C_k is the molar concentration (mol/m^3). $\dot{J}_k$ is the species flux (mol/m^2.s) and is related to the gradient of the electrochemical potential ($\tilde{\mu}_k$):

$$J_k = -C_k D_k \nabla \frac{\tilde{\mu}_k}{RT} \tag{3.11}$$

where $\tilde{\mu}_k$ is given by:

$$\tilde{\mu}_k = \mu_i^0 + RTln(a_k) + z_k F\phi \tag{3.12}$$

where a_k (=C_k/C_k^0) is the activity of specie k. In dilute limits where species are non-interacting, the charged species flux can be expressed by the Nernst-Planck equation:

$$J_k = -D_k \nabla C_k - \frac{z_k F}{RT} D_k C_k \nabla \phi \tag{3.13}$$

where z_k is the charge (+2 for oxide-ions vacancy and -1 for electron), F is the Faraday constant, ϕ is the electric potential (V), and D_k is the diffusion coefficient (m^2/s).Under strict neutrality conditions ($\sum z_k J_k = 0$ and $\sum z_k C_k = 0$), the flux of two coupled charged species can alternatively be represented in terms of the ambipolar diffusion coefficient ($\mathscr{D}$)[75].

$$J_k = -\mathscr{D} \nabla C_k \tag{3.14}$$

where $\mathscr{D} = 3D_{V_O^{\bullet\bullet}} D_{Ce_{ce}'} / (2D_{V_O^{\bullet\bullet}} + D_{Ce_{ce}'})$. Eq. 3.14 is only applicable for transport of two defects which is the case of transport in pure ceria under reducing conditions. Charge neutrality further leads to simplification of the Poisson equation.

$$\nabla . \left(\epsilon \nabla \phi \right) = -F \sum z_k C_k = 0 \tag{3.15}$$

where ϵ is the permitivity of ceria (F/m). Eqs. 3.10, 3.13 and 3.15 represent a system of coupled partial differential equations, also known as the NPP model.

Solution of the NPP model requires appropriate definition of the boundary conditions. The simplest boundary condition is at Γ_2 and Γ_3 which follows that there is no change in the electrochemical potentials, therefore no change in the defect concentrations and the electric potential. At MIEC/YSZ interface (Γ_1) electrons are blocked and oxide-ions vacancies can migrate through. Similarly, at metal/MIEC interface (Γ_4) vacancies are blocked and electrons can migrate through. Therefore, $\frac{\partial}{\partial y} \tilde{\mu}_{Ce_{ce}'} \Big|_{\Gamma_1} = 0$ and $\frac{\partial}{\partial y} \tilde{\mu}_{V_O^{\bullet\bullet}} \Big|_{\Gamma_4} = 0$ holds at Γ_1 and Γ_4, respectively [67]. The boundary condition at gas/ceria interface (Γ_5) is relatively complex because of the complicated interactions between oxide-ion vacancies,

electrons, and gas-phase reactants and products. We assume that fluxes of vacancies and electrons at Γ_5 are given by the rate of reaction 3.4 and reaction 3.2, respectively. This follows that $J_{\mathrm{V_O^{\bullet\bullet}}} = \dot{r}_4$ and $J_{\mathrm{Ce_{ce}^{\prime}}} = 2\dot{r}_2$.

3.3 Numerical solution and model validation

We used Matlab® version R2015b and COMSOL® version 5.1 to solve surface concentration and electrochemical potential distribution within ceria bulk, respectively. Table 3.1 summarizes the simulation parameters and Table 3.2, the thermodynamic properties of gas-phase and surface species. To understand the relative importance of the defect transport and the surface kinetics, three resistance terms, i.e. the cross-plane bulk ionic resistance ($R^{CP}_{\mathrm{V_O^{\bullet\bullet}}}$), the in-plane drift-diffusion resistance ($R^{IP}_{\mathrm{Ce_{ce}^{\prime}}}$), and the surface reaction resistance (R_{chem}) are introduced and defined as [67]:

$$R^{CP}_{\mathrm{V_O^{\bullet\bullet}}} = \frac{\left\langle \tilde{\mu}_{\mathrm{V_O^{\bullet\bullet}}} \right\rangle_{\Gamma_1} - \left\langle \tilde{\mu}_{\mathrm{V_O^{\bullet\bullet}}} \right\rangle_{\Gamma_5}}{I^{CP}_{\mathrm{V_O^{\bullet\bullet}}}} \tag{3.16}$$

$$R^{IP}_{\mathrm{Ce_{ce}^{\prime}}} = \frac{\left\langle \tilde{\mu}_{\mathrm{Ce_{ce}^{\prime}}} \right\rangle_{\Gamma_4} - \left\langle \tilde{\mu}_{\mathrm{Ce_{ce}^{\prime}}} \right\rangle_{\Gamma_5}}{I^{IP}_{\mathrm{Ce_{ce}^{\prime}}}} \tag{3.17}$$

$$R_{chem} = \frac{\left\langle \tilde{\mu}_{\mathrm{V_O^{\bullet\bullet}}} \right\rangle_{\Gamma_5} - \left\langle \tilde{\mu}_{\mathrm{Ce_{ce}^{\prime}}} \right\rangle_{\Gamma_5}}{I^{CP}_{\mathrm{V_O^{\bullet\bullet}}}} \tag{3.18}$$

here $\left\langle \tilde{\mu}_{\mathrm{V_O^{\bullet\bullet}}} \right\rangle$ and $\left\langle \tilde{\mu}_{\mathrm{Ce_{ce}^{\prime}}} \right\rangle$ are the average electrochemical potentials of oxide-ions vacancies and electrons at the respective boundaries. $I^{CP}_{\mathrm{V_O^{\bullet\bullet}}}$ is the cross-plane ionic current and $I^{IP}_{\mathrm{Ce_{ce}^{\prime}}}$ is the in-plane electronic current such that $I^{CP}_{\mathrm{V_O^{\bullet\bullet}}} = -I^{IP}_{\mathrm{Ce_{ce}^{\prime}}} = z_{\mathrm{V_O^{\bullet\bullet}}} F \left(\int J_{\mathrm{V_O^{\bullet\bullet}}} dx \right)_{\Gamma_5} = z_{\mathrm{V_O^{\bullet\bullet}}} F \left(\int J_{\mathrm{V_O^{\bullet\bullet}}} dx \right)_{\Gamma_1}$.

Parameter	Value
Current collector width (W1, [μm])	25
Ceria exposed width (W2, [μm])	125
Temperature [^{o}C]	750–850
H_2 sticking coefficient	$4.1x10^{-3}$
H_2O sticking coefficient	1
Pre-exponent of Reaction (3.3) rate constant [1/s] [32]	$5x10^9$
Activation energy of Reaction (3.3) [kJ/mol] [73]	131
E_{act} of H_2 adsorption [kJ/mol]	106.2
E_{act} of H_2O adsorption [kJ/mol]	0
$V_O^{\bullet\bullet}$ diffusion coefficient [m^2/s]	$1.96x10^{-10}$
$Ce_{ce}^{'}$ diffusion coefficient [m^2/s]	$6.46x10^{-9}$
Ceria surface site density [mol/cm^2]	$1.61x10^{-9}$

Table 3.1 A summary of the simulation parameters

Species	Enthalpy (kJ/mol)	Entropy (J/mol.K)
H_2	32.37	175.2
O_2	27.03	247.6
H_2O	-210.48	247.02
O_O^x	-259.8	68.14
$OH_O^{\bullet}$	-328.5	69.2
$H_2O_O^{\bullet\bullet}$	-272	130.5
$V_O^{\bullet\bullet}$	0	0

Table 3.2 Thermodynamic properties for gas-phase and surface species at 830 ^{o}C

For model validation, we conducted electrochemical impedance spectroscopy (EIS) experiments with ceria pattern electrode cells. 1 μm thick ceria patterns (surface area = 0.7414 cm^2) were deposited on a YSZ substrate (25 mm diameter and 250 μm thick) using DC magnetron sputtering (AJA International, ATC 2600 UHV). Details of the sputtering process are reported previously [41]. Figure 3.2 illustrates schematic of the pattern anode and the test assembly. For current collection, a square gold mesh (1024 mesh/cm^2) was used. EIS measurements were conducted using the Gamry Potentiostat (R600).

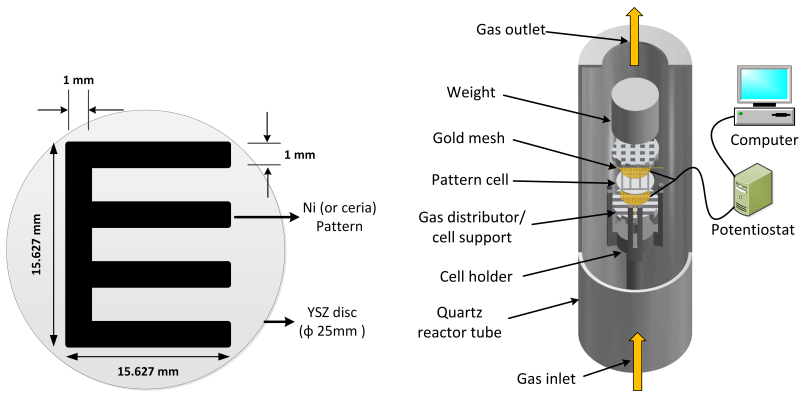

(a) Schematic of ceria pattern electrode

(b) Test assembly

Figure 3.2 Experimental setup

3.4 Results and Discussions

Fig. 3.3 and Fig. 3.4 show migration pathways of electrons and vacancies, respectively. Thick blue lines represent the electrochemical potential and thin black lines represent the charge flux. Electrons produced at gas/ceria interface are collected by metal collector and none of them passes through ceria/YSZ interface because of electron blocking nature of YSZ electrolyte. Similarly, vacancies produced at gas/ceria interface converge at ceria/YSZ interface and none of them pass through metal/ceria interface because of ion blocking nature of metal collector.

The resistances associated with the reaction kinetics and the transport of vacancies and electrons in ceria are computed from the corresponding electrochemical potential and current, as given by Eqs.

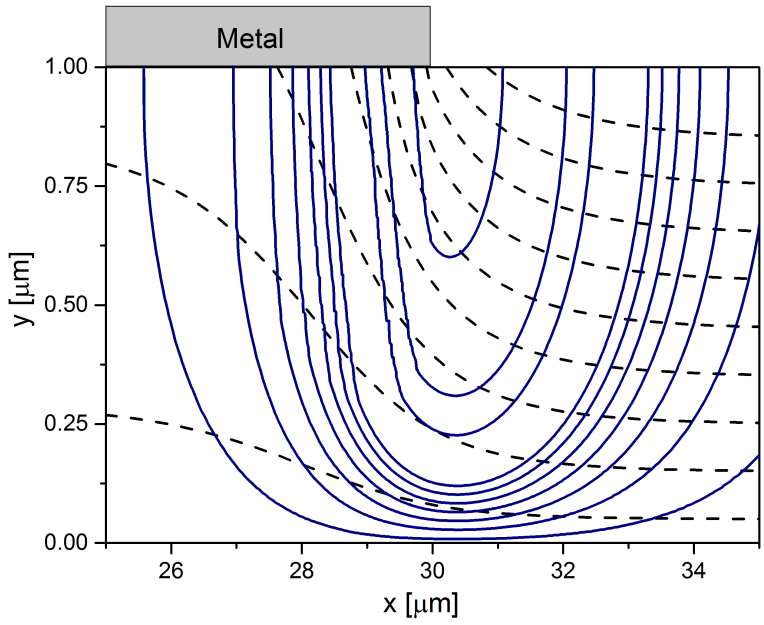

Figure 3.3 Electronic equi-potential lines (thick blue) and current flux lines (thin black) as computed at 830 [°C].

3.16–3.18. The individual contribution of each resistive step to the total electrode resistance is given in Table 3.3. In line with the previous studies [67, 66], the resistance caused by ionic and electronic transport is significantly smaller than the resistance caused by the electrochemical reactions. This implies that the defect transport is fast enough to be unlikely to control the cell response at these conditions. Therefore, the rate-determining step is largely related to the reaction kinetics.

To further analyze, the EIS experiments were conducted in a wide

Parameter	Resistance (Ωcm^2)
Surface reaction resistance (R_{rxn})	72.8
In-plane drift-diffusion resistance (R^{IP}_{eon})	4.8
Cross-plane bulk ionic resistance (R^{CP}_{ion})	1.3

Table 3.3 Resistance of individual resistive steps computed from the NPP model

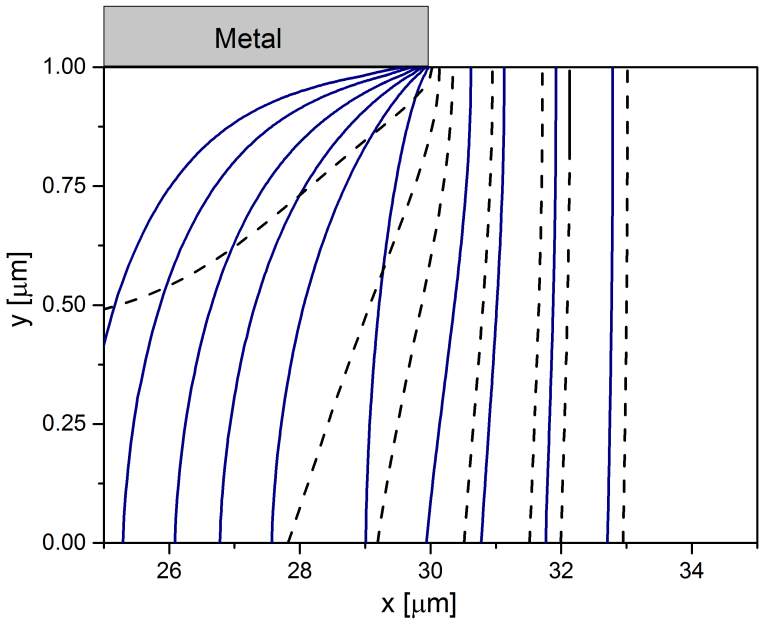

Figure 3.4 Ionic equi-potential lines (thick blue) and current flux lines (thin black) as computed at 830 [°C]

range of temperature and gas-phase composition. A representative impedance spectrum at 830°C, $x\mathrm{H}_2 = 0.96$, and $x\mathrm{H}_2\mathrm{O} = 0.04$ is shown in Fig. 3.5. To quantify various resistive and capacitive contributions in the overall cell response, the impedance spectra were deconvoluted using an equivalent circuit as shown in the inset of Fig. 3.5. This circuit is adopted from Baumann et al. [76] that was originally developed for the thin-film LSCF cathodes. Here, an $R_{hf} - Q_{hf}$ element is added in series to the original circuit to model the observed high-frequency arc and L_{lead} to account for the lead inductance. Decaluwe et al. [77] have also used a similar circuit to model the impedance response of thin-film ceria pattern anodes. The Nyquist and Bode representations – the experimental spectrum with symbols and final circuit fits with red lines – are shown in Fig. 3.5a and Fig. 3.5b, respectively. The circuit fitting fairly overlaps the experimental spectrum except at very low frequencies where some distorted points were observed. The resistances R_{chem}, R_{int}, R_{hf}, and Re are found to be 76.7, 2.2, 1.3, and 2.1 ($\Omega\mathrm{cm}^2$), respectively. R_{chem} is related to the electrochemical reaction at the gas/ceria interface. Hereafter, the polarization resistance term is used to refer to R_{chem}.

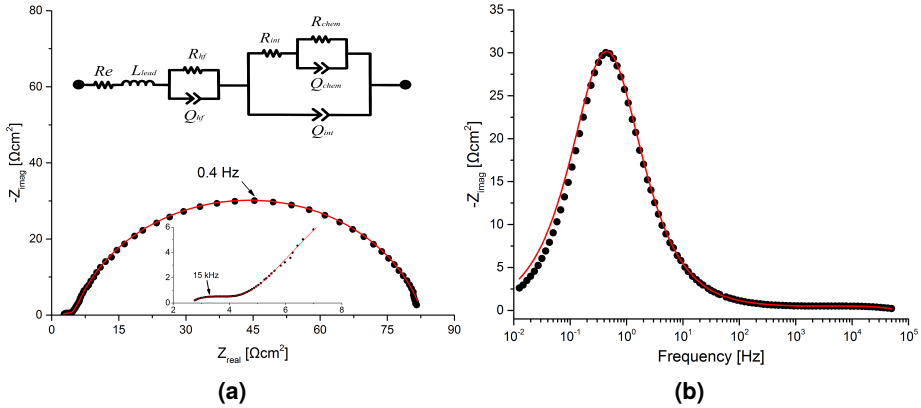

Figure 3.5 The impedance spectrum and the equivalent circuit model fit at 830 [°C]. The equivalent circuit model itself is shown in (a) inset. Symbols represent the experimental data points and red lines show the corresponding fitting.

The capacitance (C_{chem}, C_{int}, and C_{hf}) corresponding to three $R-Q$ elements, as calculated by $C_i = (R_i^{1-n}Q_i)^{1/n}$, are 4.6x10^{-3}, 4.1x10^{-4}, and 5.2x10^{-6} (F/cm^2), respectively.

Fig. 3.6 shows the experimental and simulated effect of temperature on the polarization resistance (R_{ct}). Similarly, Fig. 3.7 shows the effect of the hydrogen fraction. The experimental value of hydrogen reaction order is found to be 0.15. It can be seen that the proposed reaction scheme predicts the polarization resistance sufficiently over a wide range of temperature and gas-phase composition. The simulated activation energy is found to be 107.7 kJ/mol that matches well with the experimental value (101.7 kJ/mol).

Simulated fractional coverage of the oxide site species (O_O^x, $OH_O^{\bullet}$ and $V_O^{\bullet\bullet}$) as a function of temperature are shown in Fig. 3.8. The surface coverage of $H_2O_O^{\bullet\bullet}$ was very low (of the order of 10^{-4}), therefore, not shown here. Very low coverage is attributed to the relatively fast H_2O desorption kinetics. As shown in Fig. 3.8, the coverage of $OH_O^{\bullet}$ decreases with increase in temperature, whereas the coverage of O_O^x increase with increase in temperature. It was well expected because, 1) the hydrogen adsorption so the hydroxyl formation decreases with increase

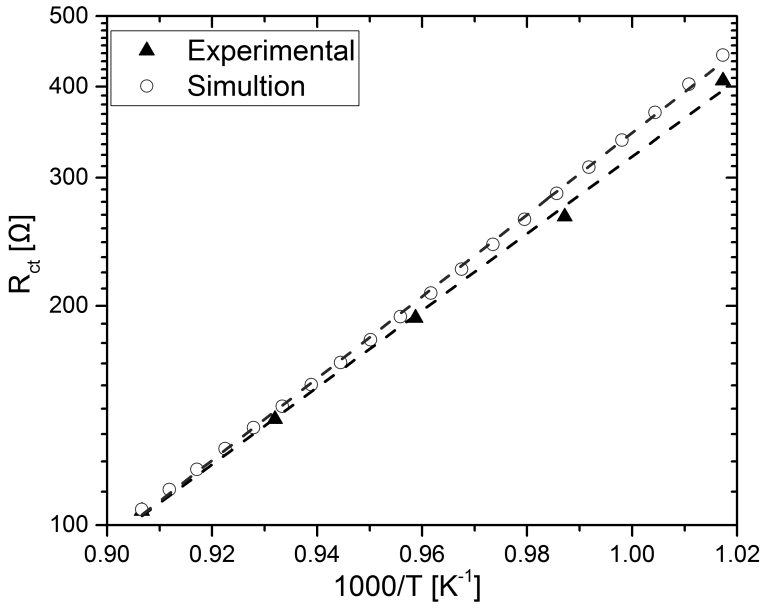

Figure 3.6 Experimental and simulated Arrhenius plot for H_2/H_2O gas mixture. Lines are guides to the eye.

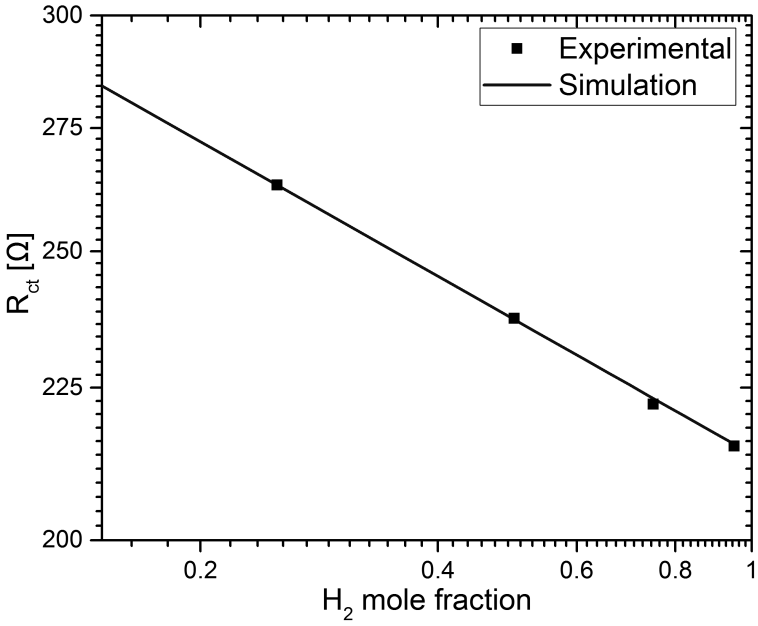

Figure 3.7 Experimental and simulated resistance as a function of hydrogen mole fraction at 4% H_2O and 760 [^oC].

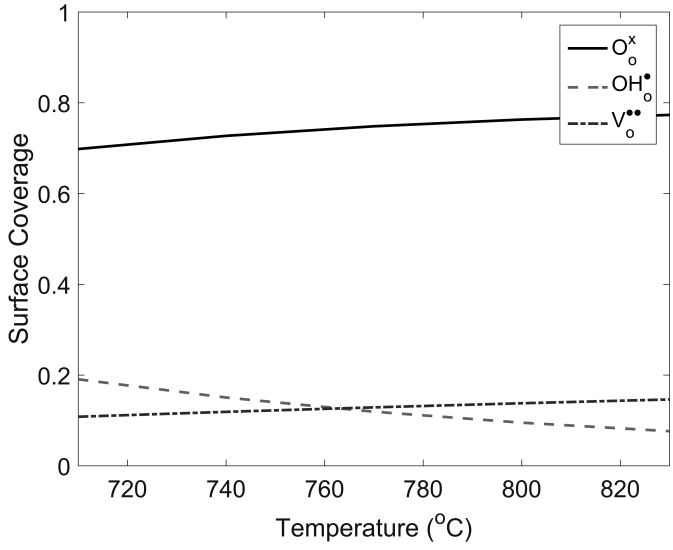

Figure 3.8 Computed fractional coverage of oxide site species as a function of temperature for H_2-4%H_2O gas mixture

in temperature, and 2) high temperature favors the O-H bond scission that liberates the lattice oxide sites covered by the hydroxyl groups. A similar trend is also reported elsewhere [74]. The surface coverage of O_O^x and $OH_O^\bullet$ at 700 °C is found to be 0.70 and 0.19, respectively (Fig. 3.8). When compared with the literature, Zhang et al. [38] found a coverage of O_O^x and $OH_O^\bullet$ as 0.75 and 0.25, respectively, with XPS at the same temperature, which are in reasonable agreement with the values found in this work.

3.4.1 Rate-determining step

Since the resistance caused by the bulk transport is insignificant compared to the resistance caused by the reaction kinetics, rate limitations are globally attributed to the surface kinetics that is in line with the previous studies [66, 67, 78]. The kinetics of elementary steps in the proposed reaction scheme allow us to identify the rate-determining elementary step, which is performed by a sensitivity analysis. The forward rate coefficients of elementary reactions are varied 10% and the resultant polarization resistance is compared with the previous value.

The relative sensitivity is defined as:

$$\frac{\Delta R_{chem}/R_{chem}}{\Delta k_m/k_m} \tag{3.19}$$

The relative sensitivity of elementary steps is shown in Fig. 3.9. It can be clearly seen that the oxidation process is only sensitive to the charge-transfer reaction (reaction 3.2). This implies that the rate of overall oxidation reaction is determined by the kinetics of reaction 3.2. Whereas, the formation and desorption of water can then be considered as the equilibrium reactions, proceeding at the same rate as the charge-transfer reaction. In the current reaction scheme, a charge-transfer from surface hydroxyl ions to the neighboring cerium cations is assumed which leads to a net positive charge on the hydroxyl ions ($OH_O^{\bullet}$) and a net negative charge on the cerium ($Ce_{ce}^{'}$). The existence of $OH_O^{\bullet}$ has also been witnessed by Feng et al. [69] through an X-ray photoelectron spectroscopy (XPS) measurements. Feng observed that the oxide-vacancy-free (fully oxidized) ceria surface in H_2/H_2O atmosphere remains mostly in the reduced state, especially under cathodic polarization, leading to the conclusion that the surface hydroxyl groups are effectively positively charged species as they transfer electrons to neighboring cerium ions.

Table 3.4 summarizes the charge-transfer process and the rate-determining steps reported in the literature. Although majority of these studies also reported the charge-transfer as the rate-determining, difference in the understanding of the charge-transfer process is apparent. In our previous study [37], despite of the fact that the two-step charge-transfer mechanism was assumed, the rate-determining step was found to be the transfer of electron from hydroxyl to the cerium atoms. A similar conclusion is made in [74]. In addition to the same conclusion on the rate-determining step, Zhenlong et al. [74] also opted for a single elementary step for hydrogen adsorption and the charge-transfer process which is in line with this study. Zhenlong further found that the relative difference of the defect concentration between ceria surface and bulk (up to 100 nm depth) is less than 0.001 % at 1000 °C. Similarly, Feng et al. [69] also reported a negligible bulk diffusional polarization. Both of these studies also suggest that the bulk diffusion is unlikely

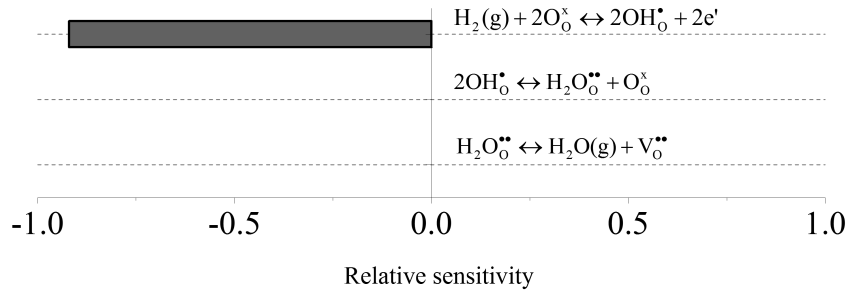

Figure 3.9 Sensitivity analysis of charge-transfer resistance for elementary reaction at 830 [°C]

Rate-determining elementary step	Reference
$H_2(g) \rightleftharpoons H_{ads} + H_{ads}$	[68]
$H_{ads} + O_O^x \rightleftharpoons OH_O^\bullet + e'$	[37]
$H_{ads} + OH_O^\bullet \rightleftharpoons H_2O(g) + V_O^{\bullet\bullet} + e'$	[38]
$OH_O^x \rightleftharpoons OH_O^\bullet + e'$	[69]
$H_2(g) + 2O_O^x + 2Ce_{ce}^x \rightleftharpoons 2OH_O^\bullet + 2Ce_{ce}^{'}$	[74]
$O_O^x(YSZ) + Ce_2O_3(b) \rightleftharpoons V_O^{\bullet\bullet}(YSZ) + Ce_2O_4(b) + 2e'$	[32]

Table 3.4 Rate-determining elementary steps reported in the literature

to be the rate-determining at SOFC operating conditions. Since, the charge-transfer is found to be the slowest elementary step, lowering the barrier of charge-transfer between $OH_O^\bullet$ and $Ce_{ce}^{'}$ should improve the electrocatalytic activity of ceria.

3.4.2 Exchange-current density (i_o)

Since the charge-transfer reaction (reaction 3.2) is found to be the rate-determining step, a theoretical relationship for the exchange-current density can be derived assuming that all other elementary reactions are in equilibrium. For convenience, the charge-transfer reaction is written as:

$$H_2(g) + 2O_O^x \rightleftharpoons 2OH_O^\bullet + 2e' \tag{3.2}$$

Net current density is proportional to the charge-transfer reaction rate and can be written as:

$$\begin{aligned} i &= \left|\overrightarrow{i}\right| - \left|\overleftarrow{i}\right| \\ &= 2F\left[\overrightarrow{k_1} exp\left(\frac{2F\beta_a E_{an}}{RT}\right)\left[\mathrm{O}_{\mathrm{O}}^{\mathrm{x}}\right]^2\right] - 2F\left[\overleftarrow{k_1} exp\left(-\frac{2F\beta_c E_{an}}{RT}\right)\left[\mathrm{OH}_{\mathrm{O}}^{\bullet}\right]^2\right] \end{aligned}$$

Here, hydrogen concentration is explicitly included in $\overrightarrow{k_1}$ for dimensional consistency: both $\overrightarrow{k_1}$ and $\overleftarrow{k_1}$ have the dimensions of [mol/cm^2.s]. The potential term (E_{an}) can be separated into the equilibrium potential (E^{eq}) and the overvoltage (η), so that we finally get a Buttler-Volmer relation of the form:

$$i = |i_o|\left[exp\left(\frac{2F\beta_a\eta}{RT}\right) - exp\left(-\frac{2F\beta_c\eta}{RT}\right)\right] \tag{3.20}$$

By definition $|i_o| \equiv \left|\overrightarrow{i_o}\right| = \left|\overleftarrow{i_o}\right|$, where:

$$\left|\overrightarrow{i_o}\right| = 2F\left[\overrightarrow{k_1} exp\left(\frac{2F\beta_a E^{eq}}{RT}\right)\left[\mathrm{O}_{\mathrm{O}}^{\mathrm{x}}\right]^2\right] \tag{3.21}$$

and

$$\left|\overleftarrow{i_o}\right| = 2F\left[\overleftarrow{k_1} exp\left(-\frac{2F\beta_c E^{eq}}{RT}\right)\left[\mathrm{OH}_{\mathrm{O}}^{\bullet}\right]^2\right] \tag{3.22}$$

The equilibrium coverage of $\mathrm{O}_{\mathrm{O}}^{\mathrm{x}}$ and $\mathrm{OH}_{\mathrm{O}}^{\bullet}$ can either be obtained by directly solving the rate equation (Eq. 3.7) or can be extracted from Fig. 3.8. Alternatively, a potential independent expression can be derived as [79]:

$$|i_o| = \left|\overrightarrow{i_o}\right|^{\beta_c}\left|\overleftarrow{i_o}\right|^{\beta_a} \tag{3.23}$$

On simplification we get:

$$i_o = 2F\left(\overrightarrow{k_1}\left[\mathrm{O_O^x}\right]^2\right)^{\beta_c}.\left(\overleftarrow{k_1}\left[\mathrm{OH_O^{\bullet}}\right]^2\right)^{\beta_a} \tag{3.24}$$

For a typical value of $\beta_a = \beta_c = 0.5$, Eq. (3.24) further simplifies as:

$$i_o = 2F\left(\sqrt{\overrightarrow{k_1}\overleftarrow{k_1}}\left[\mathrm{O_O^x}\right]\left[\mathrm{OH_O^{\bullet}}\right]\right) \tag{3.25}$$

The potential terms in the expression (3.24) disappears because:

$$exp\left(2\beta_a\beta_c FE^{eq}/RT\right)exp\left(-2\beta_a\beta_c FE^{eq}/RT\right) = 1 \tag{3.26}$$

A further treatment of $\left[\mathrm{O_O^x}\right]$ and $\left[\mathrm{OH_O^{\bullet}}\right]$ as a function of $p_{\mathrm{H_2}}$ and $p_{\mathrm{H_2O}}$ will reveal the theoretical reaction orders of $\mathrm{H_2}$ and $\mathrm{H_2O}$. The experimental exchange-current density can be related to the polarization resistance [80]:

$$i_o = \frac{RT}{zFA_{an}R_{chem}} \tag{3.27}$$

where A_{an} indicates the anode active area. R_{chem} can be obtained by electrochemical impedance spectroscopy. Figure 3.10 and 3.11 show the experimental and simulated exchange-current densities as a function of temperature and hydrogen mole fraction, respectively. It can be seen that the simulated exchange-current density reasonably matches the experimental one.

These results can be of a significant importance, as the exchange-current density is the key parameter in fuel cells modeling. While, it is common to use semi-empirical relations in SOFC modeling to address the electrochemistry, model derived here (Eq. 3.25) can provide a reliable approximation over a wide range of operating conditions. It is also computationally inexpensive to incorporate this model in a CFD code to obtain the activation overpotential.

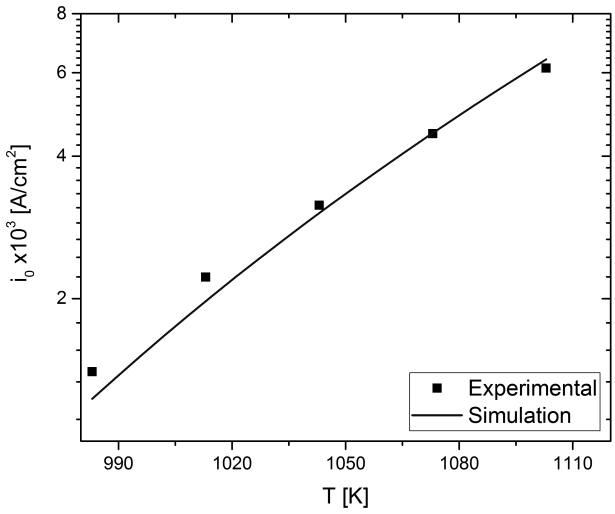

Figure 3.10 Exchange-current density as a function of temperature for H_2/4%H_2O gas mixture

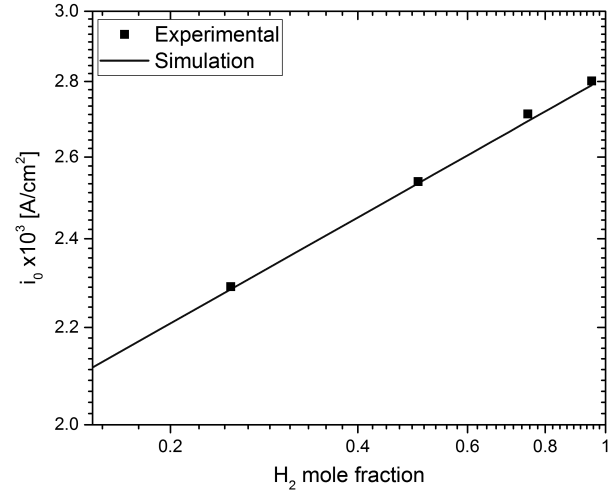

Figure 3.11 Exchange-current density as a function of hydrogen partial pressure at 760 [^{o}C]

3.5 Conclusions

This study presented detailed mechanistic investigation of hydrogen electrochemical oxidation on ceria anode. A reaction scheme was proposed and the NPP model was developed to simulate the resistance associated with the electrochemical reactions and defect transport. Kinetic parameters of forward and backward reactions were coupled considering thermodynamic consistency and microscopic reversibility of the elementary reactions. The effect of operating conditions such as temperature and hydrogen mole fraction were studied in detail.

The simulation has shown that the bulk transport of oxide-ions vacancies and electrons is faster compared to the surface chemistry. Further, a sensitivity analysis has shown that the charge-transfer reaction is the slowest and rate-determining elementary step. Based on this rate-determining step, a quantitative relationship for calculating the exchange-current density is developed and validated with the experimental data. This model can be used to obtain the activation overpotential incorporating the local operating conditions such as temperature and species concentration. Further, this model can easily be implemented in a CFD code where local conditions are well defined thus avoiding the need of empirically estimating the exchange-current density.

4

An SOFC anode model using TPB-based kinetics

There are three approaches used in SOFC modeling studies to incorporate the kinetics of electrochemical oxidation process: (1) Butler-Volmer equation using global oxidation kinetics, (2) mass-action kinetic approach with a detailed oxidation mechanism, and (2) Butler–Volmer formalism based on the kinetics of a predefined rate-limiting step of a multistep mechanism. The first approach is easy to implement in cell and system level models, however, does not incorporate mechanistic details of the oxidation process. In the mass-action kinetics approach, coupled rate equations are solved for concentration of reaction species and total current is calculated from the kinetics of charge-transfer reaction(s). Such an approach is comprehensive and does not require a priori assumptions about the rate-limiting step. However, the computational time is higher than required for solving Butler-Volmer equation because of the involvement of coupled differential equations. This approach is applied in chapter 2 for kinetic modeling of syngas oxidation. Butler–Volmer formalism is analytically developed considering a predefined rate-limiting step in the mechanisms. Elementary steps other than the rate-limiting are considered as pseudo-equilibrium reactions. In the present work, Butler-Volmer formalism is used to derive the TPB-based kinetics from experimental data of nickel pattern electrode cells and then the kinetics is used in Ni/YSZ cermet electrode cell model for the estimation of effective TPB density and activation overpotential.

4.1 Introduction

A cermet of nickel and yttrium-stabilized zirconia (YSZ) is currently the state-of-the-art anode material in the solid oxide fuel cells (SOFCs). It is commonly accepted that the electrochemical reactions in a Ni/YSZ cermet electrode occur in the vicinity of nickel/YSZ/gas triple-phase boundary (TPB). Generally, the higher the TPB length, the better is the electrode performance [5, 81]. Therefore, a quantitative knowledge of the TPB length is required to study the electrochemical reactions and their kinetics. Though the cermet electrodes ensure a high volumetric TPB length, the quantification of TPB is difficult because of the complex 3D porous structure of the cermet. Moreover, what fraction of the total volumetric TPB length actually participates in the reactions is also not clear. This makes the cermet electrodes non-ideal for such kinetics studies. Pattern electrodes, on the other hand, are best suited for this purpose because of their simplified geometry and easily quantifiable TPB length. In addition, the 2D design of the patterns also eliminates the structural and even the gas-phase effects, which exist in the cermet electrodes especially in the anode supported cells.

Mizusaki et al. [6, 48] first introduced the concept of SOFC pattern electrodes, followed by others [3, 5, 81–84], to study the hydrogen electrochemical oxidation mechanisms at the TPB. Table 4.1 gives a brief overview of these studies including the operating conditions and the parametric dependence of the polarization resistance. As can be seen, the reported dependence on $p_{\mathrm{H_2}}$, $p_{\mathrm{H_2O}}$, T, and l_{tpb} varies between these studies, largely because of the TPB inactivation due to impurities and the morphological changes during the course of experiments [42, 85]. In general, these studies report a highly thermally activated rate-limiting process, a weak dependence on the hydrogen partial pressure, and a strong dependence on the water partial pressure.

In several studies [42, 89–92], elementary kinetic approach is used to model the pattern electrodes in order to understand the charge-transfer mechanisms and to identify the rate-limiting processes. The charge-transfer is among the least understood aspect of the SOFC electrode electrochemistry. Three mechanisms are commonly reported for hydrogen electrochemical oxidation which include: 1) surface hydrogen spillover at

Para.	Mizusaki [48]	de Boer [82]	Bieberle [86]	Utz [87]	Yao [88]	Sukeshini [16]	Patel [3]
$l_{tpb}\left[\frac{\mathrm{m}}{\mathrm{cm}^2}\right]$	0–5.56	1.4–9.7	0.04–12.85	1.0–8.0	1.16–5.19	1.75–16.69	0.203
T [°C]	700–850	850	400–700	450–800	500–800	750–850	700–850
p_{H_2}[kPa]	0.25–19	4.95–99.8	2.0–88	0.8–90.0	5.0–90.0	8.3–33.3	97.0
p_{H_2O}[kPa]	0.25–1.7	0.6–3.08	3.0–70.0	0.02–60.0	5.0–70.0	0.0–4.0	4.0
E_a[eV]	0.75	1.60	0.88	1.01–1.37	0.73–1.17	0.95–1.15	1.31
a	-0.09–0.15	-0.26	0.11	-0.15–0.14	0.09–0.14	–	–
b	0.32–0.88	0.37	0.67	0.68	0.3	–	–
m	0.5	0.67	0.67–1.3	1.19	0.7–0.72	~0.5	–
α_a	1.8 [89]	1.5–2.5	–	1.22–1.38	0.8	0.24–0.30	–
α_c	0.74 [89]	1.5–0.5	–	–	0.6	0.1	–

Table 4.1 A summary of pattern electrode experimental studies reported in the literature . a, b, and m indicate the dependence of polarization resistance on p_{H_2}, p_{H_2O}, and l_{tpb}, respectively, using the expression: $R_p = c\left(l_{tpb}\right)^{-m}\left(p_{H_2}\right)^{-a}\left(p_{H_2O}\right)^{-b}$.

the TPB [82, 93], 2) surface oxygen spillover at the TPB [48, 91], and 3) bulk transfer of interstitial hydrogen species at the electrode/electrolyte two-phase boundary [94, 95]. Hanna et al. [4] have comprehensively reviewed these mechanisms. The hydrogen spillover from nickel to YSZ surface is considered as the dominant mechanism, as it yields a better qualitative agreement with the experimental results compared to other mechanisms [42, 89]. Besides charge-transfer reactions, the electrochemical oxidation also involves the adsorption/desorption of the gas-phase species and incorporation of the oxide ions between the surface and the bulk of electrolyte. Assuming hydrogen spillover as the dominant mechanism, Zhu et al. [96] proposed following five step simplified hydrogen electrochemical oxidation pathway (reaction 4.1–4.5).

$$\mathrm{H_{2gas}} + 2\square_{\mathrm{Ni}} \rightleftharpoons 2\mathrm{H_{Ni}} \tag{4.1}$$

$$\mathrm{H_{Ni}} + \mathrm{O^{2-}_{YSZ}} \rightleftharpoons \mathrm{OH^{-}_{YSZ}} + \square_{\mathrm{Ni}} + \mathrm{e^{-}_{Ni}} \tag{4.2}$$

$$\mathrm{H_{Ni}} + \mathrm{OH^{-}_{YSZ}} \rightleftharpoons \mathrm{H_2O_{YSZ}} + \square_{\mathrm{Ni}} + \mathrm{e^{-}_{Ni}} \tag{4.3}$$

$$\mathrm{H_2O_{YSZ}} \rightleftharpoons \mathrm{H_2O_{gas}} + \square_{\mathrm{YSZ}} \tag{4.4}$$

$$\mathrm{O^{x}_{O}} + \square_{\mathrm{YSZ}} \rightleftharpoons \mathrm{O^{2-}_{YSZ}} + \mathrm{V^{\bullet\bullet}_{O}} \tag{4.5}$$

The overall oxidation process is predominantly controlled by one of these elementary reactions. Though there are different proposals on the rate-limiting step, the charge-transfer process bears a general consensus [42, 89, 90]. Anode models that incorporate the detailed oxidation mechanism, applies a mass action kinetic approach without any a priori assumption about the rate-limiting step [42, 89]. This approach is advantageous when multiple elementary reactions or charge-transfer mechanisms limit the oxidation process. This approach, however, is not common in the cell and stack level models where the Butler-Volmer relationship or its approximations are generally applied in combination

with empirically obtained exchange-current density. Zhu et al. [96], on the other hand, started with a detailed reaction mechanism and derived a more practical Butler-Volmer formalism (Eq. 4.6).

$$i_{an} = i^0 \left(exp\left(\frac{\left(1+\beta_{3a}\right) F \eta_{act,an}}{RT} \right) - exp\left(-\frac{\beta_{3c} F \eta_{act,an}}{RT} \right) \right) \tag{4.6}$$

where $\eta_{act,an} = E_{an} - E_{eq}$ is the anodic activation overpotential. E_{an} is the difference between the electronic potential ($\phi_{el,an}$) and the ionic potential ($\phi_{ion,an}$) in the anode. E_{eq} is the corresponding potential at equilibrium. $1+\beta_{3a}$ and β_{3c} are the apparent symmetry factors (transfer coefficients)for forward and backward rates of the reaction (4.3), respectively. The derivation of Eq. 4.6 assumes that the mass transport effects are negligible and the rate limitations are solely attributed to the charge transfer reaction (4.3). This assumption is widely accepted in the SOFC community, though hydrogen adsorption at high currents is also found as rate limiting in a recent study [97].

The exchange-current density (i^0) in the above expression (Eq. 4.6) is defined as:

$$i^0 = i^*_{\mathrm{H_2}} \frac{\left(K_1 p_{\mathrm{H_2}}\right)^{\beta_{3c}/2} \left(p_{\mathrm{H_2O}}\right)^{1-\beta_{3c}/2}}{1+\left(K_1 p_{\mathrm{H_2}}\right)^{1/2}} \tag{4.7}$$

where $i^*_{\mathrm{H_2}}$ is an electrochemical parameter [A/m^2.atm$^{1-\beta_{3c}/2}$] given by:

$$i^*_{\mathrm{H_2}} = 2 l_{TPB} F k_{3r} (K_2 K_3)^{\beta_{3c}/2} \left(\frac{K_5}{K_4}\right)^{1-\beta_{3c}/2} \tag{4.8}$$

Eq. 4.7 and Eq. 4.8 provide an explicit relationship between i_0 and all four variable parameters: $p_{\mathrm{H_2}}$, $p_{\mathrm{H_2O}}$, l_{tpb}, and temperature dependent reaction rate coefficient. The degree of the dependence on each of these variables can be obtained from the pattern electrode cell experiments. The reaction orders of $p_{\mathrm{H_2}}$ and $p_{\mathrm{H_2O}}$ obtained by the pattern electrode cell experiments are summarized in the Table 4.1.

The explicit dependence of i^0 on l_{tpb} is of particular interest, because it enables developing the TPB-based kinetics and implementing it in a computational fluid dynamic (CFD) model for optimizing the electrode performance. Moreover, it can also help predicting the cell performance degradation related to the morphological changes or contamination.

Known studies employing Eq. 4.7 to calculate the exchange-current density, usually treat $i^*_{\mathrm{H_2}}$ as a fitting parameter – largely because of the lack of a quantitative knowledge of the rate constant and the TPB length. In a pattern electrode cell experiment, since the TPB length is known, magnitude of the rate constant can be determined with confidence and can be applied in the cermet electrode cell models leaving behind the active TPB length as a fitting parameter. This approach will provide a better understanding of the active TPB length of the cermet electrode and help optimizing the electrode structure. In this work, TPB-based kinetics is first developed from pattern electrode cell experimental data reported in the literature, the same kinetics is then validated with a different set of pattern electrode cell experiments performed in our group, and finally the kinetics is extended to Ni/YSZ cermet electrode cell for the estimation of effective TPB density.

4.2 Model formulation

When a finite current is drawn from the fuel cell, the open-circuit voltage (OCV) is reduced by various losses including: the ohmic type losses associated with the ionic and electronic transport, the activation overpotentials associated with the limited kinetics of the electrocatalysis, and the concentration overpotential associated with the gas-phase transport. The operating cell voltage can therefore be represented in terms of these potential losses:

$$E_{cell} = E_{Nernst} - \eta_{ohm} - \eta_{act,an} - \left|\eta_{act,ca}\right| - \eta_{conc,an} - \eta_{conc,ca} \qquad (4.9)$$

where η_{ohm} is the ohmic overpotential, $\eta_{act,an}$ and $\eta_{act,ca}$ are the activation overpotentials at the anode and the cathode, and $\eta_{conc,an}$ and $\eta_{conc,ca}$ are the corresponding concentration overpotentials. $\eta_{act,an}$ and

$\eta_{act,ca}$ are defined as:

$$\eta_{act,an} = \phi_{el,an} - \phi_{ion,an} - E_{eq} \tag{4.10}$$

$$\eta_{act,ca} = \phi_{el,ca} - \phi_{ion,ca} - E_{eq} \tag{4.11}$$

$\phi_{el,i}$ and $\phi_{ion,i}$ are the potentials of electronic and ionic phases, respectively. The relationship between η_{act} and the current density is described by Butler-Volmer equation.

$$i = i^0 \left(exp\left(\frac{\alpha_a F \eta_{act}}{RT}\right) - exp\left(-\frac{\alpha_c F \eta_{act}}{RT}\right)\right) \tag{4.12}$$

α_a and α_c are the transfer coefficients in the anodic and the cathodic directions of the electrochemical reaction. In the anode, α_a and α_c are given in Eq. 4.6. The definition of i^0 in the anode and in the cathode are adopted from [96]. The concentration overpotential is described as:

$$\eta_{conc,an} + \eta_{conc,ca} = \frac{RT}{2F} ln\left(\frac{p^{tpb}_{\mathrm{H_2O}} p_{\mathrm{H_2}}}{p_{\mathrm{H_2O}} p^{tpb}_{\mathrm{H_2}}}\right) + \frac{RT}{4F} ln\left(\frac{p_{\mathrm{O_2}}}{p^{tpb}_{\mathrm{O_2}}}\right) \tag{4.13}$$

The electric potential of electron conducting phase within the anode (ϕ_{an}), the electric potential of electron conducting phase within the cathode (ϕ_{ca}), and the electric potential of electrolyte phase (ϕ_{ion}) is governed by the charge-conservation equation. At steady-state the charge-conservation equations are described as: [98]

$$\nabla\left(\sigma^{e}_{ion}\nabla\phi_{ion}\right) = \begin{cases} Q_{an,el} & \text{within anode} \\ 0 & \text{within electrolyte} \\ Q_{ca,el} & \text{within cathode} \end{cases} \tag{4.14}$$
$$\nabla\left(\sigma^{e}_{an}\nabla\phi_{an}\right) = -Q_{an,el} \quad \text{within anode}$$
$$\nabla\left(\sigma^{e}_{ca}\nabla\phi_{ca}\right) = -Q_{ca,el} \quad \text{within cathode}$$

here σ^{e}_{i} is the effective conductivity [S/m] of phase i and $Q_{i,el}$ is the charge carrier source [A/m^3]. A positive value of the source term indicates the transfer of charge-carrier (here electrons) into the corresponding phase which tends to decrease the electric potential of that phase. The charge-conservation equation 4.14 is solved along with the mass conservation equation 4.15.

$$\frac{\partial c_k}{\partial t} + \nabla.J_k = \dot{s_k} \tag{4.15}$$

where c_k is the concentration of gas-phase specie k [mol/m^3], J_k is the molar flux [mol/m^2.s], and $\dot{s_k}$ is the net rate of production due to electrochemical reactions [mol/m^3.s]. The gas-phase transport in the cermet electrode is described here by the modified Stefan-Maxwell model to account for both binary and Knudsen diffusion [70].

This model is developed and solved with a finite element software COMSOL Multiphysics V5.1.

4.3 Deriving TPB-based kinetics from pattern anode studies

k_{3r} in Eq. 4.8 is the thermal rate coefficient of reaction (4.3) in the backward direction [96]. It can be written in the form of Arrhenius parameters of the forward rate coefficient and equilibrium constant as:

$$k_{3r} = k_3^0 exp\left(-\frac{E_{ct}^{act}}{RT}\right)/K_3 \tag{4.16}$$

here k_3^0, E_{ct}^{act}, and K_3 are the pre-exponent factor, activation energy, and equilibrium constant of the charge-transfer reaction, respectively. The activation energies obtained from various pattern electrode cell experimental studies are summarized in Table 4.1. k_3^0 can then be calculated by comparing i_{an}^0 from Eq. 4.7 with the experimental results of pattern electrode of known l_{tpb} and at given temperature and gas-phase activities. In pattern electrode, l_{tpb} is generally not the same as calculated based on the geometric definition of the patterns. Wavy edges of the patterns formed due to imperfect cell fabrication and cell degradation due to thermal and electrochemical processing can extend the length of TPB sites. Assuming that whole TPB length is electrochemically active, the cell performance may be better than expected based on the geometrical TPB length. Therefore, it is important to consider the effective (active) TPB length to derive the reaction kinetics. An imaging analysis can provide the information about the deviation of TPB length from the geometric value. The effective TPB fraction (ψ_{tpb}) is defined as:

$$\psi_{tpb} = \frac{\text{effective TPB length}}{\text{geometric TPB length}} \tag{4.17}$$

Using an imaging technique, Utz et al. [81] reported 1.3 times higher post-test l_{tpb} than the pre-test value (= 6.7 [m/cm^2]). Due to good stability of the patterns and known value of ψ_{tpb}, the same experimental results are used here to calculate the pre-exponent factor (k_3^0). Figure 4.1 shows the experimental Tafel plots (symbols) and the corresponding anodic and cathodic branches we simulated using Eq. 4.18 and Eq. 4.19, respectively. The slope and y-intercept of the simulated Tafel plots result in the best fit values of β_c = 0.7 and i_{an}^0 =1.9x10^{-3}, 9.2x10^{-4}, and 5.3x10^{-4} [A/cm^2] at 800, 750, and 700 [^{o}C], respectively. On comparing with Eq. 4.7, k_3^0 = 15 [mol/cm.s] is obtained at T = 800 [^{o}C], p_{H_2} = 8.3 [kPa], p_{H_2O} = 6.6 [kPa]. Considering that the reaction pathway and the rate-determining step remain the same, k_3^0 is independent of the

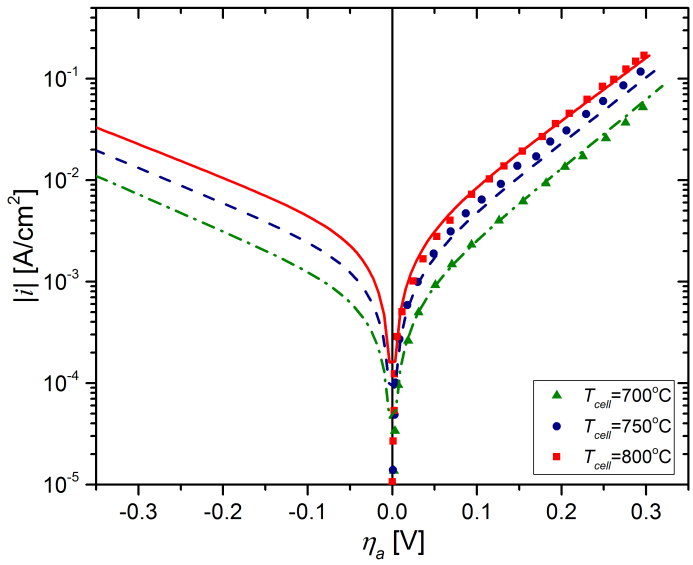

Figure 4.1 DC polarization data from Utz et al. [81] (symbols) together with anodic and cathodic Butler-Volmer fits (solid lines) at p_{H_2}= 8.3 [kPa], p_{H_2O}= 6.6 [kPa], and balance N_2).

gas-phase composition, therefore, can be used for any H_2/H_2O mixture. The effect of p_{H_2} and p_{H_2O} on the reaction kinetics is explicitly given by Eq. 4.7.

$$\overrightarrow{i} = i^0_{an} exp\left(\frac{(1+\beta_a)F\eta}{RT}\right) \tag{4.18}$$

$$\overleftarrow{i} = i^0_{an} exp\left(-\frac{\beta_c F\eta}{RT}\right) \tag{4.19}$$

4.4 Experimental

Two types of experimental studies are conducted in this work; (1) electrochemical impedance spectroscopy (EIS) using symmetrical nickel pattern electrode cells, and (2) polarization measurement using button cells with nickel pattern anode and platinum cermet cathode. Design of symmetrical cells and experimental setup for EIS measurements and

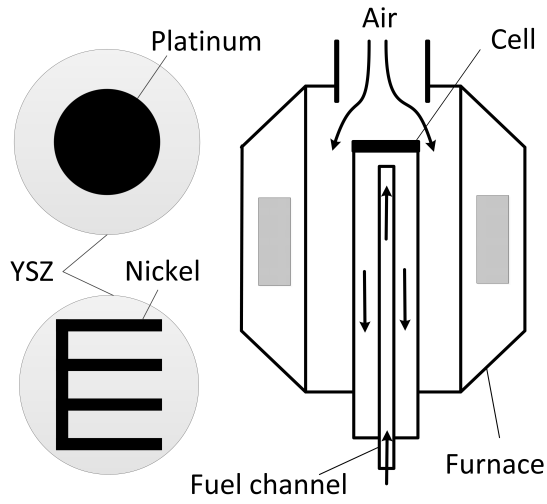

Figure 4.2 Nickel pattern anode, platinum porous cathode, and test assembly

corresponding results are reported previously [99]. The experimental setup for polarization measurements is shown in Figure 4.2. Geometric details of the anode, cathode, and electrolyte are given in Table 4.2. Preparation of the nickel pattern anode is also described previously [41]. Whereas, cermet cathode was prepared by brush painting platinum paste (www.fuelcellmaterials.com) on the YSZ electrolyte to obtain a high cathodic TPB length. The polarization curves were obtained using a Gamry Potentiostat (R600) on feeding 4% humidified hydrogen environment (100 ml/min) to the anode and ambient air to the cathode.

The model described in section 4.2 is solved for polarization study using COMSOL Multiphysics V5.1. The simulation flow diagram is shown in Figure 4.3 and summary of the simulation parameters is given in Table 4.2.

4.5 Polarization behavior of nickel pattern electrode cells

Before polarization study, the anodic exchange-current density is first calculated from the charge-transfer resistance (R_{ct}) obtained using EIS results reported previously [99]. R_{ct} at 800 [^{o}C], $p_{\mathrm{H_2}}$ = 97 [kPa],

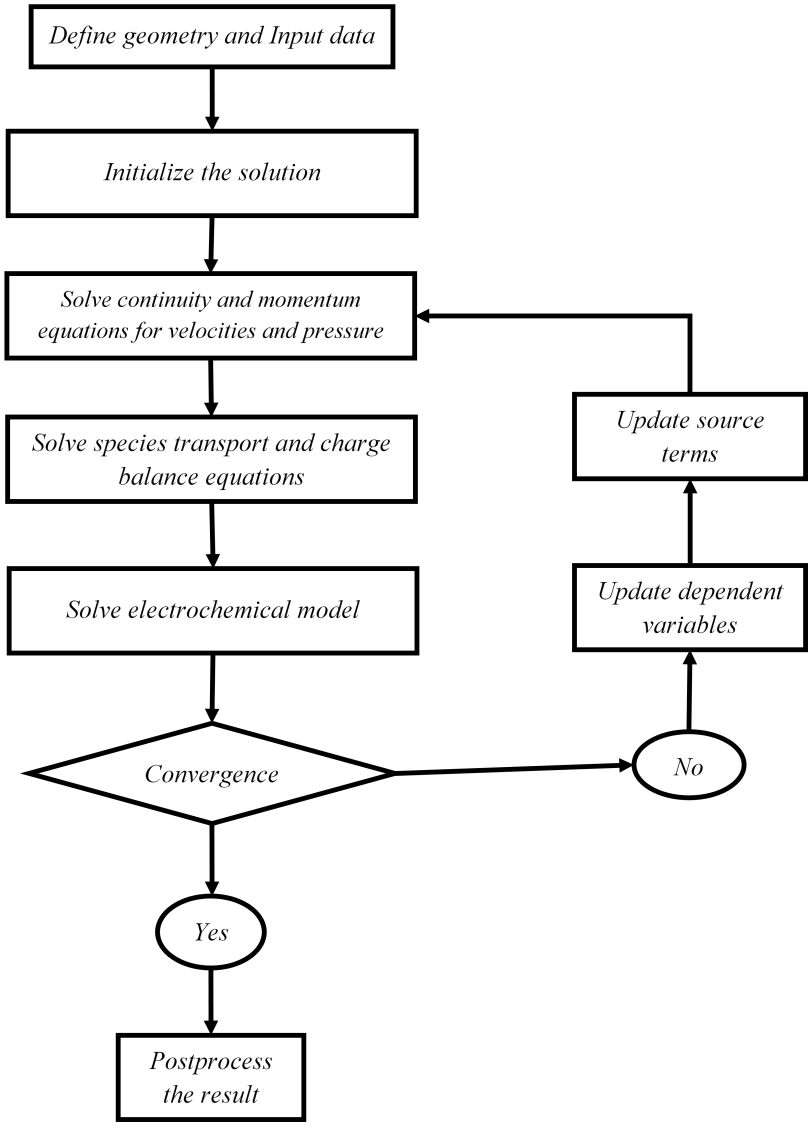

Figure 4.3 Simulation flow diagram

Parameter	Value
Anode	
Pattern surface area	0.741 [cm^2]
Pattern thickness	1.7 [μm]
Exchange-current density (i^0_{an})	1.83x10^{-4} [A/cm^2]
Inlet flow rate	100 [ml/min]
Symmetry factors (β_a, β_c)	0.3, 0.7
Cathode	
Thickness	100 [μm]
Diameter	16 [mm]
Exchange-current density (i^0_{ca})	5.0x10^{-2} [A/cm^2]
Electrolyte	
Thickness	0.5 [mm]
Diameter	25 [mm]
Conductivity	0.42 [S/m]
General parameters	
Operating temperature	800 [^{o}C]
Operating pressure	1 [atm]

Table 4.2 A summary of simulation parameters for nickel pattern electrode cell model

and p_{H_2O} = 4 [kPa] was found to be 252 [Ωcm^2] that corresponds to the exchange-current density ($i^0_{an} = RT/zFR_{ct}$) of 1.83x10^{-4} [A/cm^2]. Using Eq. 4.7 and Eq. 4.8, this i^0_{an} along with k^0_3 and E^{act}_{ct}, as derived in the previous section, results in the effective TPB length of 2.57 [m/cm^2] that is 12.7 times larger than the geometrically-defined TPB length (= 0.2027 [m/cm^2]). This can be anticipated as post-test SEM images of the patterns revealed several pits in the dense nickel layer, as shown in Figure 4.4a, exposing additional TPB length. The exposed TPBs, as shown in figure 4.4b, are analyzed using an open source image processing software, ImageJ [100]. The software counted 219 pits with average perimeter size of 21.25 [μm] on the pattern of total surface area 1.168x10^5 [μm^2]. This causes an additional TPB length of 3.44 [m cm^{-2}]. In addition, imperfect pattern fabrication and heat treatment may also cause waviness of the edges. Assuming 26% increase in the TPB length due to wavy edges, as reported in [101], the effective TPB length of

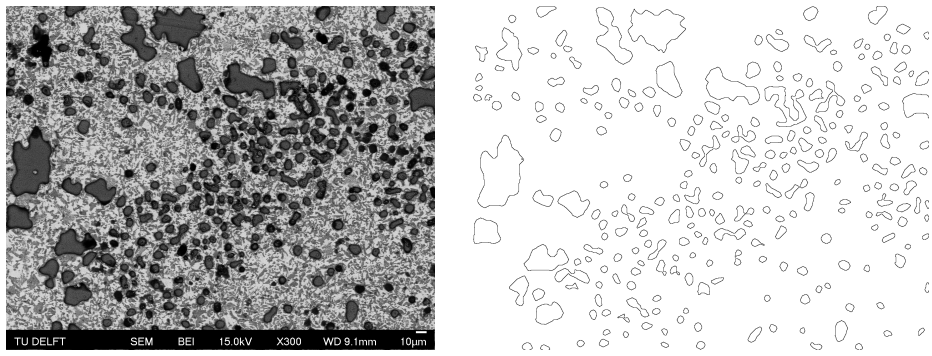

Figure 4.4 Post-test morphology of the pattern electrode: (a) raw SEM image (b) exposed TPBs due to formation of pits in the dense nickel layer

the pattern is 3.69 [m/cm^2] that is of the same order of magnitude as obtained by fitting the TPB kinetics to the experimental data.

Figure 4.5 shows the experimental and simulated polarization curves along with simulated the activation and ohmic losses. It can be seen that the simulated polarization curve is in a good agreement with the experimental data. The activation loss is found to be higher than that of ohmic loss at all current densities studied in this experiment. While ohmic loss follows Ohm's law and increases linearly with the current density, activation loss follows Butler-Volmer expression and increases rapidly in the low current density region and linearly at higher current densities. Since, exchange current density positively depends on the l_{tpb}, temperature, $p_{\mathrm{H_2}}$, and $p_{\mathrm{H_2O}}$ (equation 4.7 and 4.8), increasing any of these parameters lowers the activation loss as shown in Figure 4.6. Figure 4.6 also shows that as l_{tpb} increases, the initial rapid increase in the activation loss tends to be linear. Initial linear behavior is profound in cermet electrode as l_{tpb} is orders of the magnitude higher than that of pattern electrode. Increasing temperature favors the reaction kinetics as well as ionic transport in the electrolyte thus decreases both activation and ohmic losses. The effect of $p_{\mathrm{H_2O}}$ is significantly higher than that of $p_{\mathrm{H_2}}$ because of its higher reaction order.

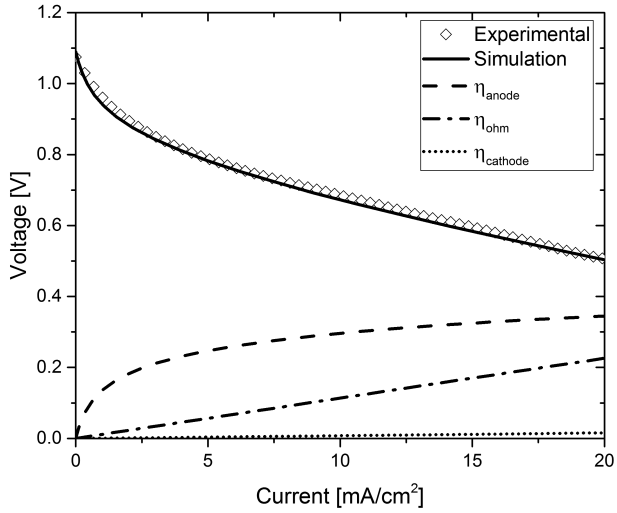

Figure 4.5 Experimental (diamond) and simulated (solid line) polarization curves for nickel pattern electrode cell. Anodic, cathodic and ohmic overpotentials are also given.

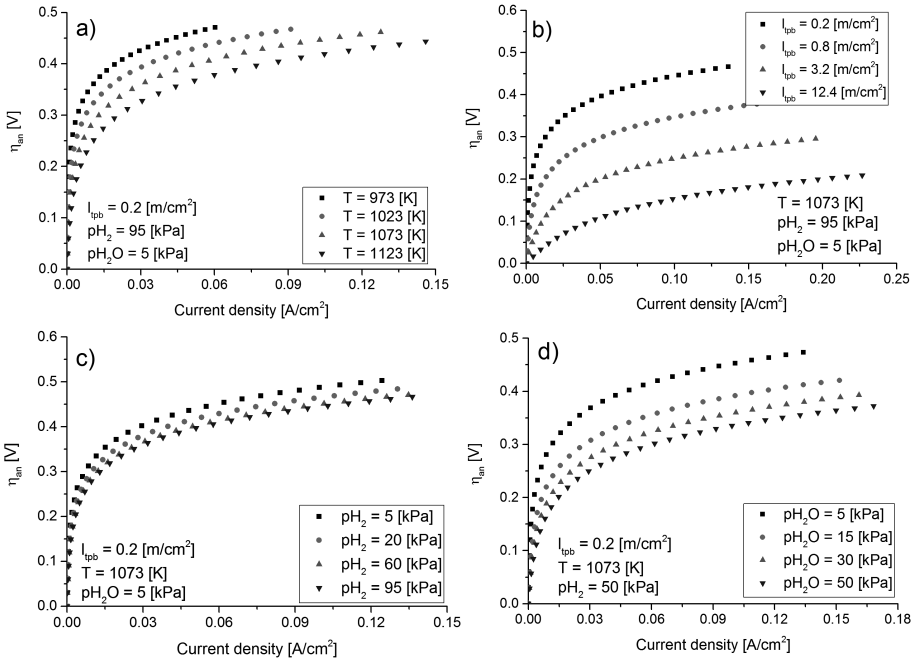

Figure 4.6 Effect of temperature, l_{tpb}, $p_{\mathrm{H_2}}$, and $p_{\mathrm{H_2O}}$ on the activation overpotential

4.6 The Butler-Volmer equation and its approximations

The hydrogen spillover charge-transfer mechanism (reaction 4.1–4.5) is a multi-step, multi-electron transfer process. The generalized Butler-Volmer equation for such a transfer process is given by [102]:

$$i = i^0 \left\{ exp\left[\left(\frac{\overleftarrow{\gamma}}{\nu} + r - r\beta \right) \frac{F\eta_{act}}{RT} \right] - exp\left[-\left(\frac{\overrightarrow{\gamma}}{\nu} + r\beta \right) \frac{F\eta_{act}}{RT} \right] \right\} \qquad (4.20)$$

here $\left(\frac{\overleftarrow{\gamma}}{\nu} + r - r\beta\right) = \alpha_a$ is the transfer coefficient in the anodic direction ($H_{Ni} + OH^-_{YSZ} \rightarrow H_2O_{YSZ} + \square_{Ni} + e^-_{Ni}$) and $\left(\frac{\overrightarrow{\gamma}}{\nu} + r\beta\right) = \alpha_c$ is the transfer coefficient in the cathodic direction ($H_2O_{YSZ} + \square_{Ni} + e^-_{Ni} \rightarrow H_{Ni} + OH^-_{YSZ}$). $\overleftarrow{\gamma}$, $\overrightarrow{\gamma}$, and r are the number of electrons transferred before, after, and in the rate-limiting step, respectively. ν is the stoichiometry of the rate-limiting step. Assuming that the rate-limiting step (here reaction 4.3) occurs only once in the overall reaction, by definition $\alpha_a > \alpha_c$ and $\alpha_a + \alpha_c = 2$. This is contrary to the common assumption of taking equal transfer coefficients based on the global oxidation kinetics. The pattern electrode cell experiments of Mizusaki [48] led to a value of $\alpha_a + \alpha_c = 2.8$, which can also not be explained by considering a unit stoichiometric number of the rate-limiting step. While modeling these experiments, Goodwin [89] proposed that the rate-limiting step may appear twice with different rate parameters so that $\alpha_a + \alpha_c = 2.8$. Goodwin further argued that such a behavior may occur because of the existence of different types of active sites that results different reaction kinetics. Besides Mizusaki, deBoer [82] also observed that $\alpha_a + \alpha_c > 2.0$. Whereas, in other pattern electrode cell experiments [16, 92], $\alpha_a + \alpha_c < 2.0$ is also observed.

Since Eq. 4.20 must be solved implicitly, there are three explicit approximations generally applied in the literature to calculate η_{act} as a function of i, and this includes: 1) Tafel equation ($\eta_{act} = (RT/\alpha_a F)\ln\left(i/i^0\right)$), 2) linear current-voltage equation ($\eta_{act} = (RT/F)\left(i/i^0\right)$), and 3) sine hyperbolic approximation ($\eta_{act} = (RT/\alpha_a F)\sinh^-\left(i/i^0\right)$) [103]. Figure 4.7

shows the computed η_{act} as a function of i/i^0 using the implicit Butler-Volmer equation and three explicit approximations. Clearly, neither linear nor sine hyperbolic approximation matches the implicit computation because of their inherent limitations. The former approximation is only valid for $i/i^0 < 1$ which is not practical in the fuel cell operation. The latter approximation also overestimates the η_{act} because it is only valid for $\alpha_a = \alpha_c$, which again does not satisfy the multi-step charge-transfer process with single rate-limiting step. The Tafel equation, on the other hand, fairly represents the expected loss at medium to high current density regions though it underestimates η_{act} at $i/i^0 < 4$.

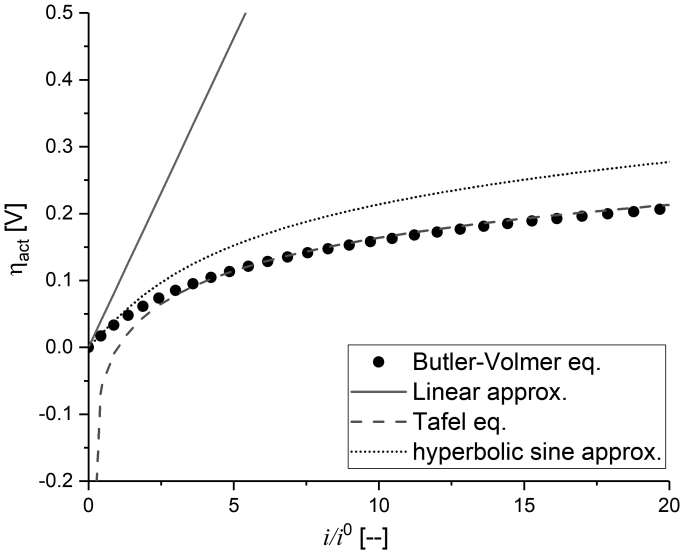

Figure 4.7 Activation overpotential as a function of dimensionless current obtained by different computational approaches. $\alpha_a = 1.4$ and $\alpha_c = 0.6$ for Butler-Volmer equation,$\alpha_a = 1.4$ for Tafel and $\alpha_a = \alpha_c = 1$ for hyperbolic sine approximation.

4.7 Implementing TPB-based kinetics in a cermet electrode cell model

So far, we have derived the TPB-based kinetics using pattern electrode cell experimental results. Recall that the exchange-current density obtained from pattern electrode (section 4.5) at T = 800 [°C], p_{H_2}= 97

[kPa], and p_{H_2O} = 4 [kPa] is 1.83x10^{-4} [A/cm^2]. This corresponds to the TPB specific exchange-current ($i^0_{l_{tpb}}$) of 3.06x10^{-6} [A/cm]. When compared with the literature, Shearing et al. [104] reported 0.94x10^{-6} [A/cm] for Ni/YSZ cermet anode using microstructure reconstruction and electrochemical characterization. Considering two widely different approaches to obtain $i^0_{l_{tpb}}$, this is of the same order of magnitude. Therefore, the kinetics we obtained can, in principle, be applied to the Ni/YSZ cermet anodes for a wide range of operating conditions. Since electrochemically active region in cermet electrodes extends beyond the electrode/electrolyte interface that requires the quantitative knowledge of volumetric TPB density (l^v_{tpb}) than the area-specific TPB length (l^a_{tpb}) to calculate the current source term. l^v_{tpb} is related to l^a_{tpb} as $l^v_{tpb} = A_s l^a_{tpb}$, where $A_s$is the catalyst specific surface area. When TPB specific kinetics is implemented in the cermet anodes, l^v_{tpb} can be treated as a free-fit parameter to match the experimental data. Thus, the fitted value may suggest the fraction of total TPB density actively participating in the electrochemical process.

To implement the TPB-based kinetics in a cermet electrode cell model we use experimental data by Jiang and Virkar [13]. Table 4.3 lists the experimental and simulation parameters. Unlike pattern anodes, the concentration overpotential is also included here while simulating the polarization behavior of cermet electrode cell. Cathodic exchange-current density is obtained by the expression proposed in [96]. Also, the experimental OCV is used here rather than calculating from the Nernst equation. The coupled gas transport and electrochemical model is solved in COMSOL Multiphysics V5.1.

Figure 4.8 shows the experimental and simulated polarization curves for four different H_2/H_2O gas mixtures at 800 [^{o}C]. It can be seen that the model captures the qualitative changes in the current-voltage relationship and when l^v_{tpb} is assigned 1.78x10^7 [m/m^3] a reasonably good fit is observed between the results from simulation and experiments. Figure 4.9 further compares the anodic activation overpotential we obtained with the simulated results of Lee et al. [106] for the same experimental data set that also shows that the assigned value of l^v_{tpb} provides a reasonably good fit. The physical TPB density reported in the literature,

Parameter	Value
Anode	
Thickness [13]	1220 [μm]
Porosity/tortuosity	0.1
Catalyst specific surface area (A_s) [96]	1.08x10^5 [m^2/m^3]
Symmetry factors (β_a, β_c)	0.3, 0.7
Cathode	
Thickness [13]	30 [μm]
Catalyst specific surface area (A_s) [96]	1.08x10^5 [m^2/m^3]
Porosity/tortuosity	0.1
Symmetry factors (β_a, β_c)	0.5, 0.5
$i^*_{O_2}$ [96]	2.80 [A/cm^2.atm$^{1/2}$]
Electrolyte	
Thickness [13]	10 [μm]
Ionic conductivity [105]	3.34x10$^4 e^{-10300/T}$ [S/m]
General parameters	
Cell temperature [13]	800 [^{o}C]
Operating pressure [13]	1 [atm]

Table 4.3 A summary of simulation parameters for Ni/YSZ cermet electrode cell model

obtained by microstructural reconstruction of Ni/YSZ cermet electrodes, is typically of the order of 10^{12} to 10^{13} [m/m^3] [107, 108] that is several orders of magnitude higher than the value obtained in this work. This possibly suggests that only a small fraction of the total TPB length is actually active for electrochemical process.

The TPBs closer to the anode/electrolyte interface are expected to be the preferred reaction sites to those at the gas/anode interface. For thick anodes, only a fraction of the total thickness, commonly known as the active layer, is sufficient to carry out the charge-transfer reac-

tions. The thickness of this active layer is reported in literature with significant variations. For example, Chen et al. [109] and Nagasawa and Hanamura [110] reported the thickness to be less than 5 [μm], Cai et al. [111] reported 5-15 [μm], Primdhal and Mogensen [112, 113], Moon et al. [114], and Li et. al [115] reported the thickness of up to 20 [μm]. Thickness higher than 40 [μm] is reported as well [116, 23]. Variations in the reported values are mainly due to difference in the anode composition, microstructure, and operating conditions. While active thickness is an important information in designing better electrodes, it does not explicitly help in comparing the performance of various electrode designs operating at different conditions. Further, merely the active thickness is not very helpful in simulating the cell degradation related to variation in the TPBs over the course of time while operating under stringent conditions. For example, sulfur present in the fuel causes irreversible degradation of the cell performance because sulfur diffuses into the nickel bulk and leads to the detachment of nickel particles from their original position and an associated reduction in the TPB length [117, 118]. Simulating the behavior of such system requires quantitative knowledge of the TPBs. The use of model electrode designs made possible to determine the TPB-based reaction kinetics that may be used to estimate the effective TPB density of electrodes of commercial cells. To the best of our knowledge, no such study is available so far that directly makes use of the TPB-based kinetics to estimates the effective TPB density of cermet anodes. Therefore, the comparison of effective TPB density as obtained here is not possible. Work is also ongoing to further refine the model and validate using experimental results obtained by anodes of different thickness. The present set of results provides quantitative knowledge of the effective TPB density of a thick cermet anode as well as supports the validity of the assumption of small active layer thickness. When these studies are extended, it will help to understand the SOFC anodes better and this is necessary in designing power plants based on SOFCs and realistic fuel choices.

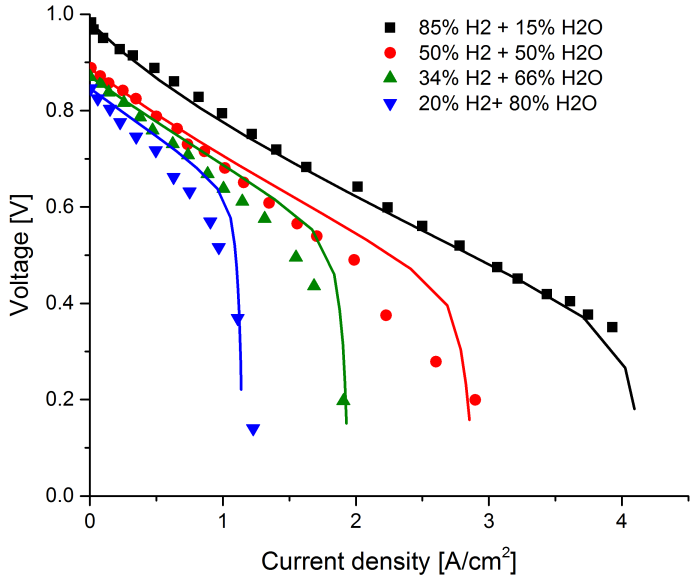

Figure 4.8 Experimental and simulated polarization curves for H_2/H_2O system at 800 [°C]

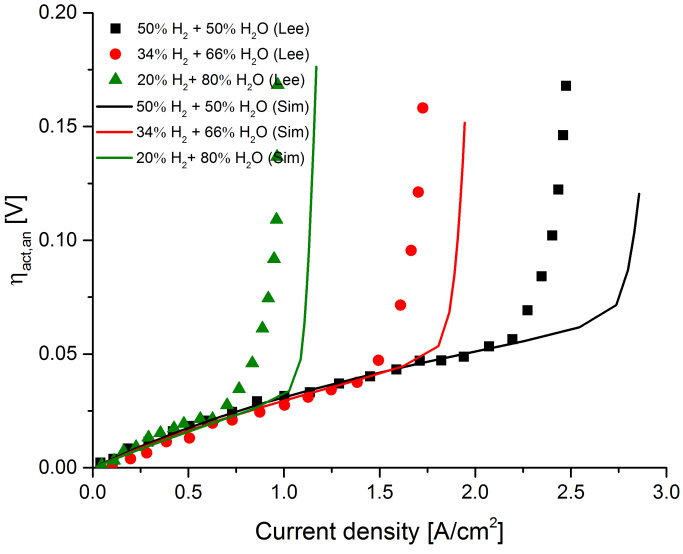

Figure 4.9 Simulated anodic activation overpotential of the cermet electrode cell

4.8 Conclusions

The TPB-based kinetics lead to a better prediction of the cell performance and give information about the effective TPB length. Expression of the anodic exchange-current density, previously derived considering a detailed reaction scheme and the charge-transfer reaction as the rate-limiting step, is used in this work to derive the TPB-based kinetics. The explicit dependence of the expression on TPB length, temperature, and gas-phase activities enabled estimating the exchange-current density over a wide range of operating conditions. Using nickel pattern electrode cell, the TPB specific exchange-current for hydrogen oxidation (97% H_2 and 3% H_2O) at 800 [^oC] is found to be 3.06x10^{-6} [A/cm] which is of the same order of magnitude of the reported value (= 0.94x10^{-6} [A/cm]) for Ni/YSZ cermet electrode cell obtained by 3D reconstruction at similar conditions. This kinetics is first validated using button cells with nickel pattern anode and platinum porous cathode and then extended for cermet anodes. While implementing this kinetics in Ni/YSZ cermet electrode cell model, we obtained an effective TPB density of 1.78x10^7 [m/m^3] which is several orders of magnitude lower than the reported physical TPB densities of cermet anodes. Very low TPB density possibly suggests that only a minor fraction of the total TPB is actually required to produce the total cell current at given cell voltage. The present set of results also support the validity of the assumption that the electrochemically active region only extends to a few microns from the anode/electrolyte interface.

5

Effect of HCl contaminant on pattern and cermet anodes

Besides H_2 and CO, syngas also contains varying levels of HCl contaminant which can potentially degrade the anode performance. Therefore, understanding the interaction chemistry between HCl and anode materials is of critical importance for designing chlorine-tolerant materials. In this work, we investigate the effect of 60 and 150 ppm(v) HCl gas on nickel pattern, ceria pattern, and nickel/gadolinium-doped ceria (Ni/GDC) cermet electrode cells using electrochemical impedance spectroscopy (EIS). Post–experiment surface analysis is also carried out using Energy-dispersive spectroscopy (EDS) and results are reported.

5.1 Introduction

Besides hydrogen, SOFCs are capable of oxidizing practical fuels like natural gas, biogas, and synthetic gas (syngas) due to their high operational temperature and conduction of oxide ions through the electrolyte. These fuels may also contain varying levels of contaminants like H_2S and HCl depending upon their source and manufacturing process. HCl concentration as high as 500 ppm(v) in coal syngas and 200 ppm(v) in biosyngas is reported that is likely to affect the anode performance [119, 120]. Effect of HCl and other chlorine compounds such as Cl_2 and CH_3Cl on the SOFC performance has been addressed in several studies [33, 119, 121–126]. Key findings from these studies include: 1) the effect of HCl on the cell performance is insignificant at concentrations less

than 50 ppm(v) [33, 121, 122, 125, 126], 2) higher concentrations may lead to both reversible [119, 123] and permanent performance losses [124], 3) increase in temperature decreases HCl related degradations [123], and 4) anode supported cells (ASC) tend to be more tolerant to HCl as compared to the electrolyte supported cells (ESC) [124].

Major source of performance loss in above studies has been attributed to the adsorption of Cl species on the nickel surface and the possibility of nickel chlorination (formation of $NiCl_2$) is ruled out in most of these studies. To the best of our knowledge, all relevant studies reported in the literature have been carried out using cermet electrodes, whereas the model geometries like point and pattern electrodes have never been tested. It should be noted that any plausible effect of HCl on the electrochemistry at the catalytic sites (triple-phase boundaries (TPBs) and two-phase boundaries (2PBs)) is difficult to quantify with the cermet electrodes because the complex microstructure related effects like gas diffusion may dominate over the reaction kinetics.

Besides Ni/YSZ, knowledge of the interaction chemistry between HCl and ceria is also essential because of the growing interest of ceria application as alternative anode material for hydrocarbon fuels. From catalysis literature, it is known that ceria is an effective catalyst for HCl oxidation at 350–450 ^{o}C temperature and in the presence of over-stoichiometric supply of oxygen, the oxidation process is known as Deacon process [127]. Ceria retains its catalytic activity due to the presence of excess oxygen. For anode applications, though HCl concentration level in hydrocarbon-based fuels is expected only at the ppm level, catalytic activity of ceria may degrade because of the reducing conditions of anode [128]. Since, nickel/ceria cermet is considered as an alternative to conventional nickel/YSZ cermet for anode applications, it is equally important to study the effect of HCl on nickel and ceria separately to identify the poisoning effect on individual and establish their kinetics. It is known that the pattern electrode cells are well suited for studying the reaction mechanisms and identifying the rate-determining step(s)[48, 5]. Such simplified 2D geometries can, in principle, be applied to study the effect of syngas contaminants on the anode electrochemistry and establish the kinetics of anode poisoning and recovery.

While previous studies mainly focused on investigating the effect of HCl on Ni/YSZ and Ni/GDC cermet, this is first time, to the best of our knowledge, that pattern electrode cells are tested in an HCl contaminated H_2/H_2O environment. We prepared nickel and ceria pattern electrodes on YSZ substrate and tested with 60 and 150 ppm(v) of HCl contamination levels using electrochemical impedance spectroscopy (EIS). In order to compare the results with literature, electrolyte-supported Ni/GDC cermet electrode cells are also tested in the same gas atmosphere.

5.2 Experimental

Preparation of nickel and ceria patterns is described in Chapter 2. The electrolyte supported nickel/GDC symmetrical button cells were received from H.C. Starck. The cells were placed between square gold meshes (1024 mesh/cm^2) acting as current collectors. A schematic of the test assembly is shown in Figure 5.1. The electrochemical measurements were carried out with Gamry potentiostat (Reference 600) using 15 mV sinusoidal perturbation and in a frequency range of 100 kHz to 0.01 Hz (12 points/decade). All of these measurements were conducted in a 4% humidified hydrogen atmosphere between 750 and 850 °C temperature.

Prior to testing with HCl contaminant, cells were heated from room temperature to 850 ^oC at a rate of 40 ^oC/hr. During the heating phase, cells were flushed with 100 ml/min of nitrogen gas. After achieving the target temperature, inlet gas was gradually switched from dry nitrogen to 4% humidified hydrogen. Impedance spectra were recorded at fixed time intervals (after 2 hrs) to monitor the cell stabilization and perform electrochemical characterization. In all three cells, it took more than 24 hours before a stable spectrum, after achieving the target temperature, could be recorded. Once the spectra were stabilized, two HCl concentration levels (60 and 150 ppm(v)) were tested by adding a HCl/H_2 gas mixture to the primary hydrogen stream while keeping total flow (100 ml/min) the same. Distilled water was injected through a syringe pump to ensure a constant 4 % humidity level in all gas atmospheres. After electrochemical measurements, cells were also analyzed with Scanning

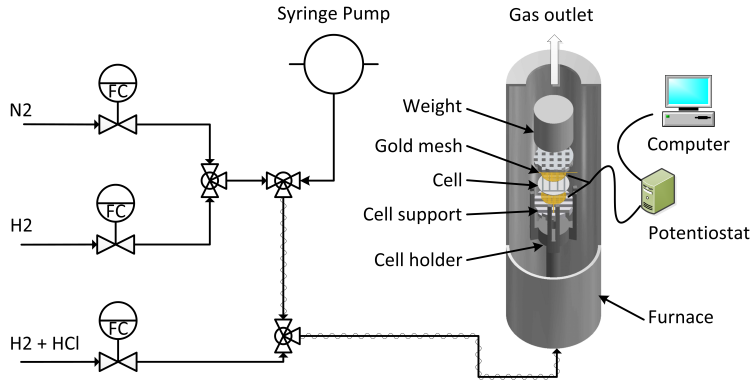

Figure 5.1 Schematic of the test assembly

Electron Microscopy (SEM) and Energy Dispersive spectroscopy (EDS) (JEOL JSM-6500f).

5.3 Results

5.3.1 Electrochemical characterization

Figure 5.2a shows the impedance spectra of nickel pattern electrode cells with H_2/H_2O prior to contamination, with H_2/H_2O contaminated with 60 and 150 ppm(v) HCl, and after removing HCl from the gas stream. Time stabilization of the polarization resistance is illustrated in Figure 5.2b. It can be seen that adding HCl lowers the polarization resistance. The polarization resistance at 150 ppm(v) HCl is less than half of the resistance initially observed before HCl addition. The resistance after removing HCl from the gas stream is found to be higher than with HCl contaminated gas, however almost 15 % lower than the resistance recorded before HCl addition.

The impedance spectra and time stabilization of the polarization resistance with ceria pattern electrode cells are illustrated in Figure 5.3a and 5.3b, respectively. Similar to nickel cells, exposing ceria cells to HCl contaminated gas also lowers the polarization resistance. However, unlike nickel, the polarization resistance after removing HCl is found to be slightly higher than the resistance recorded prior to contamination. Figure 5.3b shows that ceria is also highly sensitive to HCl gas similar

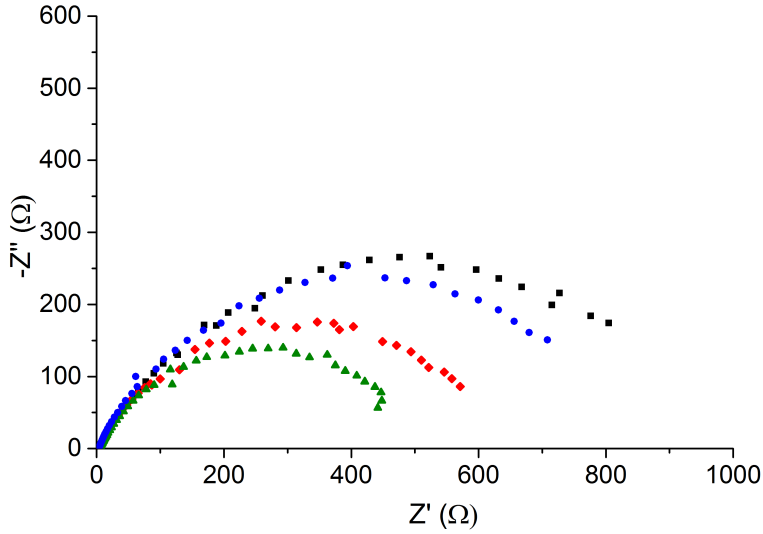

(a) Impedance spectra for four different gas atmospheres

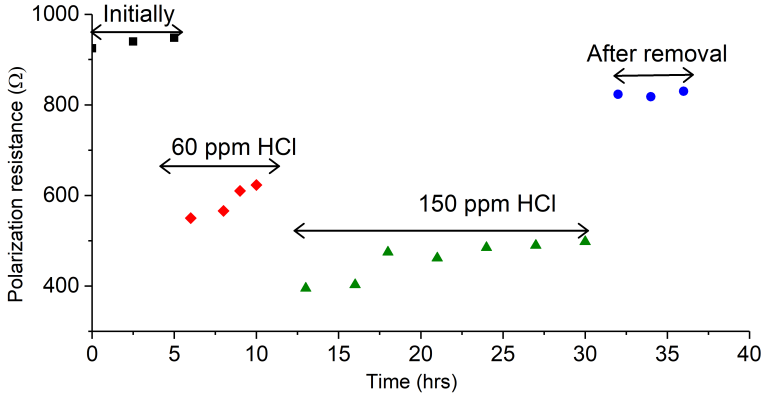

(b) Time stabilization of the polarization resistance with change in gas atmosphere

Figure 5.2 EIS measurements with nickel pattern electrode cells at 800 [°C]. H_2/H_2O gas before HCl addition in (■), H_2/H_2O/60 ppm(v) HCl in (◆), H_2/H_2O/150 ppm(v) HCl in (▲), and after HCl removal H_2/H_2O gas in (●).

to nickel as changing HCl concentration at ppm level results in a quick change in the polarization resistance.

We further studied the effect of HCl on Ni/GDC cermet electrode cells and the results are shown in Fig. 5.4. Unlike pattern electrodes, the polarization resistance remains unchanged at 60 ppm(v), only slightly increases at 150 ppm(v). To see whether higher concentration accelerates the degradation, impedance spectra with 300 ppm(v) are also recorded. It is found that the polarization resistance with 300 ppm(v) HCl is almost 25 % higher than the resistance without HCl gas. A significant increase in the polarization resistance with Ni/GDC cells at higher concentrations is consistent with the reported trend [121, 124].

5.3.2 Post-test analysis

We also performed a post-test surface analysis of nickel and ceria pattern electrodes using SEM/EDS. SEM images reveal that both nickel and ceria patterns could not remain stable and intact during the experiment as shown in Figure 5.5a and 5.5b, respectively. The edges of nickel patterns became wavy and the thick pattern layer developed several holes. In case of ceria, several patches of the pattern are washed away. It should be noted that, the polarization resistance for hydrogen oxidation on ceria is almost an order of magnitude higher than what we found in Chapter 2 at similar conditions. The erosion of ceria pattern and reduction in the active area may have resulted in this high polarization resistance.

The results of line scan EDS are also shown in Figure 5.5c and 5.5d. Only traces of chlorine are observed on both nickel and ceria surface. Traces of chlorine observed on nickel surface during post-test surface analysis have also been reported previously [121, 124] and were attributed to the adsorbed Cl species at nickel surface. Interestingly silicon and carbon elements are also detected on ceria surface. The source of silicon is expected to be the silicon paste that we applied as a gas sealant in the inlet pipes.

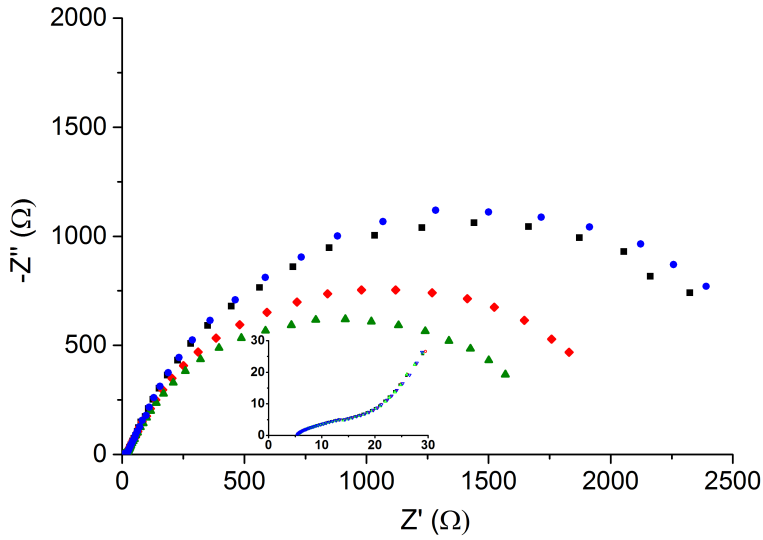

(a) Impedance spectra for four different gas atmospheres

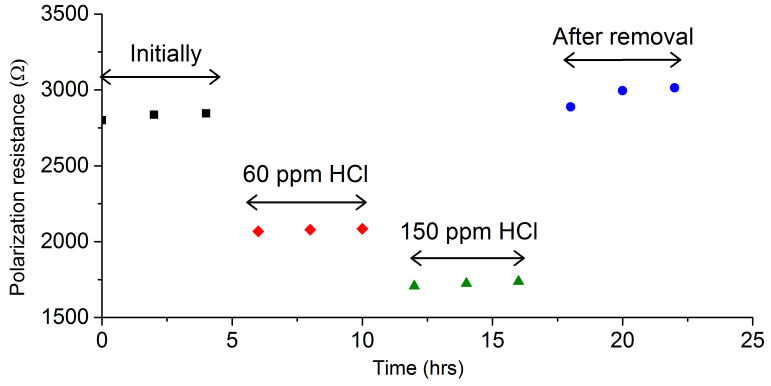

(b) Time stabilization of the polarization resistance with change in gas atmosphere

Figure 5.3 EIS measurements with a nickel pattern electrode cells at 800 °C. H_2/H_2O gas before HCl addition in (■), H_2/H_2O/60 ppm(v) HCl in (◆), H_2/H_2O/150 ppm(v) HCl in (▲), and after HCl removal H_2/H_2O gas in (●).

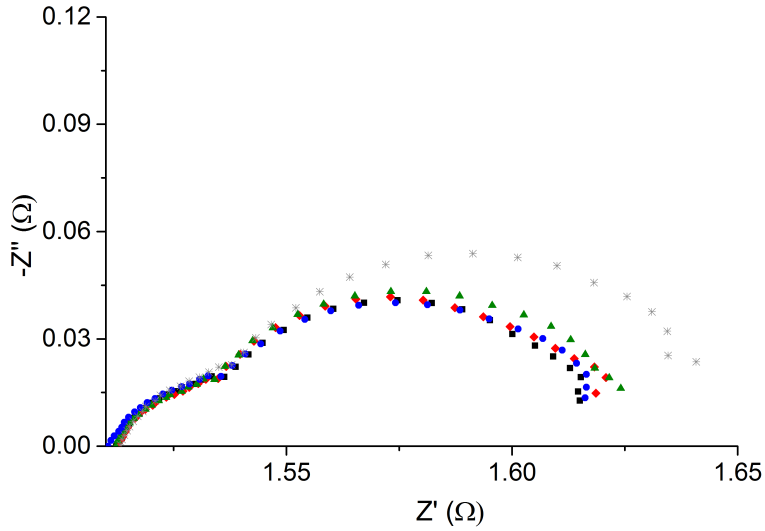

Figure 5.4 Impedance spectra for nickel/GDC cermet electrode cells at 800 [°C]. H_2/H_2O gas before HCl addition in (■), H_2/H_2O/60 ppm(v) HCl in (♦), H_2/H_2O/150 ppm(v) HCl in (▲), H_2/H_2O/300 ppm(v) HCl in (✳), and after HCl removal H_2/H_2O gas in (●).

5.4 Discussions

Electrochemical measurements with pattern electrode cells show that the polarization resistance drops, unlike cermet electrod cells, for both nickel and ceria pattern electrode cells. In previous studies with Ni/YSZ and Ni/GDC cermet electrodes, where reversible performance degradation was observed at higher HCl concentrations, degradation was attributed to the adsorbed Cl species at the catalyst surface. This adsorption can be analyzed in the perceptive of nickel and ceria catalysts separately. On nickel surface, the dissociative adsorption of HCl may be represented as:

$$\mathrm{HCl(g)} + \square_{\mathrm{Ni}} \leftrightarrow \mathrm{Cl_{Ni}} + \frac{1}{2}\mathrm{H_2(g)} \tag{5.1}$$

here $\square_{\mathrm{Ni}}$ is a free adsorption site at nickel surface and $\mathrm{Cl_{Ni}}$ is the corresponding adsorbed chlorine specie. $\mathrm{Cl_{Ni}}$ occupies the free surface sites on nickel therefore decreasing the number of available sites for

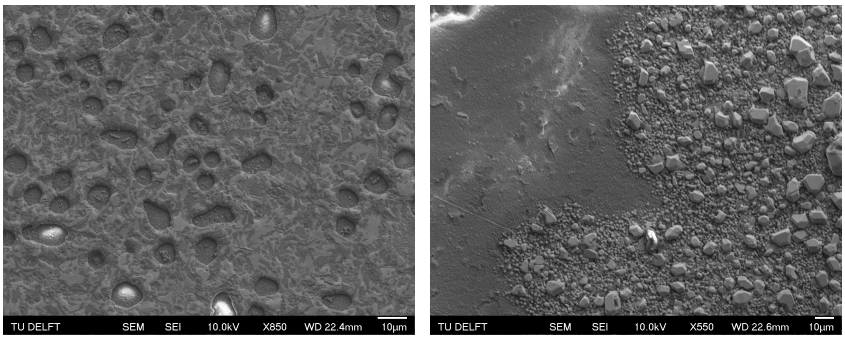

(a) (b)

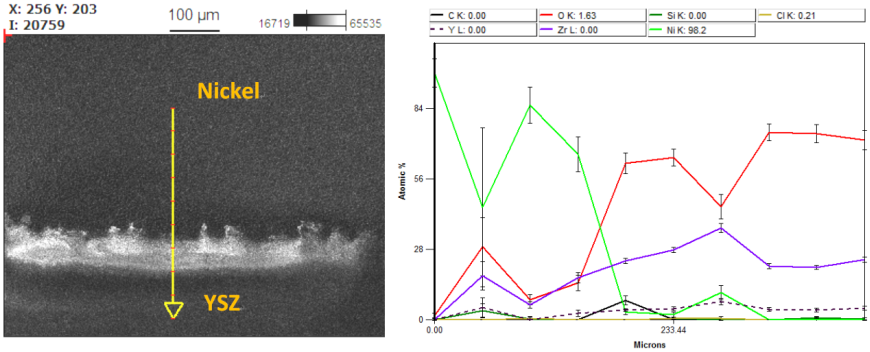

(c)

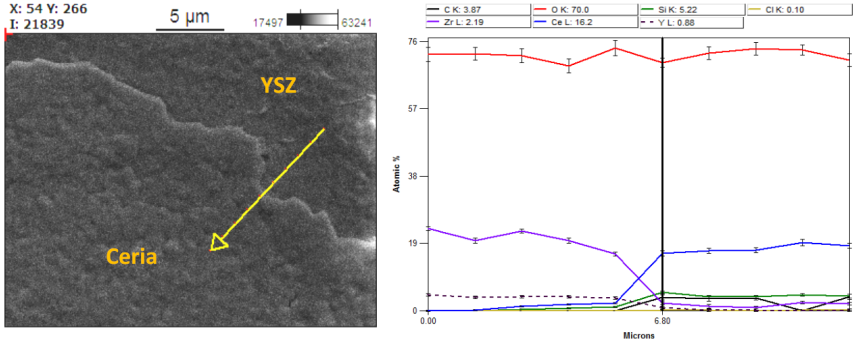

(d)

Figure 5.5 Post-test characterization of nickel and ceria pattern electrodes (a) SEM image of nickel pattern, (b) SEM image of ceria pattern, (c) line scan EDS of nickel electrode, and (d) line scan EDS of ceria electrode

hydrogen adsorption and subsequent electrochemical oxidation. As a consequence, the the cell performance should degrade as also reported in [119, 123, 124]. However, better cell performance is observed in the presence of HCl gas in this study. Alternately, HCl can react with nickel catalyst and form $NiCl_2$ as:

$$Ni(s) + 2HCl(g) \rightarrow NiCl_2(g) + H_2(g) \tag{5.2}$$

Gaseous $NiCl_2$ will move out of the anode surface and lower the nickel/YSZ ratio of the cermet that will eventually result in a permanent degradation [129]. Whether, the formation of $NiCl_2(g)$ is feasible at the cell operating conditions, we performed an equilibrium calculation using FactSage software [130], and results are shown in Figure 5.6. At 800 ^{o}C, the gas phase activity of $NiCl_2(g)$ is of the order of 10^{-14} that is too small to cause any noticeable difference in the performance. In our experiments, neither an increase in the polarization resistance is observed upon adding HCl to H_2/H_2O gas, nor any permanently higher polarization resistance is witnessed after removing HCl from the gas stream. Rather, a decrease in the resistance is found (Figure 5.2a) upon adding HCl, which cannot be explained by any argument presented before.

Electrochemical oxidation on nickel pattern electrode cells is restricted to the TPB between nickel, YSZ, and gas phases. Higher the TPB length, the better will be the cell performance. While it is known that the thermal treatment and electrochemical measurements may deteriorate the sharp TPB line between nickel and YSZ [81], as also observed in SEM images, that will expose a higher TPB length and result in a lower polarization resistance. Whether, HCl plays any critical role in deteriorating the interface or washing out any segregated impurity at the TPB is not known to our knowledge. A detailed surface analysis may provide further insight.

Similar to nickel pattern electrode cells, ceria pattern electrode cells have also shown lower polarization resistance upon adding HCl. While ceria is a potential catalyst for producing Cl_2 gas at Deacon conditions

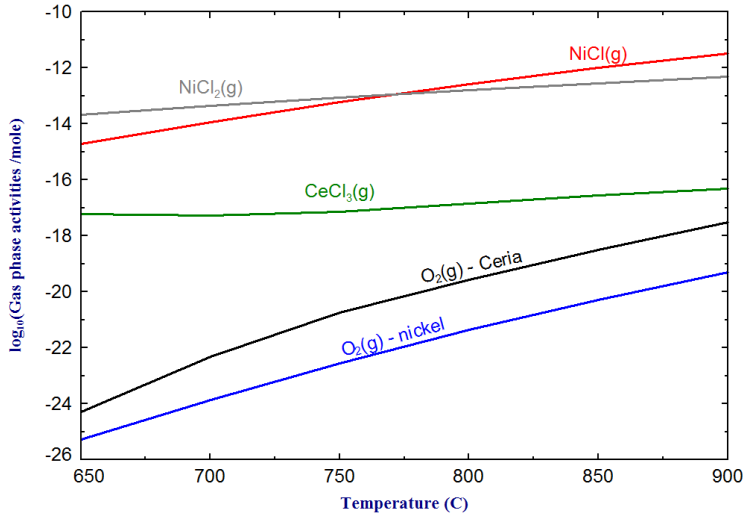

Figure 5.6 Gas phase activities of nickel and cerium chloride species

(350–450 °C and $O_2/HCl \geq 1$), it does forms chlorinated phase in a sub-stoichiometric environment ($O_2/HCl \leq 0.25$) and undergoes a reversible deactivation [131]. In this study, the formation of chlorinated cerium may be ruled out because only traces of chlorine were detected in the EDS analysis as evident from Figure 5.5d. Further, the gas phase activity of $CeCl_3$ at 800 °C is too low (Figure 5.6) to cause any considerable loss of cerium. Even, if ceria chlorination happens, the polarization resistance should increase that is contrary to our observations. The ceria patterns were found degraded in SEM images that is not expected to be a result of HCl as the cell performance was found by and large reversible upon adding and removing HCl. What caused the decrease in polarization resistance, remains unknown at this point.

The observations made with Ni/GDC cermet electrode cells are in line with the reported trend in the literature [121, 124]. The active sites in cermet electrode are significantly higher than the pattern electrode due to which the resistance from TPB related process may be insignificant compared to the resistance of other physiochemical processes. This may be a reason that unlike pattern electrode no effect of HCl on the cell performance is observed at low concentrations. The understanding of Ni/GDC anode electrochemistry is insufficient due to which it is difficult

to mechanistically relate the interaction of HCl with Ni/GDC. Further investigations with the model anode geometry are therefore suggested.

5.5 Conclusions

The effect of 60 and 150 ppm(v) HCl is investigated on nickel pattern, ceria pattern, and Ni/GDC cermet electrode cells using the electrochemical impedance spectroscopy. Lower polarization resistance is observed when 60 and 150 ppm(v) HCl contaminants are added to the H_2/H_2O gas. This observation is made with both nickel and ceria pattern electrodes. In case of Ni/GDC cermet electrode cells, the polarization resistance remains unchanged for 60 ppm(v). However, higher HCl levels (150 and 300 ppm(v)) cause a recoverable performance loss.

6

Conclusions

Commonly SOFC anodes are made of cermets of nickel and YSZ or nickel and doped ceria. These materials have high electrochemical performance, however, their electrochemistry is not properly established. Studying the kinetics with cermet electrodes is difficult due to challenges regarding specifying the reaction sites and due to the interference of structure related process. Pattern electrodes have a non-porous 2D structure with well-defined TPB length (in case of metal electrodes) or 2PB (in case of MIEC electrodes) suitable for studying the reaction kinetics and identifying the rate-determining step(s). Due to the non-porous structure, the microstructural and even the gas-phase effects are negligible in pattern electrodes that may dominate over the reaction kinetics in case of cermet electrodes.

In this thesis, the electrochemistry of nickel and ceria anodes is investigated in multifuel environments. Further, the interaction chemistry between HCl contaminant and anode materials (nickel and ceria) is studied using pattern electrode cells and results are compared with the influence on nickel/GDC cermet anode. In addition to the experimental work, mathematical models are also developed including an elementary kinetic model using the mass-action kinetic approach to study the co-oxidation of H_2 and CO in syngas (chapter 2), the Nernst-Planck-Poisson model with a detailed reaction mechanism to identify the rate-determining step during hydrogen electrochemical oxidation on ceria (chapter 3), and an electrochemical model using the TPB-based kinetics to simulate the polarization behavior of hydrogen electrochemical oxidation on the Ni/YSZ cermet anodes (chapter 4). The key findings

made in this thesis and recommendations for future work are summarized below.

6.1 Key findings of this thesis

This thesis has presented an understanding of the nickel and ceria anode electrochemistry in H_2, CO, and syngas environments. It is reaffirmed that the pattern electrodes can provide means to study the electrochemical reaction kinetics and solid-state diffusion of bulk defects, and investigate the influence of gas contaminants on the cell performance. Direct CO electrochemical oxidation is often ignored in macroscale models, however such an assumption may not be valid at high CO concentration levels especially for ceria electrodes. Ceria is not only an oxide-ion conductor but a favorable electrochemical catalyst as well – the activity of ceria can even be higher than nickel as found in this thesis. Further, it is found that the defect (electron and oxide-ion vacancies) transport is faster than the reaction kinetics due to which the electrochemically active region can extend beyond the electrode/electrolyte interface. This characteristic is of vital importance for developing anode-supported cells. The TPB-based kinetics derived in this thesis can directly be used in a CFD model to simulate the performance of Ni/YSZ cermet electrode cells, estimate the effective TPB density, and optimize the electrode design. The effective TPB density found in Ni/YSZ cermet anode is several orders of magnitude lower than the typical physical TPB densities reported in the literature indicating that only a minor fraction of total TPB density is actually required to produce the cell current. Moreover, this work gave a unique insight into the influence of HCl on nickel and ceria which has not been revealed so far.

A detailed overview of the chapter wise findings is presented below.

Chapter 2:

Ceria pattern electrode cells showed a lower polarization resistance and activation energy than nickel in all gas environments tested in this work, indicating a better catalysis on ceria than nickel. The polarization resistance of H_2 oxidation was found lower than that of CO on both electrodes, indicating an ease of H_2 oxidation than CO. Further, the polarization resistance of syngas oxidation was found closer to that of H_2

oxidation than that of CO, pointing towards the preferential oxidation of H_2 in the syngas mixtures. Adding a small amount of steam to CO caused a significantly larger drop in the polarization resistance compared to the drop caused by adding steam to H_2 that is attributed to the combined effect of WGS conversion and a preferential oxidation of hydrogen produced as a result of WGS reaction. Elementary kinetic modeling revealed that CO may also electrochemically oxidize, in addition to H_2, depending upon its concentration in the syngas.

Chapter 3:

The Nernst-Planck-Poisson model revealed that the bulk diffusion of ions and electrons is faster in a thin-film ceria pattern anode equipped with an efficient current collection mechanism than the kinetics of hydrogen electrochemical oxidation. The charge-transfer between the hydroxyl-ions and the cerium-ions is the slowest and the rate-determining step. The derived expression of the exchange-current density based on the rate-determining step (Eq. 3.21 or Eq. 3.24), reasonably predicts the experimentally obtained exchange-current density over a wide range of temperature and hydrogen partial pressure.

Chapter 4:

We derived the TPB-based kinetics of hydrogen electrochemical oxidation on nickel using nickel pattern anode experimental results. TPB specific exchange-current is found to be 3.06×10^{-6} [A/cm of the effective TPB length] at T = 800 [°C], p_{H_2} = 9.7 x 10^4 [Pa], and p_{H_2O} = 4.0 x 10^3 [Pa]. Using TPB-based kinetics, the effective volumetric TPB density of Ni/YSZ cermet anode is found to be 1.78 x 10^7 [m/m^3] which is several orders of magnitude lower than the reported physical TPB densities of the cermet electrode (= 10^{12} to 10^{13} [m/m^3]). This indicates that only a very minor fraction of the total TPB density is actually required to produce the cell current.

Chapter 5:

We also found that feeding 60 and 150 ppm(v) HCl gas to nickel and ceria pattern electrode cells lowers the polarization resistance. Apparently, HCl leaves a permanent footprint on both of the pattern electrodes as the polarization resistance after removing HCl was lower on nickel

and higher on ceria compared to the resistance before adding HCl. This is the first time that we observed a decrease in the polarization resistance with HCl contaminant. The polarization resistance for Ni/GDC cermet electrode cells remained unchanged for 60 ppm(v) and increased for higher concentration levels (150 and 300 ppm(v)) that is in line with the reported trend in the literature.

6.2 Future work recommendations

The experimental and modeling results presented in chapter 2 provided detailed kinetics of the fuel oxidation. We further compared the kinetics of H_2 and CO oxidation in syngas environment at equilibrium. Since the experimental setup was designed for measurements with the symmetrical pattern electrode cells in a single gas chamber, the effect of cell potential or current density on the relative kinetics of H_2 and CO oxidation in syngas could not be established. It is important to study the effect of potential on the reaction kinetics as the electrochemical reactions involve charged species, the energy level of which is sensitive to the change in voltage. By driving the cell potential away from equilibrium, the rate of forward or reverse reactions is favored depending upon the direction of applied activation overpotential and height of the resultant activation barrier. Quantitatively, the symmetry factor (β) indicates how changing electrical potential across the reaction interface changes the height of forward vs reverse activation barriers. Therefore, conducting experiments under anodic biasing may also help in further exploring the kinetics of fuel oxidation and the effect of contaminants as well. Similar work with the cathodic biasing is relevant for electrolysis as well where in case of H_2O/CO_2 mixture, the relative kinetics of H_2O and CO_2 electrolysis can be established.

The reaction mechanism used for syngas oxidation on ceria in chapter 2 (table 2.4) simply merged the mechanisms of H_2 and CO oxidation and did not consider the intermediate species such as formates (HCO_2^-) and hydrogen carbonates ($CO_2(OH)^-$)[132]. To this point, the true significance and relevance of these species is not clear. Therefore, a further refinement of the model incorporating these intermediates is suggested. Validation of the refined model over a wide range of operating conditions (current density, temperature, and syngas composition) may present an

important step in the development of ceria electrode cells for hydrocarbon fuels.

While we developed the kinetics of hydrogen electrochemical oxidation on dense film of undoped ceria, the cermets of gadolinium-doped ceria (GDC) are often preferred because GDC provides an enhanced oxide-ion vacancy concentration, therefore, the higher ionic conductivity compared to undoped ceria. Meanwhile oxide-ion vacancies favor the adsorption of H_2O compared to H_2. Though we speculate that it will not change the proposed reaction mechanism (chapter 3) and the rate-determining step (reaction 3.2), it may have an influence on the overall kinetics. Additionally, we have shown that the transport of ceria bulk defects is fast enough, at least up to 100 μm for electrons and 1 μm for vacancies, compared to the reaction kinetics to have any significance in a viewpoint of the overall resistance. These results provide a basis for studying the thin-film microporous anode of ceria, a composite system such as Cu/CeO_2, and eventually a more complex ceria cermet such as nickel/GDC.

Similarly, useful extension of this work would involve understanding the interaction chemistry between HCl, and nickel and ceria. A similar study with GDC pattern anode may also provide a useful insight. In-situ spectroscopic techniques can be used as a valuable tool to prob the interaction between HCl and anode material.

Nomenclature

List of symbols

a	species activity
A	electrode active area [m^2]
c_k	concentration of surface species [mol/m^2]
C_k	concentration of bulk species [mol/m^3]
D	diffusion coefficient [m^2/s]
$\mathscr{D}$	ambipolar diffusion coefficient [m^2/s]
E_{act}	activation energy [J/mol]
E_{cell}	cell voltage [V]
E^{eq}	equilibrium potential [V]
F	Faraday constant [96485 C/mol]
$\triangle H$	enthalpy change of a reaction [kJ/mol.K]
i	current density [A/m^2]

i_o	exchange-current density [A/m^2]
J	electrochemical flux [mol/m^2.s]
$\vec{k}$ & $\overleftarrow{k}$	forward & backward reaction rate constants
K	equilibrium constant
l_{tpb}	area-specific TPB length [m/cm^2]
l^v_{tpb}	Volumetric TPB density [m/m^3]
p	pressure [Pa]
R	gas constant [J/mol.K]
R_{chem}	surface reaction/charge-transfer resistance [ohm]
R^{CP}_{ion}	cross-plane ionic resistance [ohm]
R^{IP}_{eon}	in-plane electronic resistance [ohm]
R_{ct}	charge transfer resistance [ohmcm^2]
$\dot{s}_k$	net rate of generation of surface species [mol/m^2.s]
$\triangle S$	entropy change of a reaction [J/mol.K]
T	temperature [K]
$[X_k]$	fractional coverage of surface specie
z_k	formal charge

Greek symbols

v_{ki}	stoichiometric coefficient of reactant k in the ith reaction (-)
$\tilde{\mu}$	electrochemical potential [J/mol]
ϕ	electric potential [V]
ε	permitivity [F/m]
β	symmetry parameter
α	charge transfer coefficient
η	overpotential [V]
σ	electrical conductivity [S/m]
θ	coverage of surface specie
ψ_{tpb}	effective TPB fraction
Γ	surface site density [mol/m^2]

Abbreviations and acronyms

act	activation
an	anode
ca	cathode
conc	concentration
eq	equilibrium
eon/el	electronic

hf	high-frequency
lf	low-frequency
ohm	ohmic
AFC	Alkaline fuel cell
GDC	Gadolinium-doped ceria
MCFC	Molten carbonate fuel cell
OCV	Open circuit voltage
PAFC	Phosphoric acid fuel cell
PEMFC	Polymer electrolyte membrane fuel cell
SOFC	Solid oxide fuel cell
TPB	Triple-phase boundary
WGS	Water-gas shift
YSZ	Yttrium-stabilized zirconia
Pattern	Dense patterns of functional anode material
Cermet	Ceramic/metal porous composite anode

Bibliography

[1] International energy outlook 2016 (IEO2016). Technical Report DOE/EIA-0484(2016), U.S. Energy Information Administration (EIA), 2016.

[2] Steven McIntosh and Raymond J Gorte. Direct hydrocarbon solid oxide fuel cells. *Chemical Reviews*, 104(10):4845–4866, oct 2004.

[3] HC Patel, AN Tabish, Filipo Comelli, and PV Aravind. Oxidation of H_2, CO and syngas mixtures on ceria and nickel pattern anodes. *Applied Energy*, 154:912–920, sep 2015.

[4] Jeffrey Hanna, Won Yong Lee, Yixiang Shi, and Ahmed F Ghoniem. Fundamentals of electro-and thermochemistry in the anode of Solid Oxide Fuel Cells with hydrocarbon and syngas fuels. *Progress in Energy and Combustion Science*, 40:74–111, feb 2014.

[5] Anja Bieberle, Lorenz P Meier, and Ludwig J Gauckler. The electrochemistry of Ni pattern anodes used as Solid Oxide Fuel Cell model electrodes. *Journal of the Electrochemical Society*, 148(6):A646–A656, February 2006.

[6] Junichiro Mizusaki, Hiroaki Tagawa, Takatoshi Saito, Kouji Kamitani, Tamaki Yamamura, Katsuhiko Hirano, Shaw Ehara, Toshinori Takagi, Tomoji Hikita, Masamichi Ippommatsu, et al. Preparation of nickel pattern electrodes on YSZ and their electrochemical properties in H_2/H_2O atmospheres. *Journal of the Electrochemical Society*, 141(8):2129–2134, 1994.

[7] HC Patel. *Multi-Fuel oxidation in Solid Oxide Fuel Cells: Model anodes and system studies*. PhD thesis, TU Delft, Delft University of Technology, 2015.

[8] Subhash C Singhal and Kevin Kendall. *High-temperature solid oxide fuel cells: fundamentals, design and applications*. Elsevier, 2003.

[9] Robert J Kee, Huayang Zhu, A Mary Sukeshini, and Gregory S Jackson. Solid Oxide Fuel Cells: operating principles, current challenges, and the role of syngas. *Combustion Science and Technology*, 180(6):1207–1244, may 2008.

[10] Davide Papurello, Andrea Lanzini, Lorenzo Tognana, Silvia Silvestri, and Massimo Santarelli. Waste to energy: exploitation of biogas from organic waste in a 500 W el solid oxide fuel cell (SOFC) stack. *Energy*, 85:145–158, jun 2015.

[11] Vitaliano Chiodo, Antonio Galvagno, Andrea Lanzini, Davide Papurello, Francesco Urbani, Massimo Santarelli, and Salvatore Freni. Biogas reforming process investigation for SOFC application. *Energy Conversion and Management*, 98:252–258, jul 2015.

[12] Yoshio Matsuzaki and Isamu Yasuda. Electrochemical oxidation of H_2 and CO in a H_2-H_2O-CO-CO_2 system at the interface of a Ni-YSZ cermet electrode and YSZ electrolyte. *Journal of the Electrochemical Society*, 147(5):1630–1635, 2000.

[13] Yi Jiang and Anil V Virkar. Fuel composition and diluent effect on gas transport and performance of anode-supported SOFCs. *Journal of The Electrochemical Society*, 150(7):A942–A951, 2003.

[14] Andre Weber, Bastian Sauer, Axel C Müller, Dirk Herbstritt, and Ellen Ivers-Tiffée. Oxidation of H_2, CO and methane in SOFCs with Ni/YSZ-cermet anodes. *Solid State Ionics*, 152:543–550, dec 2002.

[15] Kazunari Sasaki, Yoshio Hori, Ryuji Kikuchi, Kohei Eguchi, Akira Ueno, Hideki Takeuchi, Masato Aizawa, K Tsujimoto, H Tajiri, H Nishikawa, et al. Current-voltage characteristics and impedance analysis of Solid Oxide Fuel Cells for mixed H_2 and CO gases. *Journal of The Electrochemical Society*, 149(3):A227–A233, 2002.

[16] Mary Sukeshini, Bahman Habibzadeh, Benjamin P Becker, Chad A Stoltz, Bryan W Eichhorn, and Gregory S Jackson. Electrochemical oxidation of H_2, CO, and CO/H_2 mixtures on patterned Ni anodes on YSZ electrolytes. *Journal of the Electrochemical Society*, 153(4):A705–A715, 2006.

[17] Rapeepong Suwanwarangkul, Eric Croiset, Evgueniy Entchev, Sumittra Charojrochkul, Mark D. Pritzker, Michael W Fowler, Peter L Douglas, S Chewathanakup, and H Mahaudom. Experimental and modeling study of Solid Oxide Fuel Cell operating with syngas fuel. *Journal of Power Sources*, 161(1):308–322, oct 2006.

[18] Cheng Bao and Xinxin Zhang. One-dimensional macroscopic model of Solid Oxide Fuel Cell anode with analytical modeling of H_2/CO electrochemical co-oxidation. *Electrochimica Acta*, 134:426–434, jul 2014.

[19] Martin Andersson, Jinliang Yuan, and Bengt Sundén. Sofc modeling considering hydrogen and carbon monoxide as electrochemical reactants. *Journal of Power Sources*, 232:42–54, jun 2013.

[20] Meng Ni. Modeling of sofc running on partially pre-reformed gas mixture. *International Journal of Hydrogen Energy*, 37(2):1731–1745, jan 2012.

[21] Connor J Moyer, Neal P Sullivan, Huayang Zhu, and Robert J Kee. Polarization characteristics and chemistry in reversible tubular solid-oxide cells operating on mixtures of H_2, CO, H_2O, and CO_2. *Journal of The Electrochemical Society*, 158(2):B117–B131, 2011.

[22] Katherine Mary Ong. *Modeling of solid oxide fuel cell performance with coal gasification*. PhD thesis, Massachusetts Institute of Technology, 2016.

[23] Cheng Bao, Zeyi Jiang, and Xinxin Zhang. Mathematical modeling of synthesis gas fueled electrochemistry and transport including H_2/CO co-oxidation and surface diffusion in Solid Oxide Fuel Cell. *Journal of Power Sources*, 294:317–332, oct 2015.

[24] Antonin Faes, Aïcha Hessler-Wyser, Amédée Zryd, et al. A review of redox cycling of Solid Oxide Fuel Cells anode. *Membranes*, 2(3):585–664, 2012.

[25] He Miao, Guanghui Liu, Tao Chen, Changrong He, Jun Peng, Shuang Ye, and Wei Guo Wang. Behavior of anode-supported SOFCs under simulated syngases. *Journal of Solid State Electrochemistry*, 19(3):639–646, sep 2014.

[26] Mogens Mogensen, Nigel M Sammes, and Geoff A Tompsett. Physical, chemical and electrochemical properties of pure and doped ceria. *Solid State Ionics*, 129(1):63–94, 2000.

[27] Ju-Sik Kim, Vineet V Nair, John M Vohs, and Raymond J Gorte. A study of the methane tolerance of LSCM-YSZ composite anodes with Pt, Ni, Pd and ceria catalysts. *Scripta Materialia*, 65(2):90–95, jul 2011.

[28] Alessandro Trovarelli and Paolo Fornasiero. *Catalysis by ceria and related materials*, volume 2. Imperial College Press London, may 2002.

[29] HC Patel, N Biradar, V Venkataraman, and PV Aravind. Ceria electrocatalysis compared to Nickel using pattern anodes. *Int. J. Electrochem. Sci*, 9:4048–4053, 2014.

[30] Stéphanie Hilaire, Xingyi Wang, Tingwen Luo, Raymond J Gorte, and Jon P Wagner. A comparative study of water-gas-shift reaction over ceria supported metallic catalysts. *Applied Catalysis A: General*, 215(1):271–278, feb 2004.

[31] Jose A Rodriguez, S Ma, P Liu, J Hrbek, J Evans, and M Perez. Activity of CeOx and TiOx nanoparticles grown on Au(111) in the water-gas-shift reaction. *Science*, 318(5857):1757–1760, dec 2007.

[32] Steven C. DeCaluwe. *Quantifying the role of cerium oxide as a catalyst in solid oxide fuel cell*. PhD thesis, 2009.

[33] PV Aravind, JP Ouweltjes, N Woudstra, and G Rietveld. Impact of biomass-derived contaminants on SOFCs with Ni/Gadolinia-doped ceria anodes. *Electrochemical and Solid-State Letters*, 11(2):B24–B28, 2008.

[34] Raymond J Gorte and John M Vohs. Nanostructured anodes for solid oxide fuel cells. *Current Opinion in Colloid & Interface Science*, 14(4):236–244, 2009.

[35] Olga Costa-Nunes, Raymond J Gorte, and John M Vohs. Comparison of the performance of Cu-CeO_2-YSZ and Ni-YSZ composite sofc anodes with H_2, CO, and syngas. *Journal of Power Sources*, 141(2):241–249, 2005.

[36] Chia-Ling Lu, Wayne L Worrell, John M Vohs, and Raymond J Gorte. A comparison of Cu-ceria-SDC and Au-ceria-SDC composites for sofc anodes. *Journal of The Electrochemical Society*, 150(10):A1357–A1359, 2003.

[37] HC Patel, AN Tabish, and PV Aravind. Modelling of elementary kinetics of H_2 and CO oxidation on ceria pattern cells. *Electrochimica Acta*, 182:202–211, nov 2015.

[38] Chunjuan Zhang, Yi Yu, Michael E Grass, Catherine Dejoie, Wuchen Ding, Karen Gaskell, Naila Jabeen, et al. Mechanistic studies of water electrolysis and hydrogen electro-oxidation on high temperature ceria-based solid oxide electrochemical cells. *Journal of the American Chemical Society*, 135(31):11572–11579, aug 2013.

[39] Yi Yu, Baohua Mao, Aaron Geller, Rui Chang, Karen Gaskell, Zhi Liu, and Bryan W Eichhorn. CO_2 activation and carbonate intermediates: an operando AP-XPS study of CO_2 electrolysis reactions on solid oxide electrochemical cells. *Phys. Chem. Chem. Phys.*, 16(23):11633–11639, 2014.

[40] PV Aravind, JP Ouweltjes, and Joop Schoonman. Diffusion impedance on nickel/gadolinia-doped ceria anodes for solid oxide fuel cells. *Journal of The Electrochemical Society*, 156(12):B1417–B1422, 2009.

[41] HC Patel, V Venkataraman, and PV Aravind. Nickel pattern anodes for studying sofc electrochemistry. In *Advances in Solid Oxide Fuel Cells IX*, number 4, page 89. John Wiley & Sons, nov 2013.

[42] Marcel Vogler, Anja Bieberle-Hütter, Ludwig Gauckler, Jürgen Warnatz, and Wolfgang G Bessler. Modelling study of surface reactions, diffusion, and spillover at a Ni/YSZ patterned anode. *Journal of The Electrochemical Society*, 156(5):B663–B672, 2009.

[43] Vitaliy Yurkiv, Annika Utz, André Weber, Ellen Ivers-Tiffée, Hans-Robert Volpp, and Wolfgang G Bessler. Elementary kinetic modeling and experimental validation of electrochemical CO oxidation on Ni/YSZ pattern anodes. *Electrochimica Acta*, 59:573–580, jan 2012.

[44] Jeffrey Hanna, Won Yong Lee, and Ahmed F Ghoniem. Kinetics of carbon monoxide electro-oxidation in Solid Oxide Fuel Cells from Ni-YSZ patterned-anode measurements. *Journal of the Electrochemical Society*, 160(6):F698–F708, apr 2013.

[45] Driscoll A. Tobin, Nicholas Hale, and Lloyd N Trefethen, editors. *Chebfun Guide*. Pafnuty Publications Oxford, 2014.

[46] Weifang Yao and Eric Croiset. Investigation of H_2, CO and syngas electrochemical performance using Ni/YSZ pattern anodes. *ECS Transactions*, 53(30):163–172, oct 2013.

[47] Kohei Eguchi, Hideaki Kojo, Tatsuya Takeguchi, Ryuji Kikuchi, and Kazunari Sasaki. Fuel flexibility in power generation by Solid Oxide Fuel Cells. *Solid State Ionics*, 152:411–416, dec 2002.

[48] Junichiro Mizusaki, Hiroaki Tagawa, Takatoshi Saito, Tamaki Yamamura, Kouji Kamitani, Katsuhiko Hirano, Shaw Ehara, Toshinori Takagi, Tomoji Hikita, Masamichi Ippommatsu, et al. Kinetic studies of the reaction at the nickel pattern electrode on YSZ in H_2/H_2O atmospheres. *Solid State Ionics*, 70:52–58, may 1994.

[49] Wolfgang G Bessler, Marcel Vogler, Heike Störmer, Dagmar Gerthsen, Annika Utz, André Weber, and Ellen Ivers-Tiffée. Model

anodes and anode models for understanding the mechanism of hydrogen oxidation in Solid Oxide Fuel Cells. *Physical Chemistry Chemical Physics*, 12(42):13888–13903, 2010.

[50] Lei Zhang, Feng Liu, Kyle Brinkman, Kenneth L Reifsnider, and Anil V Virkar. A study of gadolinia-doped ceria electrolyte by electrochemical impedance spectroscopy. *Journal of Power Sources*, 247:947–960, feb 2014.

[51] Xin Guo, Wilfried Sigle, and Joachim Maier. Blocking grain boundaries in yttria-doped and undoped ceria ceramics of high purity. *Journal of the American Ceramic Society*, 86(1):77–87, jan 2003.

[52] WooChul Jung, Julien O Dereux, William C Chueh, Yong Hao, and Sossina M Haile. High electrode activity of nanostructured, columnar ceria films for solid oxide fuel cells. *Energy & Environmental Science*, 5(9):8682–8689, 2012.

[53] William C Chueh, Yong Hao, WooChul Jung, and Sossina M Haile. High electrochemical activity of the oxide phase in model ceria-Pt and ceria-Ni composite anodes. *Nature Materials*, 11(2):155–161, dec 2011.

[54] Can Li, Yoshihisa Sakata, Toru Arai, Kazunari Domen, Ken-ichi Maruya, and Takaharu Onishi. Carbon monoxide and carbon dioxide adsorption on cerium oxide studied by fourier-transform infrared spectroscopy. part 1. formation of carbonate species on dehydroxylated CeO2, at room temperature. *Journal of the Chemical Society, Faraday Transactions 1: Physical Chemistry in Condensed Phases*, 85(4):929–943, 1989.

[55] Konstanze R Hahn, Marcella Iannuzzi, Ari P Seitsonen, and Ju rg Hutter. Coverage effect of the CO_2 adsorption mechanisms on CeO_2(111) by first principles analysis. *The Journal of Physical Chemistry C*, 117(4):1701–1711, jan 2013.

[56] Christopher Graves, Christodoulos Chatzichristodoulou, and Mogens B. Mogensen. Kinetics of CO/CO2 and H2/H2o reactions at Ni-based and ceria-based solid-oxide-cell electrodes. *Faraday discussions*, 182:75–95, 2015.

[57] Alessandro Trovarelli. Catalytic properties of ceria and CeO_2-containing materials. *Catalysis Reviews*, 38(4):439–520, nov 1996.

[58] Tiziano Montini, Michele Melchionna, Matteo Monai, and Paolo Fornasiero. Fundamentals and catalytic applications of CeO_2-based materials. *Chemical Reviews*, 116(10):5987–6041, 2016.

[59] Seungdoo Park, Radu Craciun, John M Vohs, and Raymond J Gorte. Direct oxidation of hydrocarbons in a solid oxide fuel cell: I. methane oxidation. *Journal of the Electrochemical Society*, 146(10):3603–3605, 1999.

[60] David A Andersson, Sergei I Simak, Natalia V Skorodumova, Igor A Abrikosov, and Börje Johansson. Optimization of ionic conductivity in doped ceria. *Proceedings of the National Academy of Sciences*, 103(10):3518–3521, feb 2006.

[61] Olga A Marina, Carsten Bagger, Søren Primdahl, and Mogens Mogensen. A solid oxide fuel cell with a gadolinia-doped ceria anode: preparation and performance. *Solid State Ionics*, 123(1):199–208, aug 1999.

[62] Wang Hay Kan and Venkataraman Thangadurai. Challenges and prospects of anodes for solid oxide fuel cells (sofcs). *Ionics*, 21(2):301–318, dec 2014.

[63] M Shishkin and T Ziegler. The electronic structure and chemical properties of a Ni/CeO_2 anode in a solid oxide fuel cell: a DFT+ U study. *The Journal of Physical Chemistry C*, 114(49):21411–21416, 2010.

[64] M Shishkin and T Ziegler. Direct modeling of the electrochemistry in the three-phase boundary of solid oxide fuel cell anodes by density functional theory: a critical overview. 16:1798–1808.

[65] Lei Wang. *Model Development for Gadolinia-doped Ceria-based Anodes in Solid Oxide Fuel Cells*. PhD thesis, 2014.

[66] Chi Chen, Dengjie Chen, William C Chueh, and Francesco Ciucci. Modeling the impedance response of mixed-conducting thin film electrodes. *Physical Chemistry Chemical Physics*, 16(23):11573–11583, 2014.

[67] Francesco Ciucci, William C Chueh, David G Goodwin, and Sossina M Haile. Surface reaction and transport in mixed conductors with electrochemically-active surfaces: a 2-D numerical study of ceria. *Phys. Chem. Chem. Phys.*, 13(6):2121–2135, 2011.

[68] J El Fallah, S Boujana, H Dexpert, A Kiennemann, J Majerus, O Touret, F Villain, and F Le Normand. Redox processes on pure ceria and on Rh/CeO_2 catalyst monitored by X-ray absorption (fast acquisition mode). *The Journal of Physical Chemistry*, 98(21):5522–5533, 1994.

[69] Zhuoluo A Feng, Farid El Gabaly, Xiaofei Ye, Zhi-Xun Shen, and William C Chueh. Fast vacancy-mediated oxygen ion incorporation across the ceria-gas electrochemical interface. *Nature Communications*, 5, jul 2014.

[70] Wolfgang G Bessler, Stefan Gewies, and Marcel Vogler. A new framework for physically based modeling of Solid Oxide Fuel Cells. *Electrochimica Acta*, 53(4):1782–1800, dec 2007.

[71] Hsin-Tsung Chen, Yong Man Choi, Meilin Liu, and MC Lin. A theoretical study of surface reduction mechanisms of CeO_2 (111) and (110) by H_2. *ChemPhysChem*, 8(6):849–855, apr 2007.

[72] Ferdinand A Kröger. *The chemistry of imperfect crystals*. North-Holland, Amsterdam, 1964.

[73] Heine A Hansen and Christopher Wolverton. Kinetics and thermodynamics of H_2O dissociation on reduced CeO_2(111). *The Journal of Physical Chemistry C*, 118(47):27402–27414, nov 2014.

[74] Zhenlong Zhao, Mruthunjaya Uddi, Nikolai Tsvetkov, Bilge Yildiz, and Ahmed F Ghoniem. Redox kinetics study of fuel reduced ceria for chemical looping water splitting. *The Journal of Physical Chemistry C*, 30(120):16271–16289, aug 2016.

[75] Yet M Chiang, Dunbar P Birnie, and David W Kingery. Physical ceramics, john&wiley sons. *Inc., New York*, 1997.

[76] Frank S Baumann, Jürgen Fleig, Hanns-Ulrich Habermeier, and Joachim Maier. Impedance spectroscopic study on well-defined (La, Sr)(Co,Fe)O_3-δ model electrodes. *Solid State Ionics*, 177(11):1071–1081, apr 2006.

[77] Steven C DeCaluwe, A Mary Sukeshini, and Gregory S Jackson. Experimental characterization of thin-film ceria solid oxide fuel cell anodes. 16(51):235–251, 2009.

[78] Francesco Ciucci, Yong Hao, and David G Goodwin. Impedance spectra of mixed conductors: a 2d study of ceria. *Physical Chemistry Chemical Physics*, 11(47):11243–11257, 2009.

[79] Joachim Maier. *Physical chemistry of ionic materials: ions and electrons in solids*. John Wiley & Sons, 2004.

[80] Mark E Orazem and Bernard Tribollet. *Electrochemical impedance spectroscopy*, volume 48. John Wiley & Sons, 2011.

[81] Annika Utz, H Strmer, André Leonide, André Weber, and Ellen Ivers-Tiffée. Degradation and relaxation effects of Ni patterned anodes in H_2-H_2O atmosphere. *Journal of the Electrochemical Society*, 157(6):B920–B930, 2010.

[82] Baukje De Boer. *SOFC Anode. Hydrogen oxidation at porous nickel and nickel/yttria-stabilised zirconia cermet electrodes*. PhD thesis, 1998.

[83] Weifang Yao and Eric Croiset. Ni/YSZ pattern anodes fabrication and their microstructure and electrochemical behavior changes in H_2/H_2O environments. *Journal of Power Sources*, 226:162–172, mar 2013.

[84] Andreas Ehn, J Høgh, Mariusz Graczyk, Kion Norrman, Lars Montelius, M Linne, and M Mogensen. Electrochemical investigation of nickel pattern electrodes in h2/h2o and co/co2 atmospheres. *Journal of the Electrochemical Society*, 157(11):B1588–B1596, 2010.

[85] John TS Irvine, Dragos Neagu, Maarten C Verbraeken, Christodoulos Chatzichristodoulou, Christopher Graves, and Mogens B Mogensen. Evolution of the electrochemical interface in high-temperature fuel cells and electrolysers. *Nature Energy*, 1(1):15014, jan 2016.

[86] Anja Bieberle. *The electrochemistry of Solid Oxide Fuel Cell anodes: experiments, modeling, and simulations*. PhD thesis.

[87] Annika Utz. *The Electrochemical Oxidation of H_2 and CO at Patterned Ni Anodes of SOFCs*. PhD thesis, 2011.

[88] Weifang Yao. *Hydrogen and Carbon Monoxide Electrochemical Oxidation Reaction Kinetics on Solid Oxide Fuel Cell Anodes*. PhD thesis.

[89] David G Goodwin, Huayang Zhu, Andrew M Colclasure, and Robert J Kee. Modeling electrochemical oxidation of hydrogen on Ni-YSZ pattern anodes. *Journal of The Electrochemical Society*, 156(9):B1004–B1021, 2009.

[90] Wolfgang G Bessler, Jürgen Warnatz, and David G Goodwin. The influence of equilibrium potential on the hydrogen oxidation kinetics of SOFC anodes. *Solid State Ionics*, 177(39):3371–3383, jan 2007.

[91] Anja Bieberle and LJ Gauckler. State-space modeling of the anodic sofc system ni, H_2H_2O YSZ. *Solid State Ionics*, 146(1):23–41, jan 2002.

[92] Weifang Yao and Eric Croiset. Modelling and Ni/Yttria-Stabilized-Zirconia pattern anode experimental validation of a new charge transfer reactions mechanism for hydrogen electrochemical oxidation on solid oxide fuel cell anodes. *Journal of Power Sources*, 248:777–788, feb 2014.

[93] Mogens Bjerg Mogensen and T Lindegaard. The kinetics of hydrogen oxidation on a Ni-YSZ SOFC electrode at 1000 C. *Solid Oxide Fuel Cells*, 1993.

[94] Peter Holtappels, LGJ de De Haart, and Ulrich Stimming. Reaction of hydrogen/water mixtures on nickel-zirconia cermet electrodes: I. DC polarization characteristics. *Journal of The Electrochemical Society*, 146(5):1620–1625, 1999.

[95] Marcel Vogler and Wolfgang G. Bessler. The role of interstitial hydrogen species in Ni/YSZ patterned anodes: A 2d modeling study. *ECS Transactions*, 25(2):1957–1966, 2009.

[96] Huayang Zhu, Robert J Kee, Vinod M Janardhanan, Olaf Deutschmann, and David G Goodwin. Modeling elementary heterogeneous chemistry and electrochemistry in solid-oxide fuel cells. *Journal of The Electrochemical Society*, 152(12):A2427–A2440, 2005.

[97] Katherine M Ong, Jeffrey Hanna, and Ahmed F Ghoniem. Investigation of a combined hydrogen and oxygen spillover mechanism for syngas electro-oxidation on ni/ysz. *Journal of The Electrochemical Society*, 164(2):F32–F45, 2017.

[98] Huayang Zhu and Robert J Kee. Two-dimensional model of distributed charge transfer and internal reforming within unit cells of segmented-in-series solid-oxide fuel cells. *Journal of Power Sources*, 196(18):7654–7664, sep 2011.

[99] AN Tabish, HC Patel, and PV Aravind. Electrochemical oxidation of syngas on nickel and ceria anodes. *Electrochimica Acta*, 228:575–585, feb 2017.

[100] WS Rasband. Imagej. *National Institutes of Health, Bethesda, Maryland, USA, https://imagej.nih.gov/ij/*, 1997–2018.

[101] Rajesh Radhakrishnan, Anil V Virkar, and Subhash C Singhal. Estimation of charge-transfer resistivity of pt cathode on ysz electrolyte using patterned electrodes. 152(5):A927–A936, 2005.

[102] John O'M Bockris, Amulya K.N. Reddy, and Maria Gamboa-Aldeco. Modern electrochemistry 2A: Fundamentals of electrodics, 2000.

[103] DA Noren and Myron A Hoffman. Clarifying the butler–volmer equation and related approximations for calculating activation losses in solid oxide fuel cell models. *Journal of Power Sources*, 152:175–181, dec 2005.

[104] Paul R Shearing, Qiong Cai, Joshua I Golbert, Vladimir Yufit, Claire S Adjiman, and Nigel P Brandon. Microstructural analysis of a solid oxide fuel cell anode using focused ion beam techniques coupled with electrochemical simulation. *Journal of Power Sources*, 195(15):4804–4810, 2010.

[105] JR Ferguson, Jean M Fiard, and Raphaèle Herbin. Three-dimensional numerical simulation for various geometries of solid oxide fuel cells. *Journal of Power Sources*, 58(2):109–122, feb 1996.

[106] Won Yong Lee, Daehyun Wee, and Ahmed F Ghoniem. An improved one-dimensional membrane-electrode assembly model to predict the performance of solid oxide fuel cell including the limiting current density. *Journal of Power Sources*, 186(2):417–427, jan 2009.

[107] Bora Timurkutluk and Mahmut D Mat. A review on micro-level modeling of solid oxide fuel cells. *International Journal of Hydrogen Energy*, 41(23):9968–9981, 2016.

[108] Paul R Shearing, Joshua I Golbert, RJ Chater, and Nigel P Brandon. 3D reconstruction of sofc anodes using a focused ion beam lift-out technique. *Chemical Engineering Science*, 64(17):3928–3933, 2009.

[109] Kongfa Chen, Xiangjun Chen, Zhe Lü, Na Ai, Xiqiang Huang, and Wenhui Su. Performance of an anode-supported sofc with anode functional layers. *Electrochimica Acta*, 53(27):7825–7830, 2008.

[110] Tsuyoshi Nagasawa and Katsunori Hanamura. Prediction of overpotential and effective thickness of ni/ysz anode for solid oxide fuel cell by improved species territory adsorption model. *Journal of Power Sources*, 353:115–122, 2017.

[111] Qiong Cai, Claire S Adjiman, and Nigel P Brandon. Investigation of the active thickness of solid oxide fuel cell electrodes using a 3d microstructure model. *Electrochimica Acta*, 56(28):10809–10819, 2011.

[112] Søren Primdahl and M Mogensen. Oxidation of hydrogen on Ni/yttria-stabilized zirconia cermet anodes. *Journal of Power Sources*, 144(10):3409–3419, 1996.

[113] M Brown, Soren Primdahl, and Mogens Mogensen. Structure/performance relations for ni/yttria-stabilized zirconia anodes for solid oxide fuel cells. *Journal of the electrochemical society*, 147(2):475–485, 2000.

[114] Hwan Moon, Sun Dong Kim, Eon Woo Park, Sang Hoon Hyun, and Ho Sung Kim. Characteristics of sofc single cells with anode active layer via tape casting and co-firing. *International Journal of Hydrogen Energy*, 33(11):2826–2833, 2008.

[115] Jingde Li, Zhengyu Bai, and Eric Croiset. A two-dimensional modeling of solid oxide fuel cell button cells with detailed electrochemistry mechanism. *Journal of Power Sources*, 333:164–172, 2016.

[116] Jiangrong Kong, Kening Sun, Derui Zhou, Naiqing Zhang, Ju Mu, and Jinshuo Qiao. Ni–ysz gradient anodes for anode-supported sofcs. *Journal of Power Sources*, 166(2):337–342, 2007.

[117] Haruo Kishimoto, Teruhisa Horita, Katsuhiko Yamaji, Manuel E Brito, Yue-Ping Xiong, and Harumi Yokokawa. Sulfur poisoning on sofc ni anodes: Thermodynamic analyses within local equilibrium anode reaction model. *Journal of The Electrochemical Society*, 157(6):B802–B813, 2010.

[118] Matthias Riegraf, Günter Schiller, Rémi Costa, K Andreas Friedrich, Arnulf Latz, and Vitaliy Yurkiv. Elementary kinetic numerical simulation of Ni/YSZ SOFC anode performance considering sulfur poisoning. *Journal of the Electrochemical Society*, 162(1):F65–F75, 2015.

[119] Jason P Trembly, Randall S Gemmen, and David J Bayless. The effect of coal syngas containing HCl on the performance of solid oxide fuel cells: Investigations into the effect of operational temperature and HCl concentration. *Journal of Power Sources*, 169(2):347–354, jun 2007.

[120] Abraham Van der Drift, Joep Van Doorn, and JW Vermeulen. Ten residual biomass fuels for circulating fluidized-bed gasification. *Biomass and Bioenergy*, 20(1):45–56, 2001.

[121] Hossein Madi, Andrea Lanzini, Davide Papurello, Stefan Diethelm, Christian Ludwig, Massimo Santarelli, et al. Solid oxide fuel cell anode degradation by the effect of hydrogen chloride in stack and single cell environments. *Journal of Power Sources*, 326:349–356, sep 2016.

[122] Ting Shuai Li, Cheng Xu, Tao Chen, He Miao, and Wei Guo Wang. Chlorine contaminants poisoning of solid oxide fuel cells. *Journal of Solid State Electrochemistry*, 15(6):1077–1085, aug 2010.

[123] Olga A Marina, Larry R Pederson, Edwin C Thomsen, Christopher A Coyle, and Kyung J Yoon. Reversible poisoning of nickel/zirconia solid oxide fuel cell anodes by hydrogen chloride in coal gas. *Journal of Power Sources*, 195(20):7033–7037, oct 2010.

[124] Chunchuan Xu, Mingyang Gong, John W Zondlo, XingBo Liu, and Harry O Finklea. The effect of HCl in syngas on Ni/YSZ anode-supported solid oxide fuel cells. *Journal of Power Sources*, 195(8):2149–2158, apr 2010.

[125] JianEr Bao, Gopala N Krishnan, Palitha Jayaweera, Jordi Perez-Mariano, and Angel Sanjurjo. Effect of various coal contaminants on the performance of solid oxide fuel cells: Part I. accelerated testing. *Journal of Power Sources*, 193(2):607–616, sep 2009.

[126] Gerhard Buchinger, Paul Hinterreiter, Thomas Raab, Stefan Griesser, Richard Claassen, Dirk Peter Claassen, Werner Sitte, and Dieter Meissner. Operating microtubular SOFCs with hydrogen chloride and hydrogen sulfide containing fuels and synthetic

wood gas. *Journal of Fuel Cell Science and Technology*, 3(3):280–283, 2006.

[127] Javier Prez-Ramrez, Cecilia Mondelli, Timm Schmidt, Oliver F-K Schlter, Aurel Wolf, Leslaw Mleczko, and Thorsten Dreier. Sustainable chlorine recycling via catalysed HCl oxidation: from fundamentals to implementation. *Energy & Environmental Science*, 4(12):4786–4799, 2011.

[128] Ramzi Farra, Maik Eichelbaum, Robert Schlögl, László Szentmiklósi, Timm Schmidt, Amol P Amrute, Cecilia Mondelli, Javier Pérez-Ramírez, and Detre Teschner. Do observations on surface coverage-reactivity correlations always describe the true catalytic process? a case study on ceria. 297:119–127.

[129] K Haga, Yusuke Shiratori, Kensuke Ito, and Kotaro Sasaki. Chlorine poisoning of SOFC Ni-cermet anodes. *Journal of The Electrochemical Society*, 155(12):B1233–B1239, 2008.

[130] CW Bale, E Bélisle, P Chartrand, SA Decterov, G Eriksson, K Hack, I-H Jung, Y-B Kang, J Melançon, AD Pelton, et al. FactSage thermochemical software and databases -recent developments. *Calphad*, 33(2):295–311, jun 2009.

[131] Amol P Amrute, Cecilia Mondelli, Maximilian Moser, Gerard Novell-Leruth, Núria López, Dirk Rosenthal, Ramzi Farra, Manfred E Schuster, Detre Teschner, Timm Schmidt, et al. Performance, structure, and mechanism of CeO_2 in HCl oxidation to Cl_2. *Journal of Catalysis*, 286:287–297, feb 2012.

[132] Georgi N Vayssilov, Mihail Mihaylov, Petko St Petkov, Konstantin I Hadjiivanov, and Konstantin M Neyman. Reassignment of the vibrational spectra of carbonates, formates, and related surface species on ceria: a combined density functional and infrared spectroscopy investigation. *The Journal of Physical Chemistry C*, 115(47):23435–23454, dec 2011.

List of publications

Peer Reviewed Journal Articles

[1] H.C. Patel, **A.N. Tabish**, F. Comelli, and P.V. Aravind. Oxidation of H_2, CO and syngas mixtures on ceria and nickel pattern anodes. *Applied Energy*, 154:912–920, Sep. 2015.

[2] H.C. Patel, **A.N. Tabish**, and P.V. Aravind. Modelling of elementary kinetics of H_2 and CO oxidation on ceria pattern cells. *Electrochimica Acta*, 182:202–211, Nov. 2015.

[3] **A.N. Tabish**, H.C. Patel, and P.V. Aravind. Electrochemical oxidation of syngas on nickel and ceria anodes. *Electrochimica Acta*, 228:575–585, Feb. 2017.

[4] **A.N. Tabish**, H.C. Patel, J. Schoonman, and P.V. Aravind. A detailed look into hydrogen electrochemical oxidation on ceria. *Electrochimical Acta* 283: 789-797, May 2018.

[5] **A.N. Tabish**, H.C. Patel, JinJun Li, P. Chundru, and P.V. Aravind. An SOFC anode model using TPB-based kinetics. *to be submitted*

[6] **A.N. Tabish**, H.C. Patel, and P.V. Aravind. The effect of HCl contaminant on pattern and cermet cells. *to be submitted*

Conference Proceedings

[1] **A.N. Tabish**, H.C. Patel, F. Comelli, and P.V. Aravind. Electrochemical oxidation of CO/H_2 mixtures on Ni and Ceria pattern anodes. In *ECS Transactions* 68(1) 1129–1136 (2015).

[2] P. V. Aravind, A. Cavalli, H. C. Patel, M. Recalde, A. Saadabadi, **AN Tabish**, G. Botta, A. T. Thattai, A. Teodoru, S. Hajimolana, P. Chundru, T. Woudstra. Opportunities and Challenges in using SOFCs in Waste to Energy Systems. In *ECS Transactions* 78 (1) 209-218 (2017)

Acknowledgements

There are so many people to thank for their contributions in the accomplishment of this work. I would like to start off by expressing my deep gratitude to my promotor **Dr. PV Aravind** for his continuous supervision and guidance. His invaluable guidance was instrumental in realizing this thesis, and I also appreciate the autonomy he granted me to conduct this research. I would also like to thank my second promoter **Prof. BJ Boersma** for his support. Also, to **Prof. Joop Schoonman** who really introduced me the importance of defect chemistry for understanding the MIEC electrode electrochemistry. Special thanks goes to **Ir. Theo Woudstra** as well, for useful discussions on thermodynamics, one of my favourite subjects since my undergraduate studies. It will be highly unfair to not thank my unofficial mentor and colleague **Dr. HC Patel** for his invaluable inputs from the beginning till the end of my PhD. The technical discussions we had helped me in conducting experiments, evaluating the results, drafting, and finally improving the quality of my thesis. I also thank **Jelle Stam** for his valuable contribution at the last stage of my PhD.

I am also thankful to my colleagues and fuel cell group members – **Liyuan, Eva, Aditya, Alvaro, Giulia, Mayra, Ali, Alessando, Ana, Lindert, Vincent,and Yashar** – who I had the pleasure of working with. I appreciate that they were always there for technical discussions and for off and on gatherings to celebrate various happy moments during the course of this research. I would also like to thank our workshop team – **Michel, Martijn, Duncan** among others – for assisting me with experiments, our secretary **Eveline** for helping with administrative tasks, and **Rob** for bearing the burden of financial management. I also thank **TU Delft Graduate School** for offering various courses to acquire transferable and research related skills, and inspiring me to

self-track the progress and finish the PhD. I would also like to extend my gratitudes to my students **Pradeep** and **JinJun** who worked with me in the last phase of my PhD.

I could not have performed this research without the financial support of **University of Engineering and Technology (UET) Lahore - Pakistan**. I am grateful that the University granted me a PhD scholarship under the faculty development program (FDP) and afforded me the flexibility to pursue the research topic of my choice in the field of clean energy technology. I also thank **Prof.dr. M. Zafar Noon** and **Dr. Tanveer Iqbal** for there administrative support back in UET Lahore.

I am also grateful to **Hussam**, my housemate and a great chef, who never let me miss my home dishes (Biryani, Nihari, Paye, Haleem ...). **Saad, Irfan, Imran, and Fawad** were always there to join the dining table at week-ends, to play cards, and to have heated debates on social, political, and scientific topics. I am indebted to my cricket buddies **Faisal, Usama, Fahim, Hrishikesh** among others from Pakistan and India and football friends from the department (I will remember that we finally managed to setback our unbeatable student's football team after 37 years of struggle). With the help of all these friends, the life in Delft became much smoother than I imagined considering the work load of PhD.

My brothers, sisters, and mom and dad have always been a constant source of encouragement and inspiration to me in my whole academic pursuit. Due to their unconditional support, love, freedom, and countless prayers, there has never been any laborious moment in my life. The rock solid belief that my (late) grand-father had on my hard work and commitment was the sole reason that paved my way to this day.

Someone who compromised the most with my busy routine is my wife **Iqra Farhat**. She has always stood next to me, took me out of so many depressing occasions, and pushed me so much that I successfully managed to submit the thesis draft. I am deeply indebted to her for her unlimited support. I am also grateful to my in-laws for their trust and support. My special thanks to almighty Allah for blessing us a beautiful baby **M.A. Raza** in the last year of PhD, the blessing that I can never repay.

About the Author

Tabish was born in Bahwal-Nagar, Pakistan on 1st of March 1989. He graduated in Chemical Engineering from the University of Engineering and Technology Lahore, Pakistan in 2009 and joined the faculty initially as a Research Assistant and then promoted as a Lab. Engineer/Lecturer. He completed his master's degree in Chemical Engineering with specialization in Process Engineering from the same University in 2012. He did his MSc thesis from the same University on "Thermoeconomic evaluation of an industrial fire-tube boiler" under the supervision of Prof. Dr. M. Zafar Noon. With an inspiration of continuing the academic career with research focus in the field of clean energy technology, he sought for PhD scholarship. In 2012, he was granted with a Phd fellowship under the Faculty Development Program (FDP) of the same University with a freedom to join any prestigious group around the world in the relevant field. In June 2013, he joined the fuel cell group of Dr. PV Aravind in the Technical University Delft, the Netherlands to research on the electrochemistry of SOFC anodes.